Jos Groot

Airborne and spaceborne SAR interferometry

E.J. Huising
Y. Dierikx
E.M.J. Vaessen
J. Vogelzang
RWS-MD
H. Greidanus
R.J.P. van Bree
J. Aardoom
TNO-FEL
G. Huurneman
ITC

USP-2 report 99-19
USP-2 project 2.2/AP-02
ISBN 90 54 11 292 1

December 1999

This report describes a project carried out in the framework of the National User Support Programme (USP-2) under responsibility of the Netherlands Remote Sensing Board (BCRS) and the Space Research Organization Netherlands (SRON)

Contents

Abstract

In this study, three types of interferometry, across-track (XTI), along-track (ATI), and repeat-pass (RPI), were investigated in the Waddenzee. XTI and ATI were studied with the airborne E-SAR system, while ERS tandem mode data were used for the RPI study.
XTI can be used to make a digital elevation map (DEM) of an area. Two such maps of the western part of the isle of Terschelling were compared to each other and to a DEM obtained with laser altimetry. The latter DEM has an accuracy of about 15 cm. The comparison shows that the height error in the XTI DEM varies from about 1 m for flat areas to about 3 m for forested areas. This figure compares well to those found in other studies. At this moment, XTI generated DEMs are not precise enough, but substantial improvements may be expected in the near future.
ATI allows generation of very detailed current velocity maps. The accuracy found is about 0.15 cm/s. Comparison with a model hindcast showed considerable differences, probably due to the fact that the model yields the depth-averaged current velocity rather than the surface velocity, the poor resolution of the model, and uncertainties in the wind drift correction. When used as input in a wave-current interaction model, the ATI flow field generated radar images that compare well to the observed images. The technique can be used for calibration and validation of detailed 3D flow models, and for mapping currents in coastal waters and rivers, though the relatively high costs may be a drawback.
Coherence maps constructed from ERS tandem mode data had little value for land classification. Good correlation was found only in very dry parts. In the more moist parts coherence at C-band is diminished by the effect of wind on the vegetation.

Executive summary

An image recorded with Synthetic Aperture Radar (SAR) image is a complex quantity. Besides the well known amplitude image it also contains phase information. This is used in interferometric applications, a new field of microwave remote sensing. These are relatively new and highly promising. In this study, three possible methods are studied to evaluate their potential in the coastal zone:

- Across-track interferometry (XTI);
- Along-track interferometry (ATI);
- Repeat-pass interferometry.

In XTI, the SAR system has two antennas located above each other, perpendicular to the flight track. The system therefore records two SAR images at the same time but from a slightly different location. This allows the generation of a Digital Elevation Map (DEM) of land areas recorded. In ATI the system also consists of two antennas, but now the antennas are placed next to each other, parallel to the flight direction. Now two SAR images are recorded from the same position but at slightly different times. ATI is sensitive to movement of the scatterers in the range direction. Above sea it produces a map of the current velocity component parallel to the radar look direction. A SAR system for repeat pass interferometry has one antenna. The flight track is repeated to obtain a second SAR image. A DEM can be generated from the two SAR images. The coherence (correlation) between the two images will decrease with increasing time between recording, depending on the nature of the surface recorded. This may give additional information on the terrain type.

The quality of interferometric measurements critically depends on the relative distance of the antenna(s) during measurement, the so-called base line. XTI and ATI are only possible using airborne systems with two antennas. The base line can therefore readily be found to the required precision. Repeat-pass interferometry is in principle also possible using aircraft, but the flight track and the aircraft attitude should be known with sufficient accuracy. The best known applications use ERS satellite data, especially from the ERS-1/ERS-2 tandem mode. The position of the ERS satellites is accurately measured because of the radar altimeter it carries.

This study is executed in the Waddensea north of the Netherlands. It consists of two main parts:

- an experiment with the XTI/ATI airborne SAR system of DLR, the E-SAR;
- a study to repeat-pass interferometry with ERS1/2 tandem data.

A lot of bad luck was encountered during the project. This caused considerable delay.

The E-SAR experiment was finally held on 9 and 10 June 1997 for two locations in the Waddensea: near the isle of Terschelling and near the isle of Ameland. For each day and for each location a number of XTI and ATI measurements were made. Unfortunately, no precise aircraft track could be reconstructed due to a DGPS failure. The data are therefore contaminated by aircraft motions that could not be corrected for. The best tracks have been selected for further processing.

Scenes 107 and 108 of the western part of Terschelling, recorded 9 June 1997 in XTI mode, were further processed to a DEM of the land area. The processing contains a large number of steps, some of which pose considerable technical difficulties. The precision of the final product was established by comparing to another DEM obtained with laser altimetry, and to some corner reflectors that were placed at known positions in the area. The accuracy of the XTI DEM ranges from about 1 m for flat areas to 3 m for forested areas. This figure compares well to values mentioned in the literature. For practical application in the Netherlands it is too poor, as DEMs generated with laser altimetry have an accuracy of about 15 cm. Differential XTI measures deformations with an accuracy of the order of millimetres, and this may offer practical applications. This is not studied within this project.

The perpendicular scenes 103 and 104 were recorded in ATI mode, also on 9 June 1997. They show the eastern part of Ameland and the Waddensea south of it. These scenes were further processed and combined to a map of the surface current vector on a 8×8 m^2 grid. The surface current must be corrected for the wind drift, for the movement of the Bragg scatterers, and for the azimuth displacement. The wind drift correction is assumed to be 10% of the wind speed at 10 m anemometer height. The Bragg waves have isotropic angular distribution since the E-SAR operates at X-band. The velocity contribution of Bragg waves moving towards the radar therefore cancels that of waves moving away from the radar. The azimuth displacement is 100 m at most.

The r.m.s. error in the current velocity is found to be 6 cm/s. The ATI flow field is compared to a model hindcast on a grid of approximately 160×440 m^2. The azimuth displacement is therefore neglected. The agreement between the two flow fields is good, certainly when taking into account that the model calculates the depth-averaged current whereas the ATI measurements yield the surface current. Remaining differences may be due to the coarse grid of the model or to inhomogenities in the wind drift correction. The ATI flow field on a 32×32 m^2 grid has been used as input in a wave-current interaction model. The simulated modulations in the radar cross section show good qualitative agreement with the observed ones, thus strengthening confidence in the radar measurements. ATI measurements may be used for validation and calibration of detailed (3D) flow models. Another application may be inspection of the flow field near structures in coastal waters and rivers.

From an ERS1/2 tandem pair recorded 9 and 10 May 1996 a coherence map of the isle of Ameland was constructed. This was compared to a land classification obtained from a digital topographic map and from field observations during the days of satellite overpass. Hardly any relation is found between coherence and land use, due to decorrelation caused by the effect of wind on the vegetation. The small size of the different land use parcels made it difficult to link the coherence map and these parcels. Even within 24 hours, a part of the area has decorrelated. The only exception is for some very dry parts with vegetation that is not influenced by the wind.

The airborne interferometric measurements were performed with a foreign (German E-SAR) system, because PHARUS, the Netherlands' airborne SAR, did not have any interferometric capabilities at that time. Meanwhile, some capabilities have been developed for PHARUS. An assessment of these capabilities, both XTI and ATI, and a comparison with the E-SAR results shows that it should be possible to use PHARUS for surface current mapping and DEM generation with satisfactory results.

Samenvatting

Een beeld dat is opgenomen met Synthetic Aperture Radar (SAR) is een complexe grootheid. Behalve het welbekende amplitude beeld bevat het ook fase informatie. Deze informatie wordt gebruikt in interferometrische toepassingen, een nieuwe loot aan de stam van de aardobservatie met radar. Interferometrische toepassingen zijn betrekkelijk nieuw en zeer veelbelovend. In deze studie worden drie technieken bestudeerd om hun bruikbaarheid in de kustzone vast te stellen:

- Across-track interferometrie (XTI);
- Along-track interferometrie (ATI);
- Repeat-pass interferometrie.

Bij XTI bestaat het SAR systeem uit twee antennes die boven elkaar bevestigd zijn, loodrecht op de vliegrichting. Het systeem neemt twee SAR beelden op hetzelfde tijdstip, maar vanuit een iets verschillende positie. Uit de metingen boven land kan een digitale hoogtekaart (Digital Elevation Map, DEM) worden gegenereerd. Bij ATI bestaat het systeem ook uit twee antennes, maar nu zitten de antennes boven elkaar, parallel aan de vliegrichting. Nu worden twee SAR beelden opgenomen vanaf dezelfde positie, maar op iets verschillende tijdstippen. ATI is gevoelig voor bewegende doelen, en boven water geeft ATI een kaart van de component van de stroming in de radar kijkrichting. Een SAR systeem voor repeat-pass interferometrie bestaat uit één antenne. De vliegroute wordt herhaald om een tweede SAR beeld op te nemen. Uit beide SAR beelden kan weer een DEM worden bepaald. De coherentie (correlatie) tussen de twee beelden neemt af met de tijd, afhankelijk van de eigenschappen van het oppervlak. Dit kan additionele informatie over het type terrein opleveren.

De kwaliteit van de interferometrische metingen hangt sterk af van de relatieve afstand tussen de twee antennes tijdens de metingen. Deze afstand heet de base line. XTI en ATI zijn alleen mogelijk met gevlogen systemen met twee antennes. De base line kan in dit geval eenvoudig worden opgemeten. Repeat-pass interferometrie is in principe ook mogelijk vanuit een vliegtuig, mits de baan en de stand van het vliegtuig voldoende nauwkeurig bekend zijn. De bekendste toepassingen maken gebruik van ERS beelden, in het bijzonder van de ERS-1/ERS-2 tandem mode. De positie van de ERS satellieten wordt nauwkeurig bijgehouden met de radar altimeter die aan boord is.

Deze studie is uitgevoerd in de Waddenzee in het noorden van Nederland, en bestaat uit twee hoofdbestanddelen:

- een experiment met de E-SAR, het gevlogen XTI/ATI SAR systeem van DLR;
- een studie naar repeat-pass interferometrie met ERS1/2 tandem mode data.

Het project werd door pech achtervolgd, waardoor een aanzienlijke vertraging is opgetreden.

Het experiment met de E-SAR is uiteindelijk gehouden op 9 en 10 juni 1997 op twee locaties in de Waddenzee: bij Terschelling en bij Ameland. Op iedere dag en voor iedere locatie zijn een aantal XTI en ATI metingen uitgevoerd. Helaas kon de baan van het vliegtuig achteraf niet goed gereconstrueerd worden wegens een fout in DGPS. De data bevatten daardoor storende effecten veroorzaakt door de bewegingen van het vliegtuig waarvoor niet gecorrigeerd kon worden. De beste gegevens zijn geselecteerd voor verdere analyse.

Opnames 107 en 108 werden opgenomen op 9 juni 1997 en tonen het westelijk deel van Terschelling. Deze opnames zijn verder verwerkt tot een DEM van het droge gedeelte. De verwerking telt een groot aantal stappen waarvan sommigen tot aanzienlijke technische problemen leidden. De nauwkeurigheid van het eindprodukt is vastgesteld door te vergelijken met een ander digitaal hoogtebestand opgenomen met laser altimetrie. Tevens waren in het testgebied corner reflectoren neergezet op bekende posities.

De nauwkeurigheid van de XTI DEM varieert van 1 m boven vlakke gebieden tot 3 m boven bossen. Dit komt overeen met nauwkeurigheden zoals ze in de literatuur worden genoemd. Voor praktische toepassingen binnen Nederland is de fout te groot, omdat de hoogte gemeten met laser altimetrie een nauwkeurigheid van 15 cm heeft. Met differentiële XTI kunnen deformaties bepaald worden tot op enkele millimeters. Hiervoor bestaan mogelijk praktische toepassingen, maar dat is niet binnen dit project onderzocht.

Opnames 103 en 104 werden in ATI mode opgenomen, eveneens op 9 juni 1997. Deze opnames staan loodrecht op elkaar en bestrijken het oostelijk deel van Ameland en de Waddenzee ten zuiden daarvan. Deze opnames zijn verder verwerkt tot een map van de stroomsnelheid en -richting aan het oppervlak op een rooster van 8×8 m^2. De oppervlakte stroomsnelheid moet gecorrigeerd worden voor de zogenaamde wind drift, voor de beweging van de Bragg golven en voor de azimut verplaatsing ten gevolge van de stroomsnelheid zelf. De wind drift correctie wordt verondersteld 10% van de windsnelheid op 10 m hoogte te bedragen. De E-SAR werkt met X-band, zodat de Bragg golven een isotrope richtingsverdeling hebben. De bijdrage aan de snelheid ten gevolge van Bragg golven die naar de radar toe bewegen valt daarom weg tegen die van Bragg golven die van de radar af bewegen. De azimut verplaatsing bedraagt maximaal 100 m.

De r.m.s. fout in de stroomsnelheid bedraagt 6 cm/s. Het ATI stromingsveld is vergeleken met een modelberekening op een rooster van ongeveer 140×440 m^2. De azimut verplaatsing kan daarom verwaarloosd worden. De overeenkomst tussen beide velden is goed, zeker gezien het feit dat het model de dieptegemiddelde stroomsnelheid berekent terwijl de ATI metingen de stroomsnelheid aan het oppervlak geven. Resterende fouten worden toegeschreven aan de grofheid van het modelrooster en aan inhomogeniteiten in de correctie voor de wind drift. Het ATI stromingsveld op een 32×32 m^2 rooster is gebruikt als input in een model voor golf-stromingsinteractie. De aldus berekende modulaties in de radar doorsnede komen kwalitatief gezien goed overeen met de waargenomen modulaties, hetgeen het vertrouwen in de ATI metingen versterkt. ATI kan gebruikt worden voor het kalibreren en valideren van gedetailleerde (3D) stromingsmodellen, en voor inspectie van het stromingsveld rond constructies langs kusten en in rivieren.

Uit een ERS1/2 tandem paar van 9 en 10 mei 1996 is een kaart van de coherentie bepaald voor Ameland. Deze is vergeleken met de landclassificatie uit de digitale topografische kaart en met veldwaarnemingen die zijn gedaan op de dagen dat de satelliet opnames gemaakt zijn. Er is nauwelijks enige relatie gevonden tussen de coherentie en het landgebruik wegens het decorrelerende effect van de wind op vegetatie. De kleine percelen met verschillend bodemgebruik maakte het moeilijk om het coherentie beeld aan deze percelen te koppelen. Zelfs binnen 24 uur is een deel van de gebieden gedecorreleerd, behalve enkele zeer droge delen waar de vegetatie weinig effect van de wind ondervindt.

De interferometrische vliegtuig metingen zijn gedaan met een buitenlands systeem (Duitse E-SAR), omdat PHARUS, de Nederlandse vliegtuig SAR, indertijd geen interferometrische mogelijkheden bezat. Inmiddels zijn er enkele interferometrische opties ontwikkeld, zowel XTI als ATI. Deze opties worden bekeken en vergeleken met de mogelijkheden van de E-SAR. Het blijkt dat het mogelijk moet zijn ook PHARUS te gebruiken voor het afbeelden van stroming aan het oppervlak en voor vervaardiging van hoogtekaarten, met voldoende nauwkeurigheid.

Chapter 1 INTRODUCTION

1.1 Historical overview

Synthetic Aperture Radar (SAR) has become one of the standard sensors for earth observation purposes. A SAR image is in fact an array of complex numbers. It is called a Single Look Complex (SLC) image. It consists of a real part and an imaginary part, or, equivalently, an amplitude image and a phase image. The amplitude part is the usual SAR image. It was realised by *Zebker and Goldstein* [1978] that radar interferometry is possible by combining two SLC images, provided that the (relative) position of the antenna during the measurements is known to a sufficient level of accuracy.

The first interferometric SAR systems were mounted in an aircraft and had two antennas. In such a configuration, the relative position of the two antennas is fixed and readily known. The antennas can be mounted next to each other, parallel to the flight path of the aircraft. This is called Along-Track Interferometry (ATI). The system makes two SAR images from the same position but at a slightly different time. The other possibility is to mount the antennas above each other, perpendicular to the flight path. This leads to Across-Track Interferometry (XTI). An XTI system also makes two SAR images, but at the same time and from a slightly different position. One can also do interferometry with only one antenna, by recording the same scene twice. This is called repeat-pass interferometry, in contrast with the single-pass two-antenna technique. A necessary condition is that the relative position of the antenna during the two flights, and hence the platform track, is known to a sufficient accuracy. As the two tracks will differ slightly, and as there always is a time lag between the flights, repeat-pass interferometry is a combination of ATI and XTI.

So far, single pass interferometric systems have only been implemented in aeroplanes. These systems are expensive, and world-wide only half a dozen systems exist. Recent developments in positioning using the Global Positioning System (GPS) enable repeat-pass interferometry with airborne systems, though this technique is still experimental. Repeat-pass interferometry from space is widely used. The European Remote Sensing (ERS) satellites carry radar altimeters that need accurate orbit information in order to interpret the measurements. The orbit of the ERS satellites is therefore well monitored by laser tracking. As a by-product, this orbit information can be used to perform repeat-pass interferometry on the C-band SAR images recorded by the Active Microwave Instrument (AMI) carried by ERS-1 and ERS-2.

One can therefore schematise the various types as follows:

- ATI (airborne)
- XTI (airborne)
- Repeat pass (spaceborne, airborne)

SAR interferometry is a promising technique for a number of application fields. With along-track interferometry (ATI) one can measure motions. Used over water, this means surface currents can be mapped with a high level of detail. The information can be used to validate and improve accuracy of hydrological observations and numerical models. Across-track interferometry (XTI) can be used above land for Digital Elevation Model (DEM) generation, deformation mapping and morphological studies. Both types of interferometry yield complex coherence measures, which give independent information about the surface and can be used for image classification purposes. Such applications are of special interest in coastal zones.

In the Netherlands considerable effort is spent on monitoring coastal areas. The littoral areas, including estuaries and intertidal areas, are of vital interest for coastal defence and from the point of view of ecology and nature conservation. Also in developing countries, the casualties and damage that can be caused by flooding stress the importance of coastal zone monitoring. Furthermore, for military operations there is a clear interest in techniques for mapping surface current and DEM generation of the coastal zone.

1.2 Aims and scope

The main aim of this project is to assess the potential of SAR interferometry for applications in coastal zones. X-band single-pass interferometry from the airborne E-SAR system of DLR is used for obtaining the ATI and XTI data. With ATI two antennas are placed on the longitudinal axis of the aeroplane, as mentioned before. This configuration results in two SAR images taken shortly after each other. Phase differences between these two images indicate displacements at the ground or at sea which can easily be translated into velocities. In this manner we get a detailed measurement of surface current. The results are compared with the current fields calculated using numerical models.

XTI has the two antennas placed next to each other perpendicular to the flight direction of the aeroplane. In this configuration the registered phase difference can be used to compute the angle and from that the height of objects on the ground. In order to evaluate the XTI DEMs they are compared with laser scanning data and corner reflectors.

Satellite interferometry is a combination of along-track and across-track interferometry because there will always be a time difference and a baseline component in across-track direction. Physical phenomena which have a short decorrelation time such as sea surface can therefore never be studied with satellite INSAR. In this study repeat pass interferometry with a tandem mission of ERS1 and ERS2 satellites (both using C-band) is used for studying coherence maps. Decorrelation phenomena hamper the extraction of height information from the interferogram, but on the other hand provide information on characteristic surface features and may therefore be used for land use mapping or mapping of land use change.

The area of interest is the Dutch Waddensea because a lot of elements are present that can benefit from interferometric studies. The Waddensea is a partially enclosed shallow sea, protected by barrier islands. Tidal processes play a dominant role, as water from the open sea moves in and out of the Waddensea following the tides. In this process, the bottom of the Waddensea is shaped into large tidal flats cut across by deep gullies. This topography is rather dynamic. If this process is to be understood, modelled, or forecast, it is necessary to have a good knowledge of the currents. The islands consist of sandy beaches and dunes, covered by vegetation on the inland parts. As the sand is also subject to erosion and deposition, by the sea and the wind, the islands themselves are also dynamic. The Waddensea has a socio-economic importance, in fishing, tourism, ferry transport and nature conservation. In combination with its dynamic nature, this implies a need for constant monitoring. With XTI, the topography of the area can be mapped and monitored, while with ATI, the currents can be mapped and monitored. For this study, two test areas on the islands of Terschelling and Ameland have been defined.

1.3 Project team

Table 1.1 lists the institutes and personnel involved in this project.

Contractors	Address	Personnel
Rijkswaterstaat, Survey Department (RWS-MD)	P.O. Box 5023 2600 GA Delft	E.J. Huising Y. Dierikx E. Vaessen J. Vogelzang
TNO Physics and Electronics Laboratory (TNO-FEL)	P.O. Box 96864 2509 JG The Hague	H. Greidanus R.J.P. van Bree J. Aardoom
International Institute for Aerospace Survey and Earth Sciences (ITC)	P.O. Box 6 7500 AA Enschede	G. Huurneman
Rijkswaterstaat, National Institute for Marine and Coastal Management (RWS-RIKZ)	P.O. Box 20907 2500 EX The Hague	J. Vogelzang

Table 1.1 Project team.

Note that J. Vogelzang moved from RIKZ to MD in 1998. The project manager is E.J. Huising. Since he left Rijkswaterstaat on 1 May 1999, project management was transferred to J. Vogelzang for the last few months.

1.4 Introductory remarks

The project consisted of the following elements:

- A small literature study in order to be prepared for the analysis of the interferometric data
- An experiment with an airborne SAR in ATI and XTI interferometric modes over two test areas in the Waddensea
- Processing of the data from the airborne SAR into current fields and DEMs
- Analysis and verification of the obtained current fields and DEMs, by comparison with data from other sources
- A study into the use of multi-pass interferometric satellite data for mapping and monitoring of the area

Project execution was hindered by a lot of bad luck. A first experiment with airborne SAR in the Waddensea was conducted in 1996. This experiment failed due to malfunctioning of a tape recorder, so no data were recorded. The second experiment was held in 1997. Due to GPS problems, the aircraft track could not be reconstructed to the required precision. This held up processing and delayed interpretation of the measurements. Finally, the flow field calculations had to be redone, due to the neglect of the one hour time difference between Central European Summer Time (local time during the experiment with airborne SAR) and Central European Time (used as input for the flow model).

Originally, the SAR flight was planned simultaneous with an HF radar deployment on Terschelling in order to compare maps of the surface current. This HF deployment was part of a suite of demonstration projects financed by Rijkswaterstaat. These projects had their own goals. They were also hindered by bad luck. It proved to be impossible to synchronise two delayed projects. Finally, the HF radar deployment on Terschelling ended a month before the 1997 flight. Note that if the HF radar deployment had been on schedule, no comparison would

have been possible since the first flight failed, and that if the HF radar deployment were simultaneous with the second flight, no comparison would have been possible since the Terschelling ATI data were of poor quality.

Chapter 2 contains a brief general description of the principles behind interferometric measurement techniques. Three different techniques are identified: along-track, across-track and repeat-pass interferometry. Some potential applications are mentioned.

Chapters 3-5 deal with the experiment with airborne SAR in which across-track and along-track interferometry was studied. Chapter 3 describes the experiment with the airborne SAR and its results. Information is given on the SAR sensor, the meteo conditions and the results. Also the available ground measurements are presented.

In chapter 4 the across-track interferometric measurements are studied. Two scenes are selected and processed to a Digital Elevation Model of a part of the isle of Terschelling in the Waddensea. This is a complicated process. It is described in detail, and possible alternatives in the processing steps are identified and discussed. The elevation model extracted from the radar measurements is carefully compared to an elevation model obtained from laser altimetry. The latter model has an accuracy of about 15 cm. Also some corner reflectors were located at known positions. The analysis shows that the accuracy of interferometric radar height measurements is about 1 m for flat areas like beaches and increases to more than 3 m in forested areas. These figures compare well to similar figures in the literature, but the accuracy is too poor compared to laser altimetry.

Chapter 5 deals with the along-track interferometric measurements. The two best scenes are processed to a flow map of the area South of the isle of Ameland in the Waddensea. The processing steps are described in detail. The resulting current velocities are corrected for wind drift effects. No correction for the movement of the Bragg wave scatterers is needed as these are distributed isotropically at X-band. The flow map is compared to a model prediction. The general flow pattern is reproduced, though there are some differences. As a consistency check, the interferometrically measured flow field is used as input in a wave-current interaction simulation model. This yields predictions of the modulations in the intensity images. These compare well with the actual intensity images, thus strengthening confidence in the technique. It is concluded that along-track interferometry yields flow maps at very high resolution. However, the problem of azimuth shift must be solved in order to fully exploit the resolution.

Chapter 6 reports on the satellite multi-pass interferometric study. The coherence between two radar images will decrease as function of time. Here it is attempted to find a relation between coherence and land class. The study is performed for a part of the isle of Ameland. No clear relation is found, due to fast decorrelation caused by wind influence. Temporal decorrelation is low enough only in very dry areas.

In chapter 7 the interferometric methods studied here for obtaining digital height maps and surface current maps are compared to other methods in terms of costs and accuracy. Also the implications for the operational use of the PHARUS airborne SAR system are discussed.

This report ends with some conclusions and recommendations in Chapter 8.

The results of this studied were presented in 1999 at the International Geoscience and Remote Sensing Symposium (IGARSS '99) in Hamburg, Germany [*Greidanus et al, 1999a, 1999b*].

Chapter 2 INTERFEROMETRY

This chapter on the principles of SAR interferometry is taken from TNO report number FEL-93-B084 titled "SAR land subsidence monitoring" by M.W.A. van der Kooij , D. Van Halsema and W. Groenewoud. [Van der Kooij et al., 1993].

An interferometric SAR system (INSAR) basically consists of two SAR antennas. Both antennas record amplitude and phase data. A phase preserving SAR processor transforms these data into two separate complex radar images of the same area. These images will be quite similar. However, the phase of corresponding pixels will be slightly different. The processing of these phase differences, the correction for platform attitude and the extraction of various parameters such as topography and velocity is called interferometric processing. An image of the phase differences is called an interferogram. In the next sections the principles behind along-track, across-track and repeat-pass interferometric measurements will be discussed.

2.1 Along-track interferometry (ATI)

Figure 2.1 gives the principle of along-track interferometric SAR (ATI-SAR) on board of an aircraft. The system consists of a front-antenna and an aft-antenna. The connecting line between the two antennas is called the baseline B. The x-component of the baseline (along the line of flight) is important for ATI. The situation during recording is shown. Both antennas alternately transmit and record radar radiation with wavelength λ. Let's suppose that part of the radiation is backscattered from an object moving with velocity u towards or away from the radar. Because of the positioning of the antennas a small delay Δt has been built in between the recording of the two images. During this time interval the object will have moved a little bit towards or away from the radar. This will cause a phase difference φ between corresponding pixels of the images that gives information on the velocity u of the object towards or away from the radar.

The phase difference is given by

$$\Delta\varphi = \frac{4\pi}{\lambda} u\Delta t = \frac{4\pi}{\lambda}\frac{u}{V} B_x \,, \tag{2.1}$$

where V is the velocity of the aircraft.

It is important to realise that aircraft yaw and pitch will cause baseline components in y- and z-direction (see Figure 2.1) and thus will give additional phase differences. These can be corrected for if the attitude of the aircraft is accurately measured. A calibration of the phase difference is necessary before absolute velocity measurements are possible. Thus the exact locations of the antennas and the cable delays should be measured with high precision.

Possible applications are the detection of moving objects, the mapping of water currents and measurement of directional wave spectra [*Goldstein and Zebker*, 1987; *Marom et al.*, 1991; *Scheiber*, 1998]. The measured speed is always in the radial direction, so two tracks at an angle are needed to compose the current vector. The decorrelation time of the interferogram is very small so even water does not decorrelate.

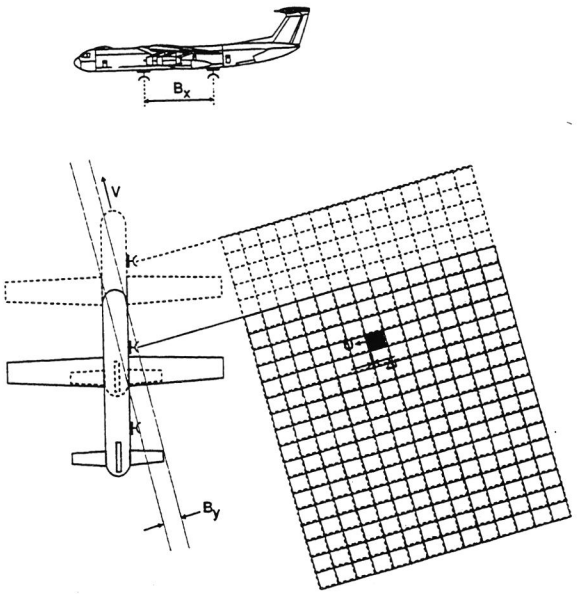

Figure 2.1 Along-track interferometry.

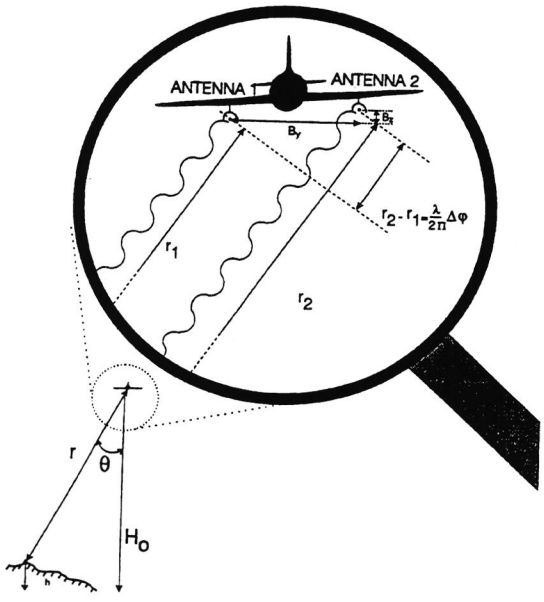

Figure 2.2 Across-track interferometry.

2.2 Across- track interferometry (XTI)

Figure 2.2 gives the principle of across-track interferometric SAR (XTI-SAR) on board of an aircraft. The system consists of two SAR antennas separated by a baseline B perpendicular to the flight direction. The baseline consists of a horizontal (B_y) and a vertical (B_z) component. Sometimes one antenna transmits and both

antennas record. In case of the DLR E-SAR system employed in this study both antennas transmit and record. After SAR processing two almost identical SAR images are obtained.

The phase difference is a measure for the direction θ of the incoming radar radiation. It is given by

$$\Delta\phi = \frac{4\pi}{\lambda}(B_y \sin\theta - B_z \cos\theta), \tag{2.2}$$

with $h = H_0 - r\cos\theta$. The equation above applies to the DLR E-SAR. If only one antenna transmits the factor is 2π instead of 4π. H_0 is the reference height, h is the local height above the reference height, and r is the range.

By measuring range, incidence angle, the exact flight track and the timing of the measurements, the 3-dimensional location of the scatterer is determined. This enables generation of a height map. However, the phase difference is measured with an ambiguity of 2π. This means that the resulting height map will also contain ambiguities. Another important point to mention is the impossibility to distinguish between errors in the aircraft roll measurements and a slope of the topography. Accurate attitude measurements are of great importance to airborne across-track interferometry.

2.3 Repeat pass interferometry

Figure 2.3 shows another possibility for across-track measurements. It is the same geometry as in Figure 2.2 but in this case only one SAR antenna is available on the platform. The second SAR image is obtained in a repeated pass some time later. The horizontal and vertical separation between the passes form the baseline. The phase difference has the same form as for across-track interferometry. It therefore satisfies (2.2).

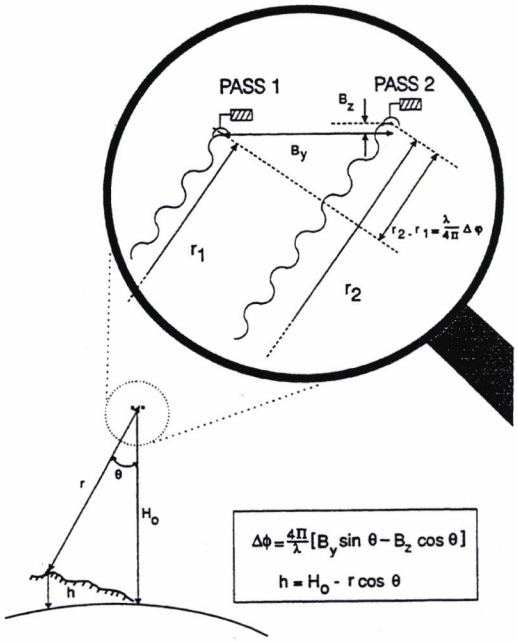

Figure 2.3 Repeat-pass interferometry

In fact this technique combines across-track and along-track interferometer measurements. The long time interval Δt between the recordings of the SAR data gives a sensitivity for very slowly moving objects (or, equivalently, for very small elevation changes or horizontal shifts of mm's or cm's between the recording of the images). The ability of SAR to measure phase difference with high accuracy offers interesting possibilities for very accurate mapping of relative elevation changes or horizontal shifts on a large scale with high resolution.

A decorrelation in the interferograms occurs when the backscatter properties of the object changes. This happens if the baseline and the time between the images is too large. The latter differs from object to object. Some examples of this method are given by *Prati et al.* [1992].

Chapter 3 E-SAR EXPERIMENT

3.1 The SAR sensor

The SAR sensor used for this experiment was the airborne E-SAR (Experimental SAR) owned and operated by the Deutsche Forschungsanstalt fur Luft- und Raumfahrt e.V. (DLR). The E-SAR is operated by the Institut fur Hochfrequenztechnik in Oberpfaffenhofen, Germany. It has multi-frequency, polarimetric and interferometric capabilities, but in this experiment only the X-band VV interferometric mode was used [*Horn*, 1996]. The parameters of the SAR that are relevant to this experiment are listed in Table 3.1. The definition of the baseline components was already given in Figures 2.1 and 2.2.

Frequency	9.6 GHz	Bandwidth	100 MHz
Wavelength	0.0312 m	Sampling rate	100 MHz
Polarisation	VV	PRF	1000 Hz
Peak power	2.5 kW	Baseline x	0.46023 m
Receiver noise	4.0 dB	Baseline y	0.37188 m
Antenna gain	17.5 dB	Baseline z	1.56355 m
Azimuth beam width	17°	Resolution slant range	1.5 m
Elevation beam width	30°	Resolution azimuth	0.6 m

Table 3.1 E-SAR parameters during the experiment.

The E-SAR is flown on a Dornier 228 turboprop aircraft. Three X-band interferometric antennas are mounted on the right side of the aircraft: two on the lower side and one higher up. In ATI-mode, the two lower antennas are used to form an interferometric pair. In the XTI-mode, the upper antenna is combined with one of the lower antennas. The motion data of the aircraft are measured and recorded, in order to be able to accurately reconstruct the flight path and the aircraft attitude. Both INS (Inertial Navigation System) and DGPS (Differential Global Positioning System) data are used and integrated.

During the measurements, there is an on-board quick-look facility to monitor the quality of the data. The quick-looks remain available on hard-copy. After an experiment, the raw SAR data are first processed to so-called survey images with limited accuracy. The survey images, together with the (low resolution) quick looks, can be used to select data for subsequent precision processing. In the precision processing, the raw SAR data and the motion data that have been recorded are converted into the final high resolution, high quality SAR image product (SLC interferometric image pairs in this case). The SLC images are motion corrected, resampled to a regular grid in slant range and corrected for a number of instrumental effects. The data are processed to a reference attitude of zero roll, pitch and yaw. No autofocussing is applied. The SLC interferometric image pairs, together with annotation, are the final deliverables by DLR.

In XTI mode, the height ambiguity of the data (corresponding to 2π interferometric phase) varies from 15 m (near range) to 40 m (far range). The relative height resolution due to aircraft roll is claimed to be of the order of 0.5 m. This is only in the optimal signal-to-noise case; in cases of low signal, the height resolution will deteriorate.

3.2 Experimental setup

During the measurement campaign with the E-SAR, a number of scenes over the islands of Ameland and Terschelling in the Dutch Waddensea were recorded. On Terschelling, a scene was defined on the western tip of the island, covering the town of West Terschelling, the surrounding area, and the adjacent intertidal region to the south. Distributed within the scene, corner reflectors were placed on four locations to serve as reference targets. On Ameland, a scene was defined on the eastern tip of the island, containing dunes, beaches and intertidal areas. No corner reflectors were deployed on Ameland. Both scenes were repeatedly imaged in XTI and ATI modes, with the acquisition times for the XTI focused on low tide (when most of the land is exposed), and for the ATI on rising tide and dropping tide (when currents are maximal). A total of 12 scenes was ordered from DLR.

A Novatel GPS receiver was employed in the aircraft which recorded the GPS L1 signal in Flykin format. The flights took place from Groningen airport, where a DGPS ground reference station was deployed by DLR (Novatel, L1, Flykin). Another DGPS reference station was deployed on Terschelling; this one recorded L1/L2 in Rinex format. The corner reflector absolute positions were measured with DGPS accuracy.

The first experiment was carried out in the period 15-22 October 1996. In first instance it appeared to be successful, but later it turned out that the data had not been properly recorded on tape and could not be used. Therefore, it was decided to perform a second experiment. Since this meant an unexpected doubling of the costs associated with flight preparation, flight execution, placing and removing of corner reflectors, etc., this had significant implications on the project. More of the project effort has been allocated to the experiment than originally planned, at the cost of literature and feasibility studies and data analysis.

Scene	Date	Start Time	ATI	XTI	Amel	Ters	Track	Track	Look dirn	Altitude	Squint	Gnd Spd	Tide
	(6-97)	(UTC)					nr.	(deg)	(Nominal)	(m)	(deg)	(m/s)	
101	9	15:25:59	A			T	5	*269,946	N	*3154,93	*-0,64251	*81,2083	Falling
102	9	15:32:27	A			T	6	358,317	E	3157,00	3,99402	89,0746	Falling
103	9	15:54:07	A		A		7	253,967	N	3155,85	-2,93075	80,2129	Falling
104	9	16:03:04	A		A		8	343,636	E	3157,01	2,97278	83,7709	Falling
107	9	16:39:17		X		T	2	1,618	E	3160,98	4,76112	81,7812	Fa--Lo
108	9	16:52:19		X		T	1	270,412	N	3158,84	-1,18659	81,1903	Low
110	9	17:39:05		X	A		3	256,797	N	3157,42	-2,74833	81,9993	Low
111	9	17:49:26		X	A		4	343,316	E	3156,48	3,66033	81,1103	Low
201	10	07:00:09	A			T	5	269,327	N	3158,51	0,96430	81,4216	Rising
202	10	07:08:54	A			T	6	2,156	E	3160,74	27,06520	83,1461	Rising
203	10	07:29:22	A		A		7	257,868	N	3160,11	0,39244	80,9847	Rising
204	10	07:38:14	A		A		8	344,358	E	3161,71	1,30219	79,7687	Rising
206	10	07:58:57		X		T	2	357,634	E	3160,44	0,74472	81,0445	Ri--Hi

Table 3.2 Overview of precision processed scenes. *: Values for channel 1; those for channel 2 differ slightly.

The second experiment took place on June 9-10, 1997. This experiment was for the most part successful, with the exception of the DGPS aircraft motion data registration. A total number of 18 scenes was recorded. On the basis of the quick-look and survey processed data, 12 scenes were selected for precision processing. The first precision processed scene was delivered by DLR in March 1998. Table 3.2 lists all precision processed scenes that were delivered by DLR. Scene 206 is a "bonus" and brings the total to 13 scenes.

During the precision processing at DLR it turned out that the DGPS data were not suitable for further use, due to format problems. No reliable DGPS flight track could be reconstructed. Therefore, the flight track for which the SAR data are corrected is based on INS and GPS only. Discontinuities occur in this flight track, related to aircraft turns, satellite configuration changes, etc. As a consequence, the accuracy of the flight track is less than expected, and also less than needed for high-quality interferometric results as will become clear later in this report.

3.3 Meteo conditions

Meteo conditions affects an airborne radar experiment above sea both at flight and at sea level. The wind condition at flight level influences the squint and look angle of the radar. It also affects the flight track. Humidity and temperature conditions may result in ice coverage of the sensor. The meteo conditions at the sea surface influences the radar backscatter signal. Low wind speed results in a smooth sea surface and a low backscatter signal, whereas high wind speed results in a foam-covered sea surface without any features.

Meteo condition forecasts were obtained from the Maritieme Meteorologische Dienst (MMD) and airport Eelde. Both forecasts are based on output of the High Resolution Limited Area Model (HIRLAM) operated by the KNMI. The MMD forecast is more dedicated to the sea level meteo conditions whereas Eelde is at flight conditions. The forecast is updated every six hours. Relevant parameters for the experiment are wind force, wind direction, and temperature at flight level.

Wind speed and direction data were obtained from meteo stations Hoorn (Terschelling) and Schiermonnikoog. No meteo data from Ameland itself is available. Meteo station Hoorn is regarded as representative for the test area, since it is located at 1 m above sea level. Its geographical co-ordinates are 53° 23′ N and 5° 21′ E. The measurements are taken at 10 m altitude (11 m above sea level) with no obstacles present in a radius of minimal 100 m. This guarantees undisturbed wind flow conditions. The data consists of the wind speed averaged over a 10 minutes interval before the whole hour and the instantaneous wind direction. Table 3.3 gives some values during the radar measurements.

Date and time	Wind at Hoorn (knots / degrees)	Wind at Schiermonnikoog (knots / degrees)
9 June 17:00	10 / 260	14 / 280
9 June 18:00	12 / 290	12 / 280
9 June 19:00	10 / 290	12 / 280
10 June 8:00	8 / 060	6 / 050
10 June 9:00	8 / 080	6 / 070

Table 3.3 Wind speed and direction data of 9/10 June 1997 at Hoorn (Terschelling) and Schiermonnikoog. Wind speed is averaged over ten minutes interval, wind direction is instantaneous. One knot equals about 0.515 m/s.

3.4 XTI measurements

Five across-track scenes were obtained from DLR, two of Ameland and three of Terschelling. These scenes are shown in Figures 3.1 - 3.5. Both intensity (left) and coherence (right) are plotted for each scene. The coherence is produced with the uncorrected phase.

Looking to the ten images in Figures 3.1 - 3.5, two things can be remarked.

1. Almost all of the coherence images contain dark (or bright) bands parallel to the cut off edges on top and bottom of the images. These are due to phase errors caused by aircraft movements that could not be corrected for.
2. Some areas in the coherence image correlate with low signal areas because of low SNR.

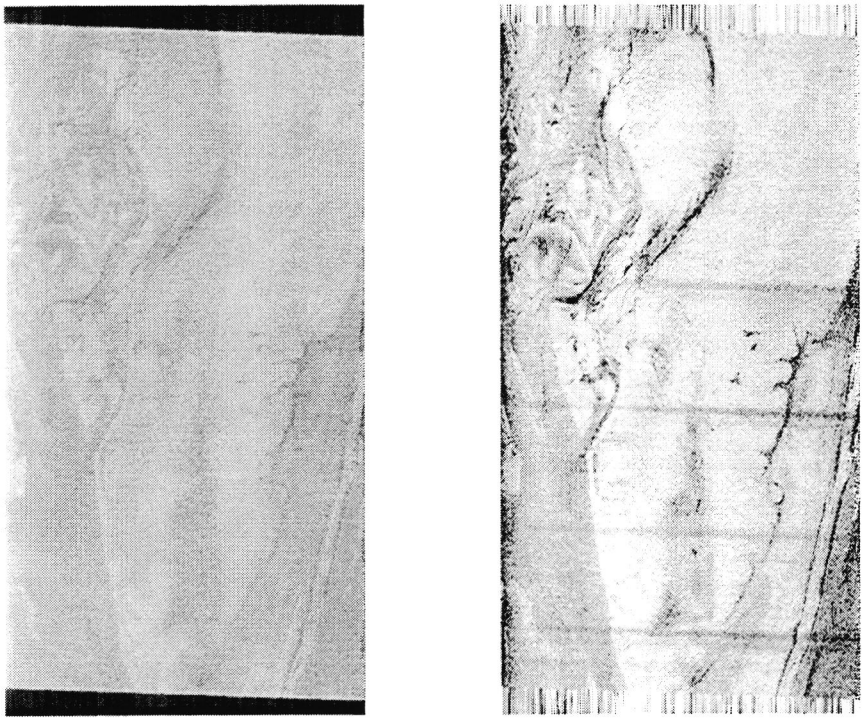

Figure 3.1 Scene 110 of Ameland. Intensity is shown in the left panel, coherence in the right panel.

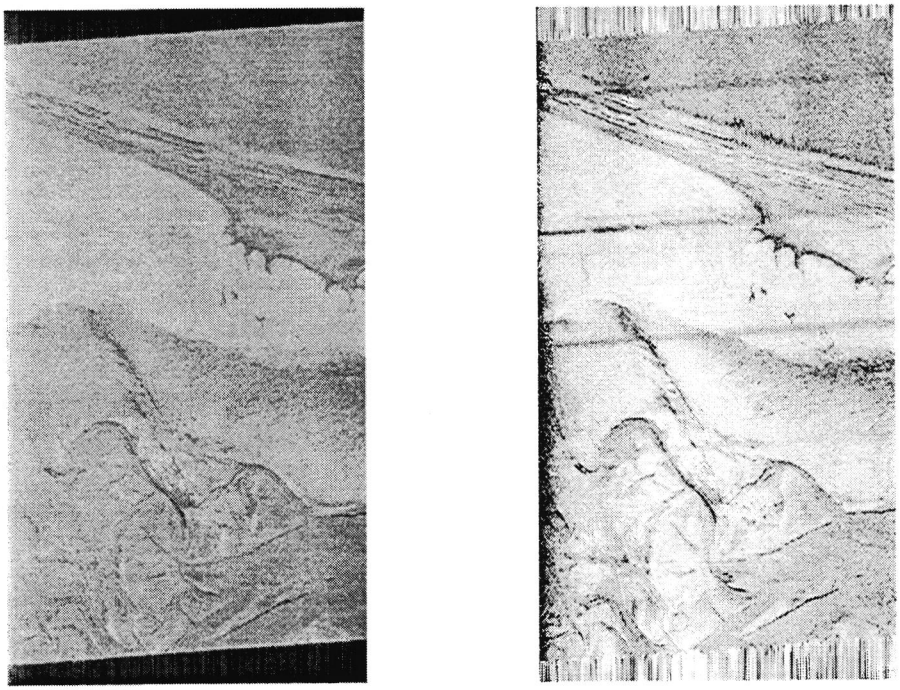

Figure 3.2 As Figure 3.1, but for scene 111 of Ameland.

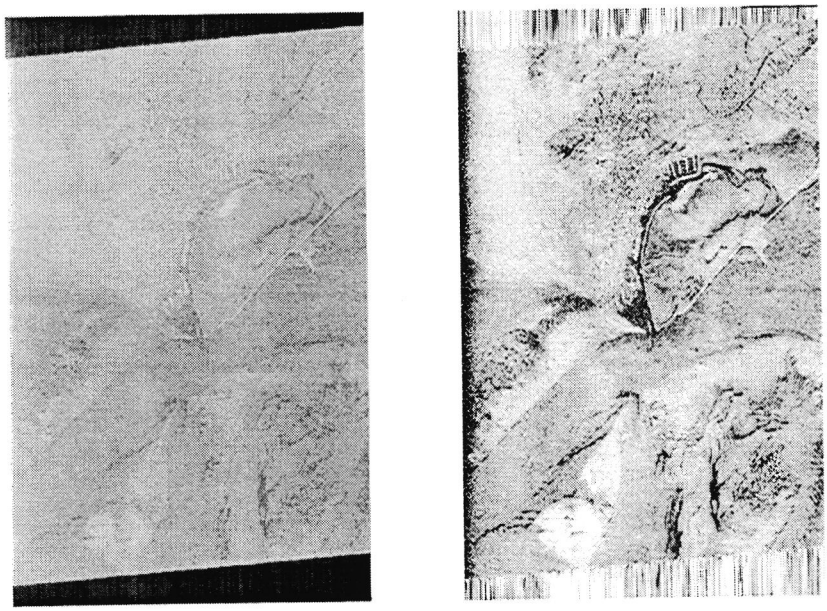

Figure 3.3 As Figure 3.1, for scene 107 of Terschelling.

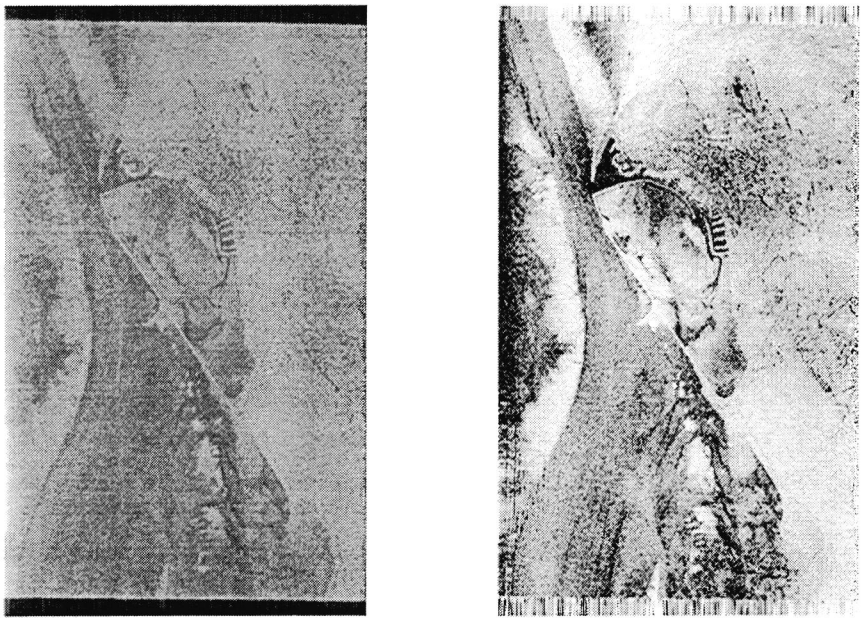

Figure 3.4 As Figure 3.1, for scene 108 of Terschelling.

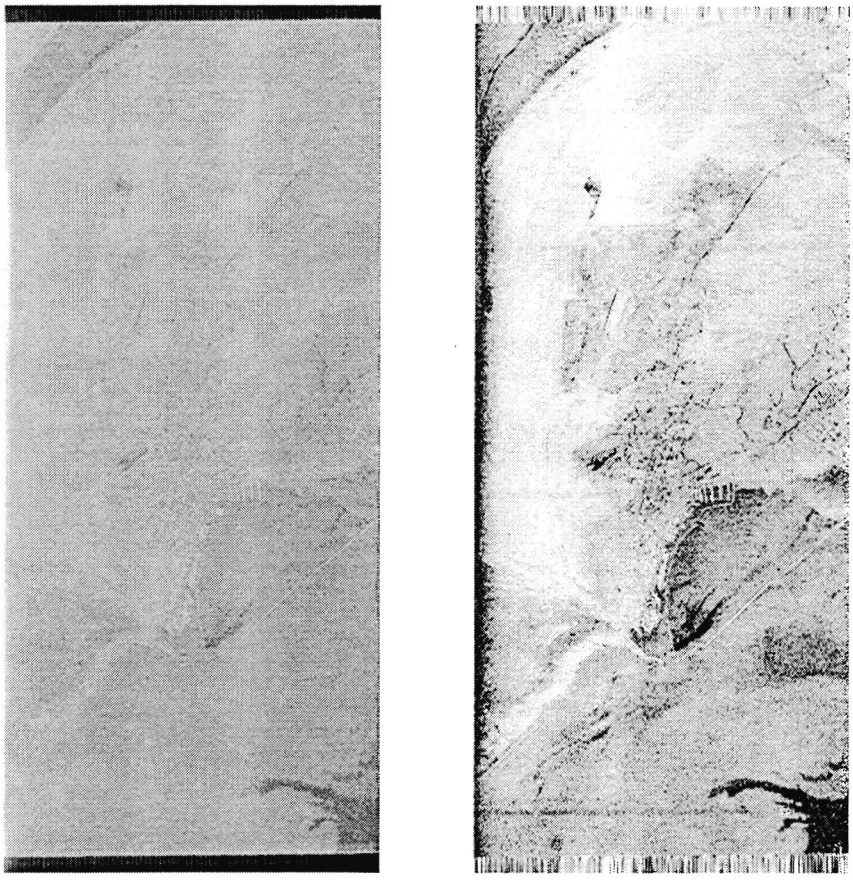

Figure 3.5 As Figure 3.1, for scene 206 of Terschelling.

3.5 ATI measurements

A total number of eight along-track scenes were obtained, four of Terschelling and four of Ameland. The best results were obtained from scenes 103 and 104 that were recorded on June 9 above Ameland. The phase images are shown in Figure 3.6. Other scenes contain much distortion from aircraft movements that could not be corrected for.

Scene 103 (left panel of Figure 3.6) has flowing water on the left hand side and land on the right hand side. The bright area just left of the centre is a phase jump of 2π. It occurs at the highest velocity of the current. This will be corrected for later on. The land on the right has a nearly constant phase. The "Wadden" (exposed tidal flats) are visible. Scene 104 (right panel of Figure 3.6) has flowing water at the bottom and land at the top. A phase jump is also visible at the edges of the "Wadden". The aeroplane flew from bottom left to top left in both images in Figure 3.6.

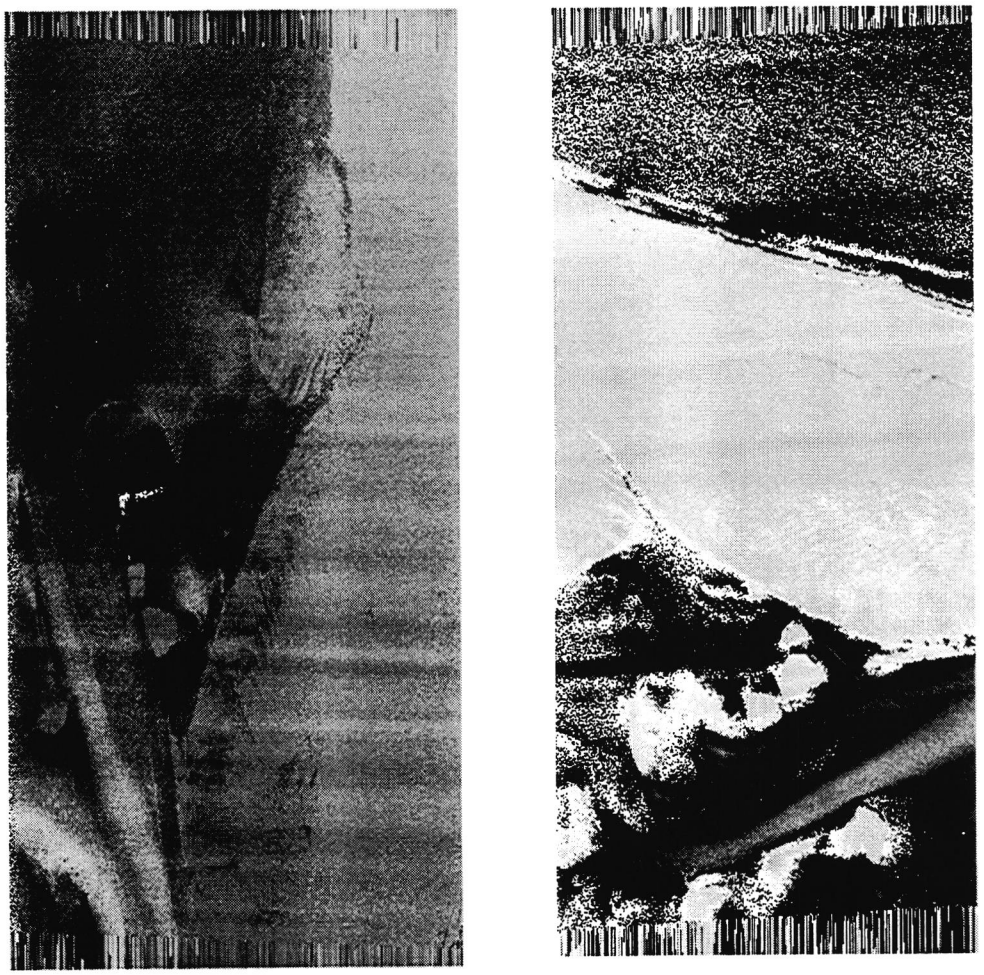

Figure 3.6 Phase images for scene 103 (left) and scene 104 (right).

3.6 Depth and flow map

Available soundings of the complete Waddensea area were interpolated to a digital map on a 20 × 20 m^2 grid by the National Institute of Marine and Coastal Management of Rijkswaterstaat (RWS-RIKZ). Figure 3.7 shows a part of this map for the area of interest. The isle of Ameland is visible as the black area at the top of the figure. Note the discontinuities in the coast line of Ameland and in the gully in the upper right of the figure. These are probably due to the fact that the soundings were recorded in different years, each set having its own systematic error. The two gullies south-east of Ameland are clearly visible. Figure 3.8 and Figure 5.7 in chapter 5 contain depth contour lines. These were obtained from this map using a simple approach with bilinear interpolation.

Current fields may be calculated using numerical models. For this study, RWS-RIKZ and ALKYON made hind-casts of the depth-averaged current using the "Waddenzee" model. This model is based on the well-known WAQUA system [*Leendertse*, 1967]. The shallow water equations are solved on a curvilinear staggered grid. The effect of wind is included, but the effect of atmospheric pressure differences not. The model receives its boundary conditions from a similar model on a greater scale. Figure 3.8 shows the model result for Ameland at 18:00 UTC (16:00 local time), just between recording of images 103 and 104. In the area of interest, the model grid size is about 440 m in the east-west direction and about 170 m in the north-south direction. The water is flowing towards the North-east. The strongest currents are found in the two gullies. These are indicated by the depth contour lines. The magnitude of the current is up to 0.87 m/s.

Figure 3.7 Depth map of the test area near Ameland.

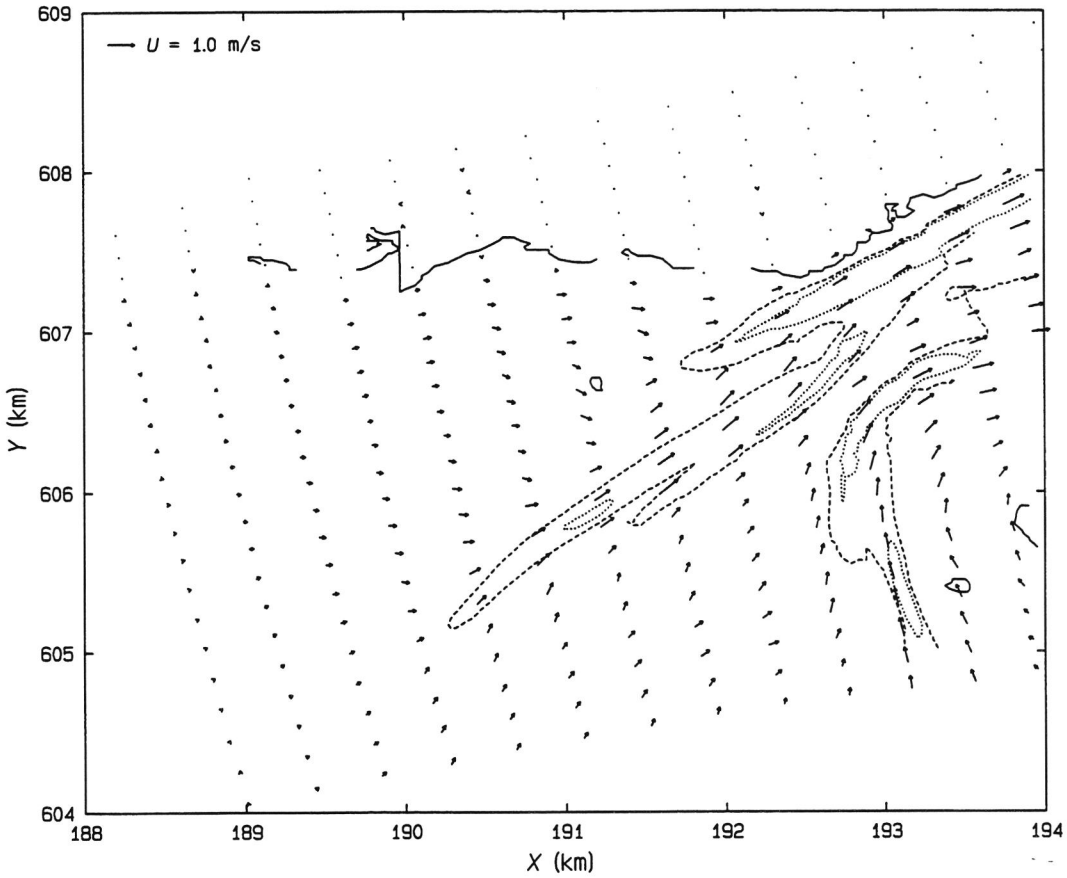

Figure 3.8 WAQUA hindcast of depth-averaged flow on June 9, 1997 at 18:00 UTC. The depth contour lines are at 0 m (solid curves), -2.5 m (dashed curves), and -5 m (dotted curves).

Chapter 4 XTI ANALYSIS

4.1 Introduction

This chapter describes how the XTI data gathered during the E-SAR experiment were processed to digital elevation models (DEMs). These will be compared to a DEM obtained from laser altimetry in order to assess the accuracy of DEMs generated by XTI.

The processing is complicated and involves quite a number of steps:

- Flat earth correction
- Phase unwrapping (2 methods tried)
- Phase to height conversion
- First trend correction
- Ground range transformation (3 methods tried)
- Geocoding
- First comparison
- Second trend correction
- Final comparison.

The first five steps are part of the DEM generation and will be covered in section 4.2. The resulting DEMs are presented and discussed in section 4.3. In the last four steps the XTI DEMs are compared to the laser DEM. This is described in section 4.4. The main conclusions are summarised in section 4.5.

Each of the processing steps will be addressed to separately. Some need only one sentence, others require more elaborate description. Many intermediate results will not be shown. As indicated in the list above, more than one approach is possible in some processing steps. In those cases the alternatives are discussed and the best method is selected. The ground range transformation has three alternatives, the best of which will be identified in the final comparison.

4.2 DEM generation

4.2.1 Flat earth correction

An across-track interferometer is sensitive to height differences. As stated before, the phase difference $\Delta\varphi$ caused by a pathlength difference of the received signal from a flat earth $(r - r')$ satisfies (see Figure 4.1):

$$\Delta\varphi = \frac{-4\pi}{\lambda}(r - r') = \frac{-4\pi}{\lambda}(B_z \cos\theta - B_y \sin\theta), \tag{4.1}$$

where λ is the wave length and θ the angle of incidence. The path length difference (phase difference) depends on the angle of incidence of the radar beam and of the baselines in y- and z- direction. The number of 4π is due to the fact that both antennas of the E-SAR emit and receive.

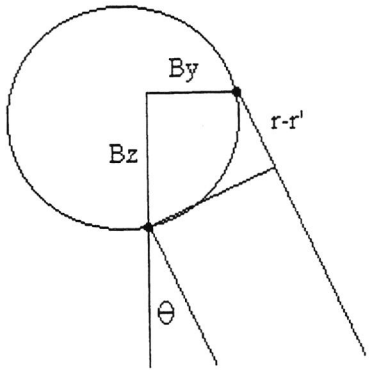

Figure 4.1 XTI geometry.

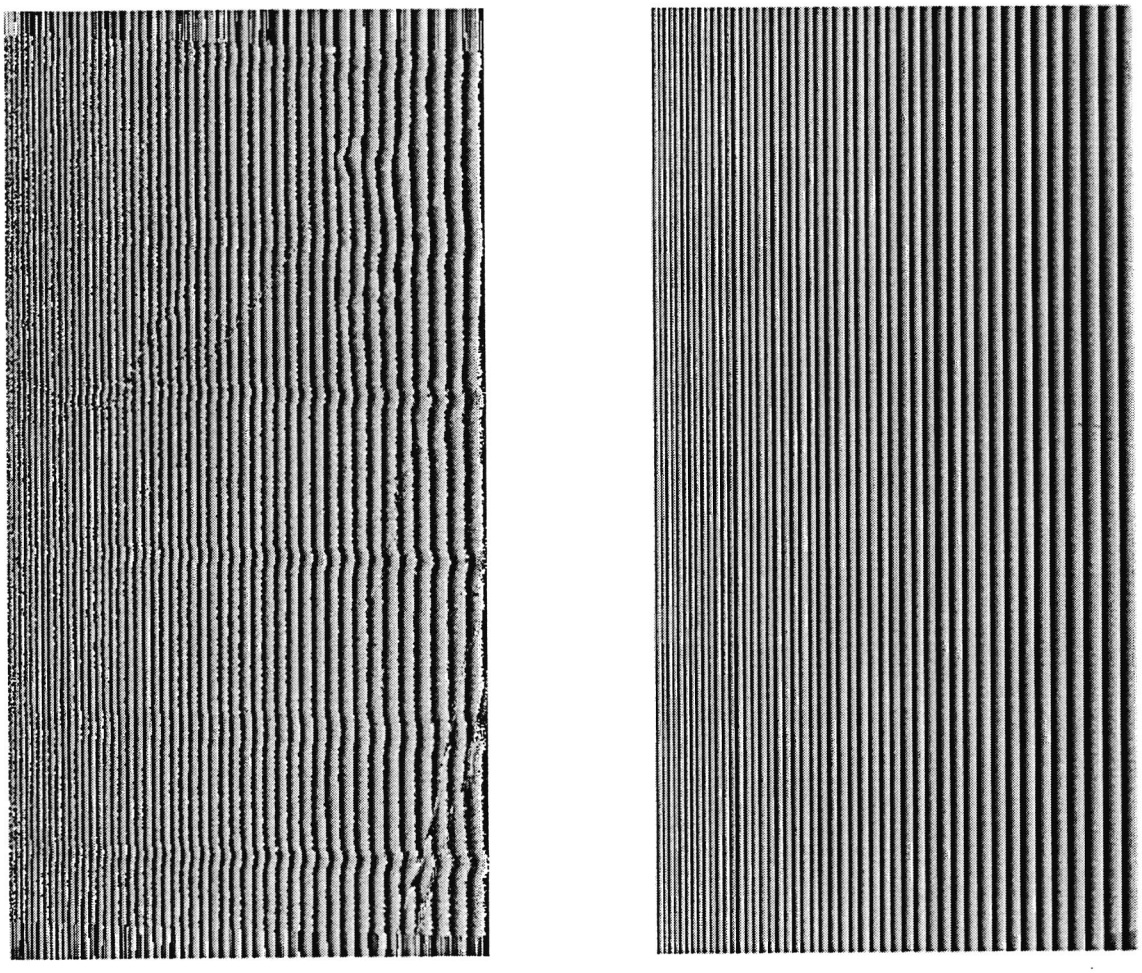

Figure 4.2 Uncorrected phase image (left) and flat earth correction (right). The range direction is from left to right.

The phase difference $\Delta\varphi$ grows with increasing θ, and because of the 2π ambiguity the phase difference will have "fringes" in the range direction as shown in Figure 4.2. There are also fringes due to height differences but those cannot be seen properly in the phase image because this effect is much smaller. Therefore a correction must be made, a flat earth correction. From the phase image an estimated fringe pattern of a flat earth is subtracted (see Figure 4.2), making visible the fringes caused by height differences.

The phase difference lies between -π and +π. After flat earth correction only fringes caused by height differences and currents remain in the images.

4.2.2 Phase unwrapping

The next step is to remove the remaining fringes by introducing a continuous phase without 2π discontinuities. This is called "phase-unwrapping". Phase unwrapping is a very complex and difficult aspect of interferometry ("art rather than science"). A number of algorithms has been proposed to do the job. This can be difficult for two reasons:

- very complex structures on the earth, like very steep hill sides or by multibounce objects;
- artefacts in the phase data caused by hardware faults, low signal to noise ratio (SNR), or by aeroplane movements.

In our case problems are caused mainly by aircraft movements. This will become clear later on from the unwrapped phase data. Two different unwrap algorithms were tried:

- a multi resolution and multigrid phase unwrapper written in MATLAB by P.T.A. van den Hout at TNO-FEL [*Van den Hout*, 1997];
- the least square phase unwrapper of PCI.

All five XTI scenes shown in section 3.4 were unwrapped. Scenes 107 and 108 of Terschelling were selected for further processing. The other scenes contained too much errors due to aircraft movements. Figures 4.3 and 4.4 show the results for scenes 107 and 108, respectively. The left panel shows the phase image after flat earth correction, the right panel the image after phase unwrapping using the algorithm of *Van den Hout* [1997].

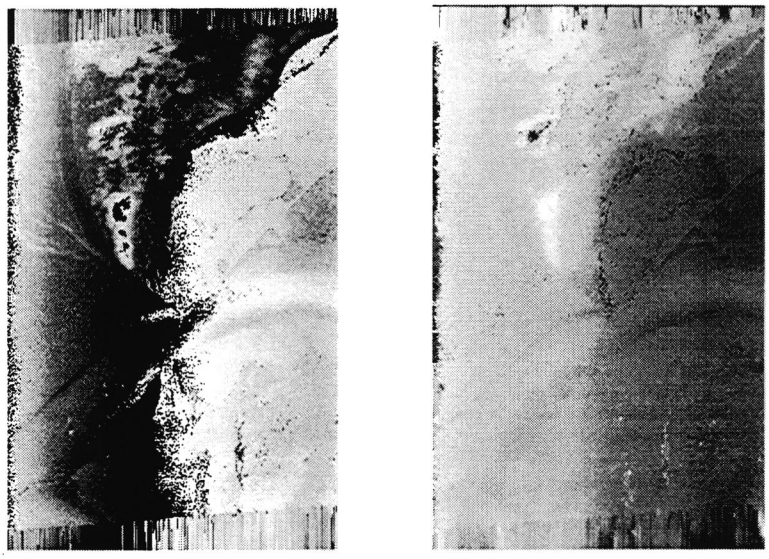

Figure 4.3 Scene 107 of Terschelling. The left panel shows the phase image after flat earth correction, the right image shows the unwrapped phase using the algorithm of *Van den Hout* [1997].

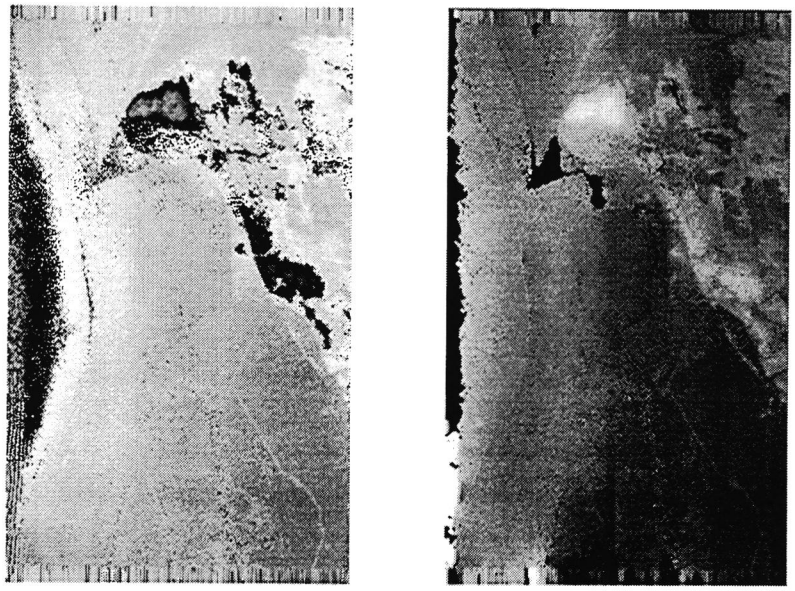

Figure 4.4 As Figure 4.3, for scene 108 of Terschelling.

In Figure 4.3, some areas with low SNR are masked in the flat earth corrected image (left panel) as indicated by the dark and dotted areas. Also some phase differences due to currents at sea are visible. Scene 108 was flown perpendicular to scene 107. Sometimes "boundaries" are visible in the phase unwrapped images (notably at the bottom of the right panel of Figure 4.4). These are due to the software which calculates the phase in blocks of 257 × 257 pixels. In the end the 6 or 8 blocks have to be levelled. This problem can in principle be solved by calculating the scene as a whole. However, this takes a lot of effort for rewriting the software, and was considered outside the scope of this project.

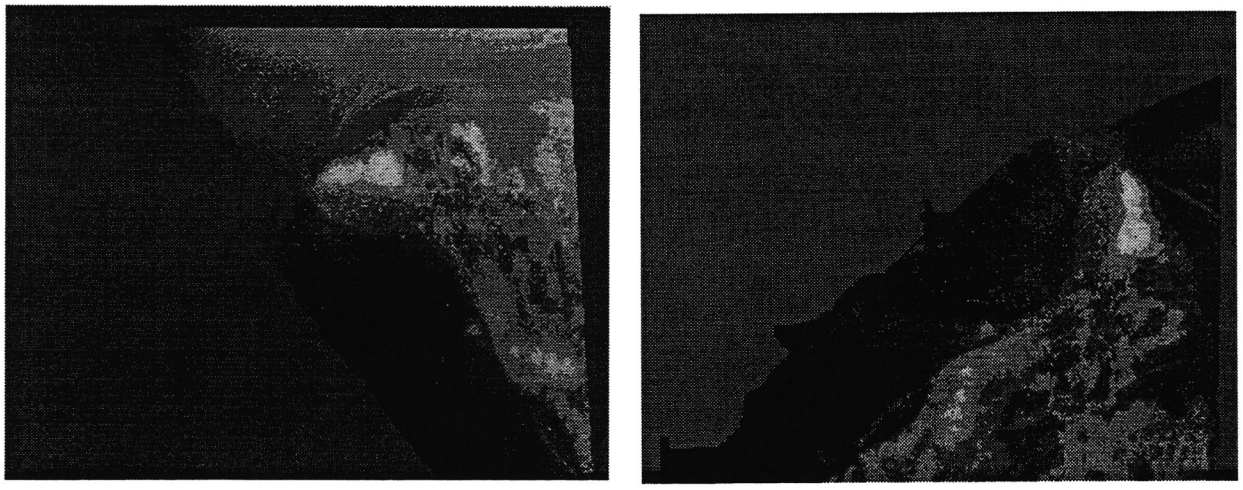

Figure 4.5 Unwrapped phase images for scenes 107 (left) and 108 (right) using the PCI algorithm.

The boundaries and areas left out from the unwrapping will lead to "jumps" in the DEM. For that reason the unwrapper of PCI-works was tried. This unwrapper uses the least square method with so called "ghostlines". These lines mark areas with low coherence. The result of that unwrapping is shown in Figure 4.5 for scenes 107 (left) and 108 (right). The sea is masked out and set to zero phase. The aeroplane flew from top left to top right. Note that the unwrapped phase is now of a better quality than previously in Figures 4.3 and 4.4.

The DLR E-SAR interferometer has in across-track mode also a baseline component in the x-direction, i.e. in the along-track direction. This results in an interferometer which is sensitive for both elevation and velocity. This can be seen in some of the phase images shown in Figures 4.3 and 4.4.

4.2.3 Phase to height conversion

The phase difference can be converted into a height difference according to the relation

$$\Delta h = \frac{\lambda H \tan\theta}{4\pi B_{\perp}} \cdot \Delta\varphi_{topo} \,, \tag{4.4}$$

with the perpendicular baseline $B_{\perp}$ given by (see also Figure 4.6)

$$B_{\perp} = B_z \sin\theta + B_y \cos\theta \,, \tag{4.5}$$

and $\Delta\varphi_{topo}$ the flat earth corrected unwrapped phase.

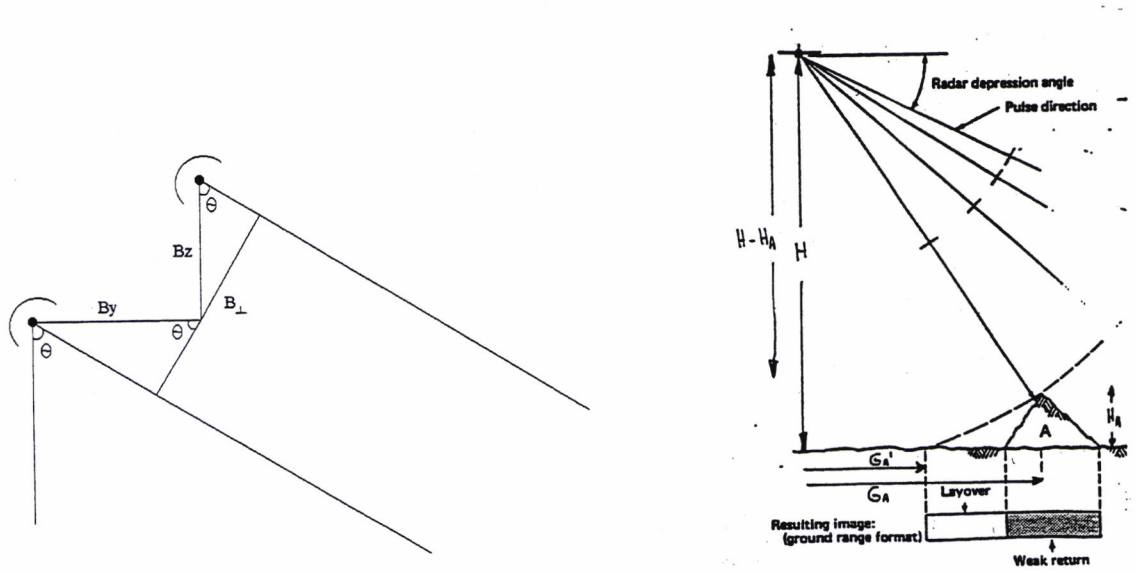

Figure 4.6 Left: baseline geometry. Right: conversion to ground range and correction for layover.

4.2.4 First trend correction

There can still be a trend in range due to an error in the flat earth correction. A linear trend is corrected for in scene 107. No trend was visible in scene 108.

4.2.5 Ground range transformation and overlay correction

The next step is to correct for overlay effects and to transform to ground range. A point in a SAR image with a height H_A will be plotted more nearby than its real position. The pixels in range direction have to be moved over a distance $G_A - G'_A$ as indicated in the right panel of Figure 4.6. This distance is given by

$$G_A = \sqrt{(G'_A)^2 + H^2 - (H - H_A)^2}\ , \tag{4.4}$$

with H the height of the SAR antenna.

For a flat earth, the slant to ground range conversion is a non-linear projection, which is carried out straightforwardly by regridding. If the terrain is not flat, however, the local terrain height enters in the projection formula. With s the slant range, g the ground range, h the local terrain height and H the aircraft altitude, the projection formula is:

$$s^2 = g^2 + (H - h)^2\ . \tag{4.5}$$

When the slant to ground range conversion has to be performed, $h(\tilde{s})$ is given, while $h(\tilde{g})$ is sought. The tilde indicates a linearly spaced grid. Two approaches are possible to solve this. The first is to compute a table of $g(\tilde{s}, h(\tilde{s}))$. This leads to a table of irregularly spaced g-values. The linearly spaced $\tilde{g}$ values can be looked up by interpolation in this table, and the corresponding h-values can then be interpolated from $h(\tilde{s})$. This approach is fast, but runs into problems when the table of g-values is not monotonic which may happen in case of lay-over. Moreover, interpolation in an irregular grid yields uncontrollable results that may spoil the accuracy.

The second approach is by starting with the desired linearly spaced grid $\tilde{g}$, and then, for each point on this grid, iteratively solving

$$s_{i+1} = \sqrt{g^2 + (H - h(s_i))^2}\ . \tag{4.6}$$

A starting value for $h(s_i)$ at $i=0$ has to be chosen. Here the starting values are zero. With this approach, the iteration may be continued until a desired accuracy is reached. In the numerical implementation provisions can be made to ensure convergence. In case of lay-over this convergence will not be to the correct value, since the problem is always undetermined.

Both methods were applied to scenes 107 and 108. The first attempts produced ground range DEMs that gave a strange impression of a sort of smoothing or striping in the range direction. It turned out that this effect was caused by noise in the DEM. An error analysis of the projection formula shows that, for given values of H and g, a change in h results in a change in s according to

$$\delta s = (H - h)/s\ \delta h \approx \delta h\ . \tag{4.7}$$

The slant range DEM has a pixel spacing of 6 m. It shows height differences of the same order (6 m) between neighbouring pixels. After transformation to ground range, DEM-values can be randomly shifted in the range direction over distances of the order of 1 pixel size. This caused the strange appearance of the ground range DEMs. The remedy for this effect is to perform the slant range to ground range projection using a smoothened DEM that does not have large height differences between neighbouring pixels. Note that this means that the

smoothened DEM is used to give the *h(s)* in the projection, but that still both the radar power image and the *unsmoothened* DEM can be slant-to-ground-range-projected at their full resolution. This leads to a third method for slant range to ground range transformation.

The effect is demonstrated in the Figure 4.7. Figure 4.7a shows the (unsmoothened) DEM in slant range projection; Figures 4.7b-d are in ground range. Figure 4.7b was obtained using a flat DEM, Figure 4.7c by using the unsmoothened DEM, and Figure 4.7d by using a smoothened DEM. The DEM was smoothened by convolution with a 2-dimensional Hanning function with a width of 8 pixels in both slant range and azimuth direction. The image in Figure 4.7c has a noisy structure which is absent in the other images, which must therefore be due to the noisy nature of the unsmoothened DEM. The effect may be aggravated by the relatively large pixel spacing, since formally the data are undersampled (see also Tables 4.1 and 4.2). Note that since the pixel spacing in the slant range is different from that in the ground range, the number of range pixels in Figure 4.7a deviates from that of Figures 4.7b-d. The DEMs shown in Figures 4.7a, 4.7b and 4.7d differ significantly, but this can best be appreciated by blinking them on a monitor, or by inspecting cross-cuts.

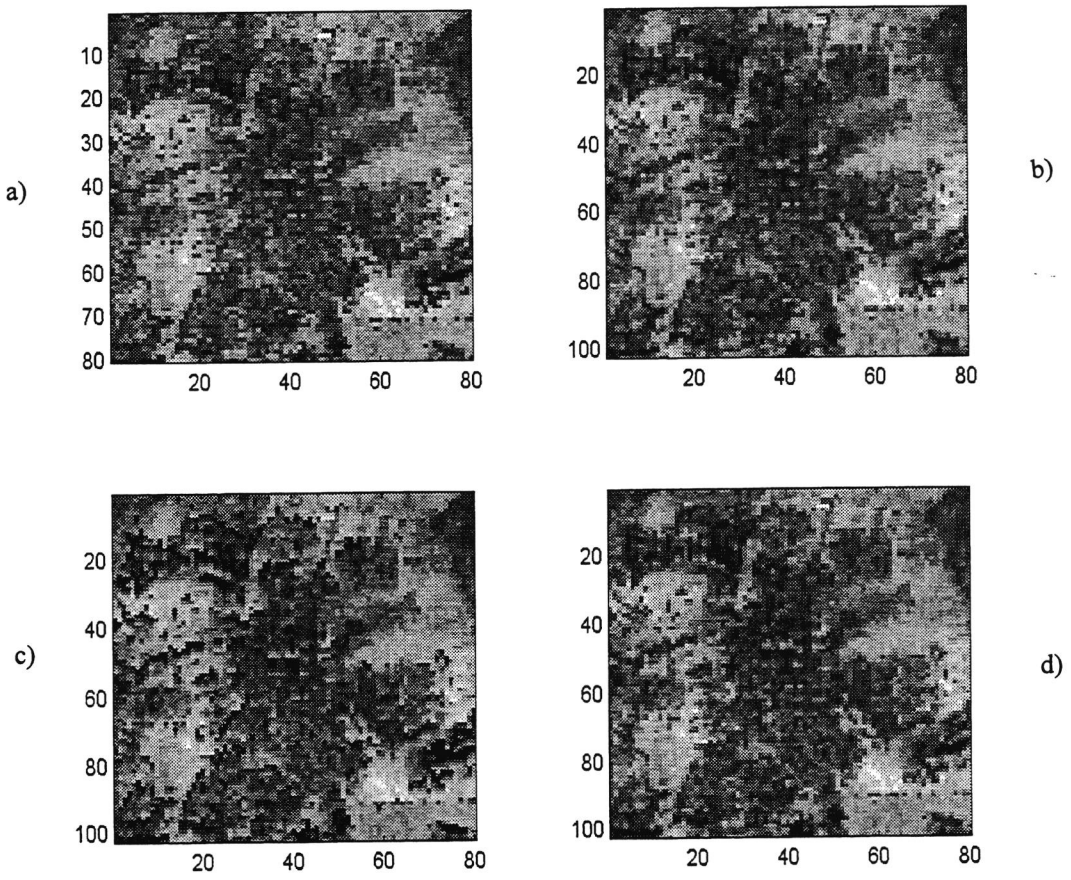

Figure 4.7 DEM of a small test area of scene 108. The range direction is downward, the azimuth direction to the right. a) Slant range DEM; b) Ground range DEM obtained using flat earth; c) Unsmoothened ground range DEM; d) Smoothened ground range DEM.

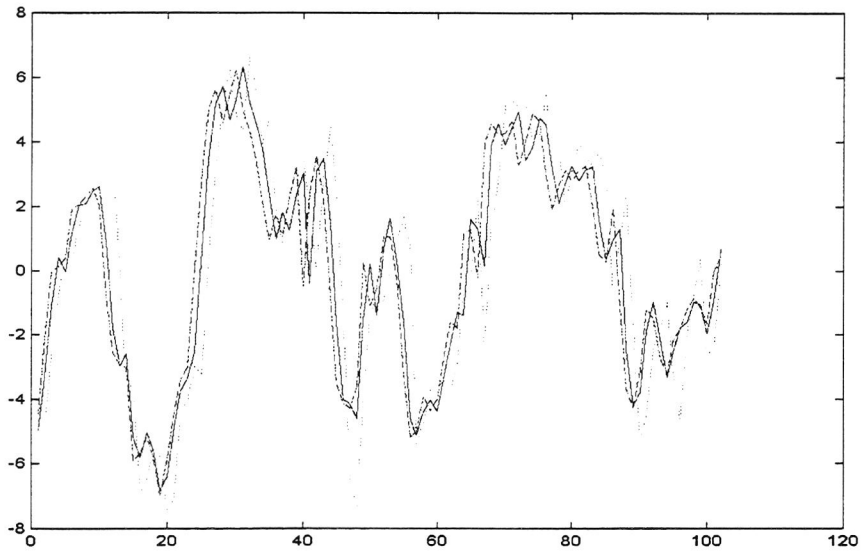

Figure 4.8 Cross-cut in range direction through the three ground range DEMs of Figure 4.7. Dashed curve: using flat DEM; dotted curve: using unsmoothened DEM; solid curve: using smoothened DEM. To compare these three cross-cuts in one graph, the profiles were averaged over a few neighbouring cross-cuts and the average heights were subtracted.

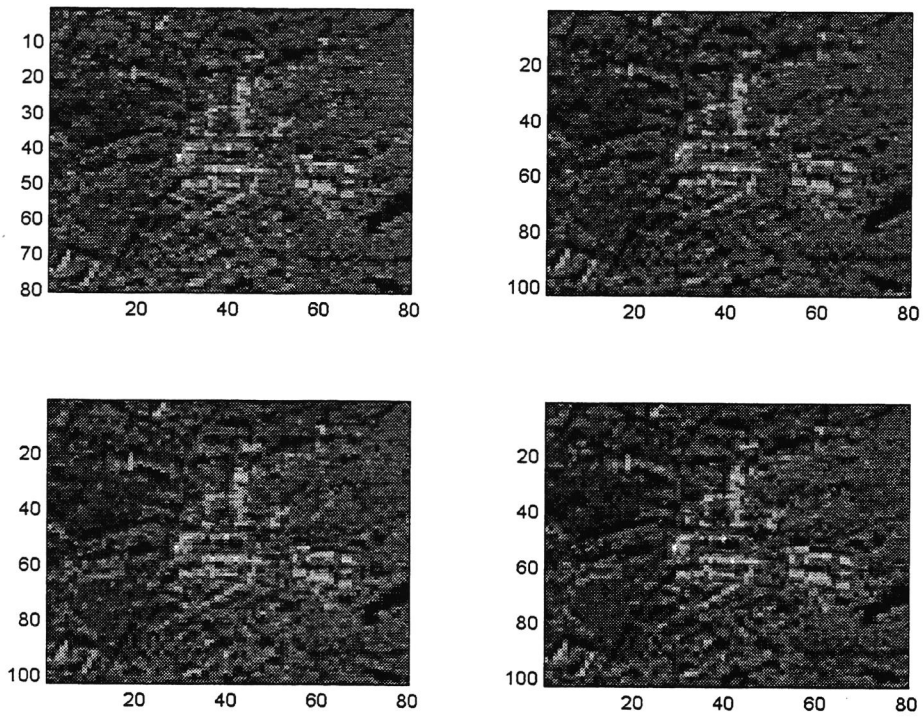

Figure 4.9 Radar power image (in dB) of the same area and in the same projections as Figure 4.7, showing built-up structures on Terschelling.

Scene 107				
Altitude (m)	3160.98			
Ground speed (m/s)	81.7812			
PRF after pre-sum (/s)	250			
107 SLC	Azimuth	Slant Range	Ground Range	Incidence Angle
# Pixels	13092	1596	-	-
Pixel spacing (m)	0.32712	1.49896	-	-
Image size (m)	4283	2392	3480	32.4 °
Resolution (m)	0.67	1.5	3.5 - 1.8 (near to far)	-
Near (m)	-	3490.03	1479.36	25.080 °
Far (m)	-	5880.88	4959.13	57.486 °
107 Result	Azimuth	Slant Range	Ground Range	
# Pixels	654	399	530	
Pixel spacing (m)	6.5424	5.99584	6.55477	
Image size (m)	4279	2392	3467	
Resolution (m)	6.6	6.2	15 - 7.3 (near to far)	
Near (m)	-	3490.03	1490.00	
Far (m)	-	5880.88	4957.47	
Smoothened DEM resolution(m)	53	48	110 - 57 (near to far)	

Table 4.1 Parameters of scene 107.

Scene 108				
Altitude (m)	3158.84			
Ground speed (m/s)	81.1903			
PRF after pre-sum (/s)	250			
108 SLC	Azimuth	Slant Range	Ground Range	Incidence Angle
# Pixels	13459	1597	-	-
Pixel spacing (m)	0.32476	1.49896	-	-
Image size (m)	4371	2394	3480	32.4 °
Resolution (m)	0.67	1.5	3.5 - 1.8 (near to far)	-
Near (m)	-	3488.53	1480.40	25.110 °
Far (m)	-	5880.88	4960.49	57.511 °
108 Result	Azimuth	Slant Range	Ground Range	
# Pixels	672	399	534	
Pixel spacing (m)	6.4952	5.99584	6.50739	
Image size (m)	4365	2392	3468	
Resolution (m)	6.5	6.2	15 - 7.3 (near to far)	
Near (m)	-	3488.53	1490.00	
Far (m)	-	5880.88	4958.44	
Smoothened DEM resolution(m)	53	48	110 - 57 (near to far)	

Table 4.2 Parameters of scene 108.

Figure 4.8 compares cross-cuts, in range direction, through the ground range DEMs. The result using the unsmoothened DEM is much noisier than the other two. The results using the zero DEM and the smoothened DEM differ at the higher altitudes and overlap at the lower, as expected, because at the lower (near zero) altitudes the smoothened DEM locally equals the zero DEM. Figure 4.9 compares the results of the different projections on the radar power image of the same test area. The effect of using the full resolution noisy DEM seems

to be less severe on the power image. Again, projection differences are significant, but can best be seen by blinking on a monitor.

In view of the results above, the final ground range projection was performed using a DEM smoothened by a 2-dimensional Hanning function with a width of 8 pixels in both slant range and azimuth direction. Tables 4.1 and 4.2 list the parameters of scenes 107 and 108, respectively. The first part of each table gives the relevant flight parameters. The second part gives the parameters of the SLC image pair as delivered by DLR (which is a slant range image). The listed SLC resolution was not measured but is the nominal resolution as specified by DLR. The third part lists the parameters of the derived power image and DEM in slant range and ground range. The basis of these is the SLC image pair after spatial averaging over 4 × 20 pixels (slant range × azimuth). Note that the result of this averaging is formally undersampled (fewer than 2 samples per resolution element). The ground range data have (very nearly) square pixels, so that these data are geometrically correct. Note that in ground range the range resolution is a function of range. The line "smoothened DEM" refers to the slant range smoothened DEM used for the slant-to-ground range projection. As the resolution for this DEM also varies with ground range, this is not a suitable product to use in case a ground range smoothened DEM is needed. In that case, it would be better to subject the full-resolution ground range DEM to smoothing.

The resolution of the slant range image, R_{SR} is calculated from

$$R_{SR} = \sqrt{R_{SLC}^2 + N_{avg}^2 d_{SLC}^2} \,, \tag{4.8}$$

with R_{SLC} the resolution in the SLC image, N_{avg} the number of pixels in the SLC image averaged over, and d_{SLC} the pixel distance in the SLC image. In fact, (4.8) is a convolution of the original resolution and the averaged pixel distance.

In order to control the quality of the resulting data, cross cuts were made through the power images of the corner reflector on the eastern edge of scenes 107 and 108. The results are shown in Figures 4.10 and 4.11. In the azimuth direction (right half of the figures), the ground range cross-cuts are the same as the slant range ones. In the range direction (left halves), the ground range cross cuts are broader than the slant range ones.

However, this is in units of pixels. For scene 107, the slant range width of the corner reflector is 1.6 pixels, equal to 6.5 m slant range. The corner is located at an incidence angle 37.7°, so the ground range width is 6.5/sin(37.7°) = 10.7 m. The measured ground range width is 2.7 pixels, or 12.1 m. For scene 108, the slant range width is 2.9 pixels, equalling 11.8 m in slant range, corresponding to 12/sin (52.4°) = 14.9 m in ground range. The measured ground range width is 3.2 pixels, equalling 14.1 m. Therefore, the data have not been significantly smoothened or degraded by the slant to ground range projection. The extracted corner widths are listed in Table 4.3. There is a significant difference in the measured width in range direction between scenes 107 and 108, which cannot be explained. The values of the ground range in the table above are averages of the calculated ground range and the measured one. The slant range is then calculated back from that average.

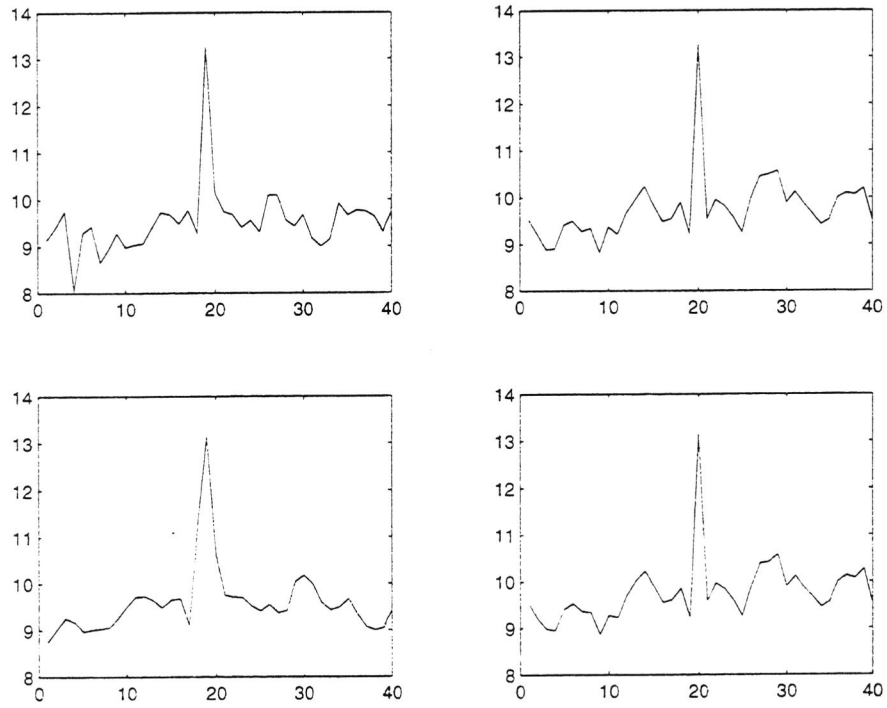

Figure 4.10 Scene 107. Cross-cuts through the corner reflector on the East edge of the scene. Top: slant range image; bottom: ground range image. Left: range; right: azimuth.

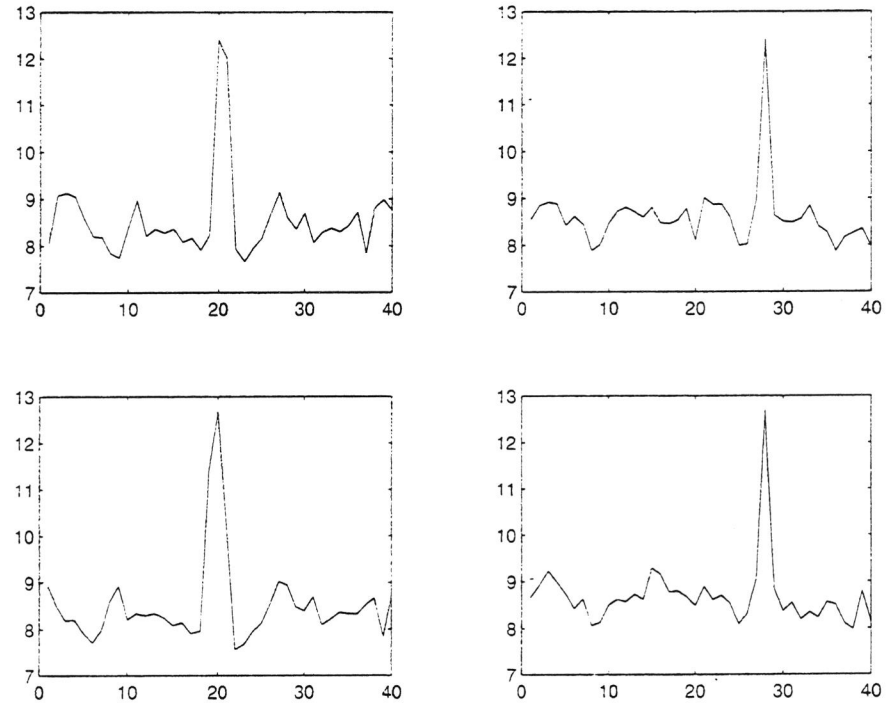

Figure 4.11 Scene 108. Cross-cuts through the corner reflector on the east edge of the scene. Top: slant range image; bottom: ground range image. Left: range; right: azimuth.

Scene	Corner at Incidence angle	Azimuth (m)	Slant Range (m)	Ground Range (m)
107	37.7 °	6.0	7.0	11.4
108	52.4 °	7.5	11.5	14.5

Table 4.3 Measured widths (FWHM) of the corner reflector on the east edge of the scene. Accuracy is ± 1 m.

4.3 DEM Results

The DEMs obtained from scenes 107 and 108 are shown and discussed in this section. As stated before, the reason for choosing scenes 107 and 108 is because these XTI images have the best phase images. Figure 4.12 shows a 3-d impression, Figure 4.13 a height contour map, and Figure 4.14 a grayscale map of the DEMs.

The DEMs were calibrated by setting the height of the water in the harbour area to zero. A mask is used to set the water areas to zero. This is done because of the ATI component in the image which causes a phase difference in the water due to currents.

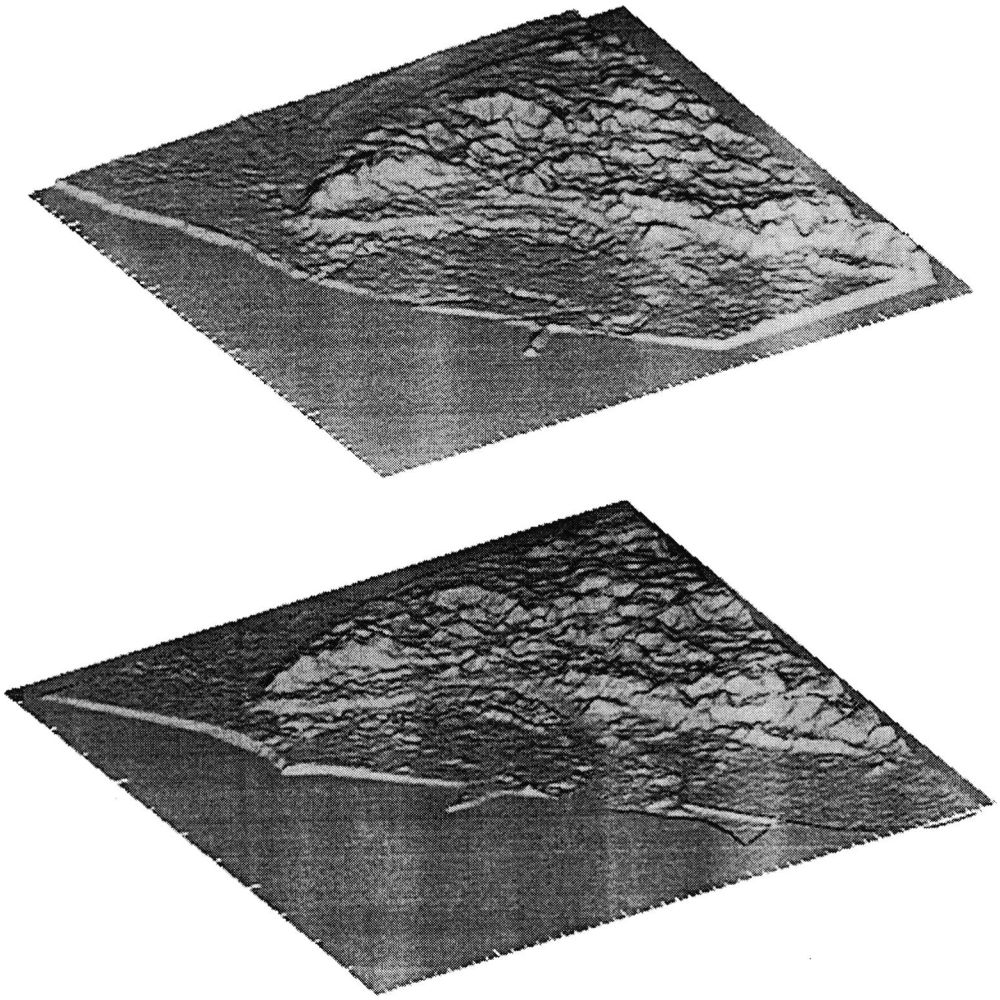

Figure 4.12 Three-dimensional views of the DEMs from scene 107 (top) and 108 (bottom).

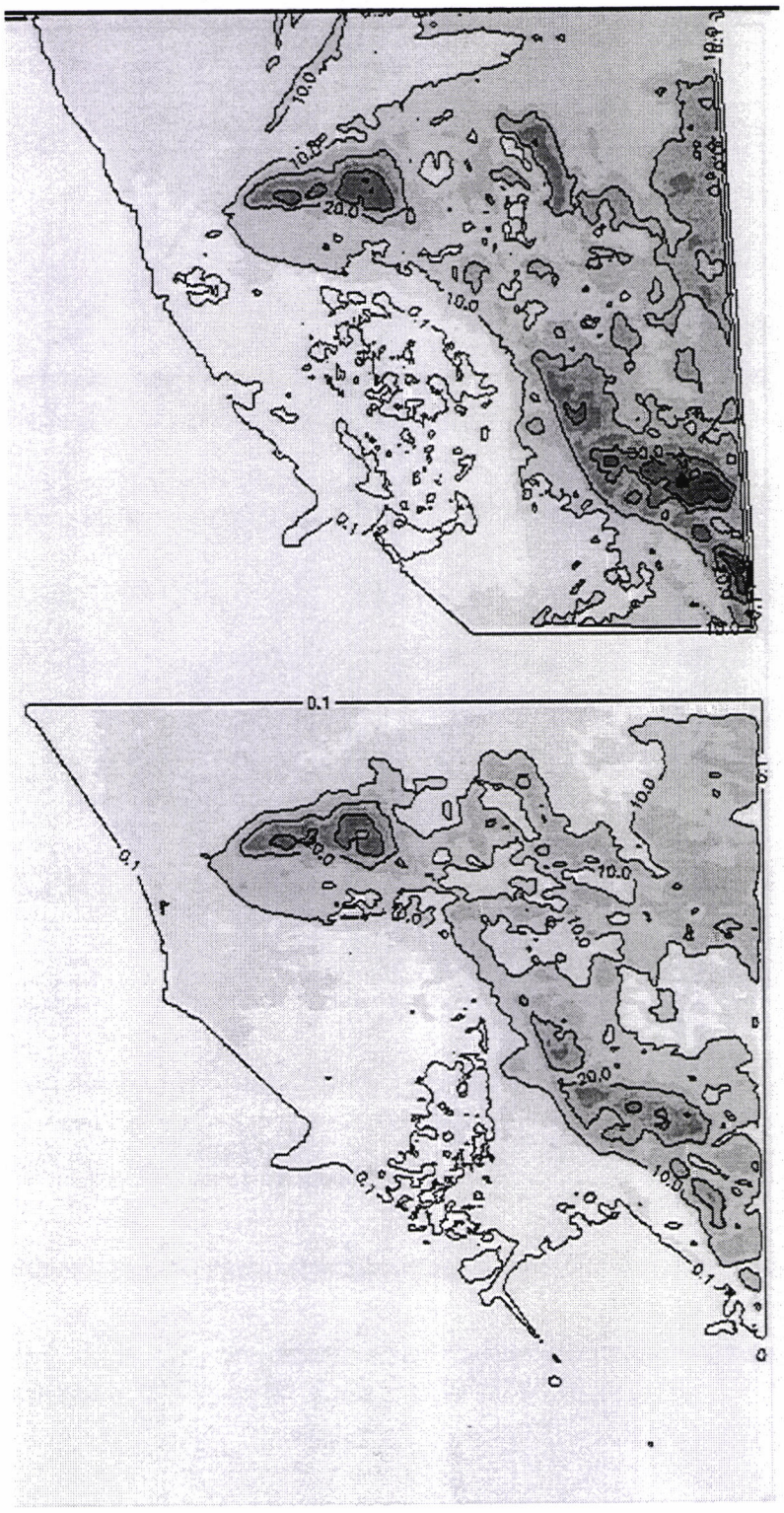

Figure 4.13 Contour plots of the DEMs from scene 107 (top) and 108 (bottom). The grey tones represent a 5 m interval from -5 m to +40 m.

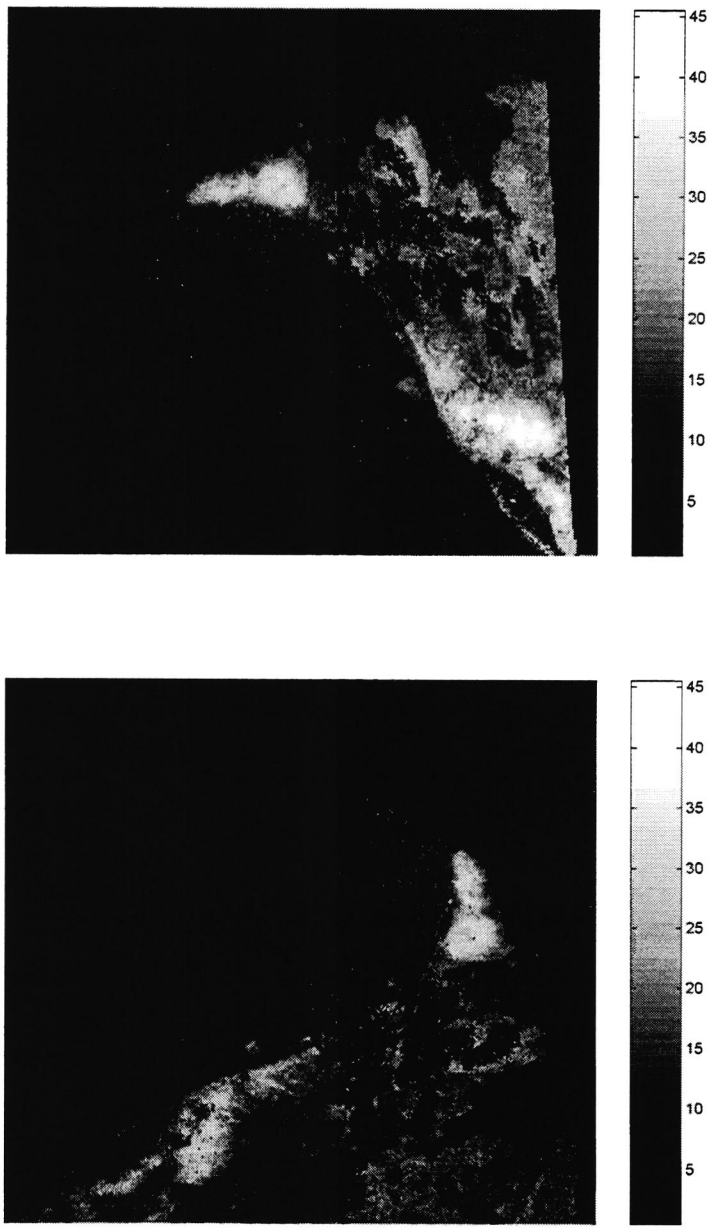

Figure 4.14 Map of the DEM from scene107 (top) and 108 (bottom). The scale at the right hand side is in m.

The image of scene 108 still contains a trend in azimuth (bottom to top in Figures 4.12-4.14). This is due to bad processing of the flight data. The 107 DEM is projected on the 108 DEM so they have the same frame co-ordinates. A smoothing factor of 5 × 5 pixels is used to improve the image.

4.4 DEM validation

The DEMs generated from scenes 107 and 108 cover part of Terschelling. In Figure 4.15 the area of interest is shown together with the flight direction of scenes 107 and 108. For the evaluation some areas of interest are chosen. These are within the white frames in Figure 4.15.

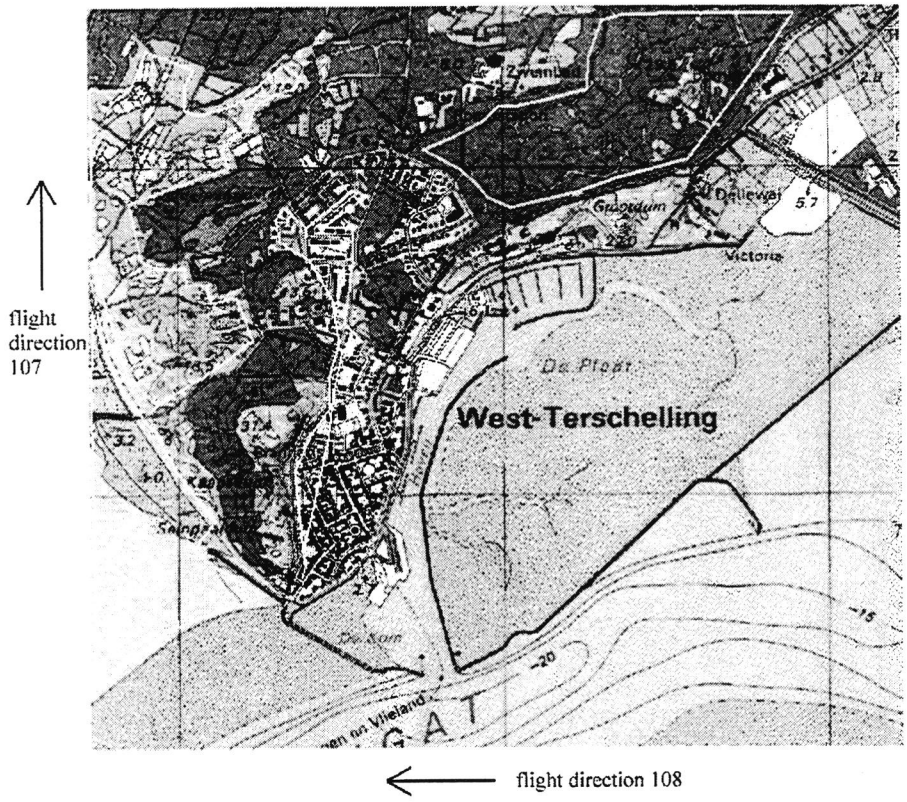

Figure 4.15 Area of interest: the western part of Terschelling. The flight directions of both perpendicular INSAR pairs are shown. The four areas of interest are marked in white.

A number of processing steps is needed to compare the INSAR DEMs with the laser DEM. These steps are schematised in Figure 4.16.

4.4.1 Geocoding

The DEMs are geocoded by selecting ground control points on the intensity images and on the digital 1:10,000 topographic map. After geocoding the position of each pixel is known in Dutch National Reference (RD) co-ordinates. With 14 points the root mean squared (RMS) error of transformation was 1.5 pixel for DEM107 and 1.1 pixel for DEM108. The laser DEM is already given in RD co-ordinates. The point density of the laser DEM is 1 point per 4×4 m^2 and is therefore higher than the point density of the INSAR DEMs that have a resolution of about 7×10 m^2 (azimuth $\times$ range). After transformation to RD the INSAR data are interpolated to grids of 5×5 m^2. To perform the validation properly, the amount of interpolation of both datasets should be minimised. Therefore the original laser data points are used for comparison instead of a grid of interpolated laser data.

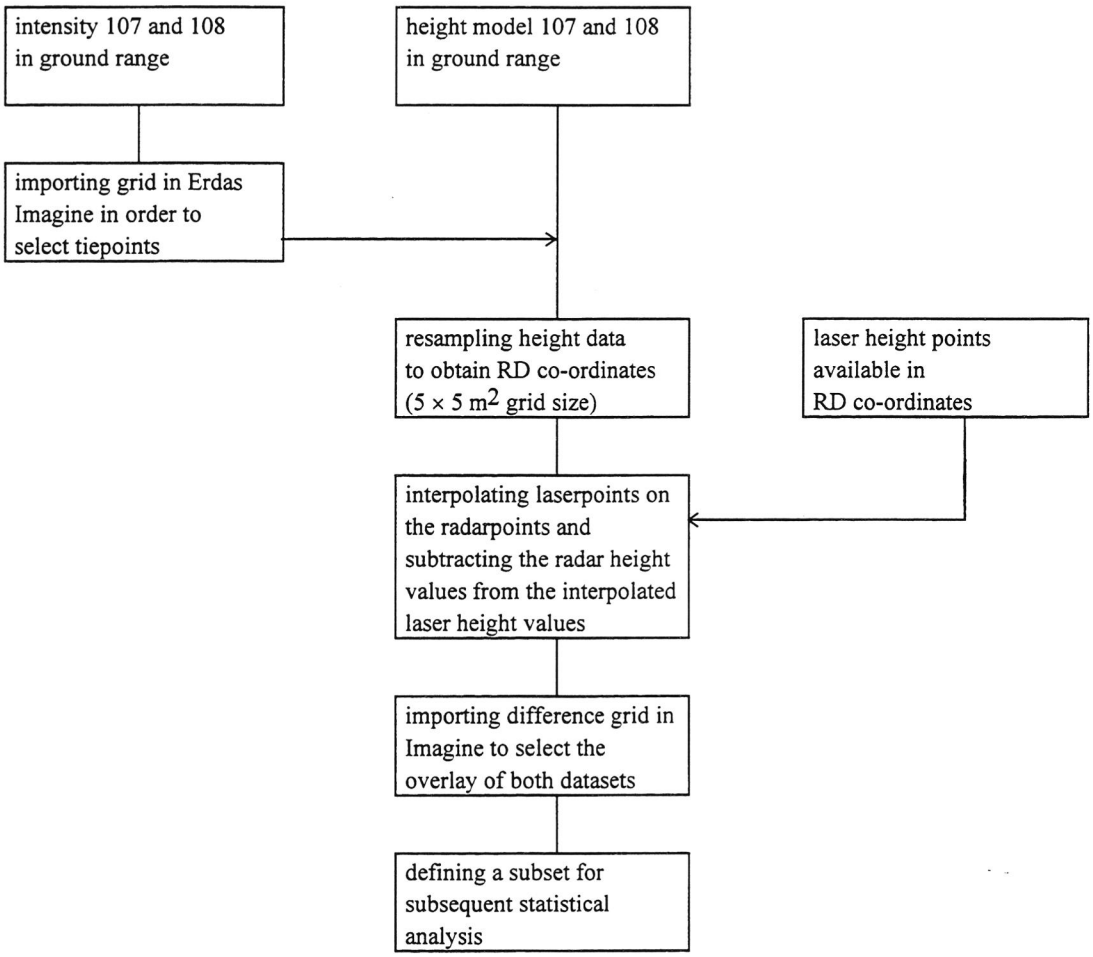

Figure 4.16 Processing steps for comparing the INSAR height models with laser height models.

For each INSAR point the height is subtracted from the averaged height of the surrounding laserpoints within a footprint of 10 m. To make the results of 107 and 108 comparable a subset is defined that covers the area that 107 and 108 have in common. In this subset statistics are applied.

From the INSAR datasets 107 and 108 three different methods of slant to ground range conversion are applied (see also section 4.2.5). This leads to the following ground range DEMs: *107R and 108R* (ground range as a function of the slant range and height in slant range), *107H and 108H* (iterative solution of heights for each ground range point) and *107S and 108S* (using a smoothed DEM for the height values in slant range to compute

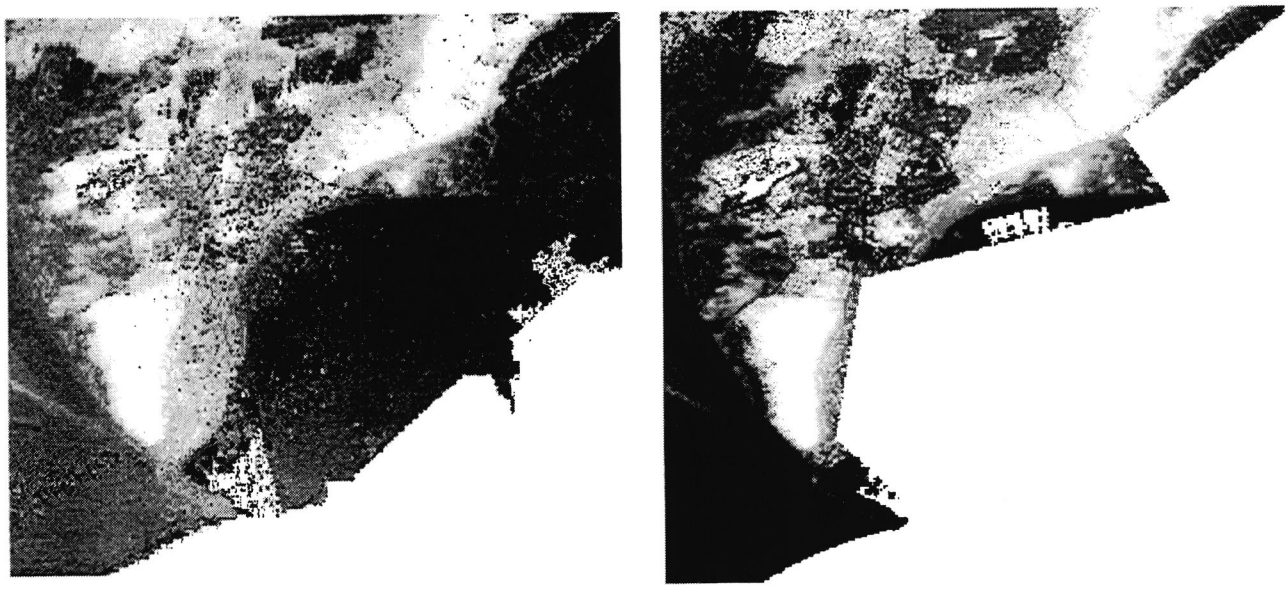

Figure 4.17 Part of the XTI DEM 108H (left) and the corresponding part of the laser DEM (right).

the ground range). Figure 4.17 shows the XTI DEM 108H as example of the processed INSAR DEMs. The white areas indicate higher situated areas like forests. This should be compared to Figure 4.15.

The laser DEM from Terschelling is not filtered for vegetation. Part of this reference DEM is shown also in Figure 4.17. The angularity at the right shows the area where the laser has not flown or the pulses have not been reflected back to the aeroplane due to the properties of the water surface.

Corner reflectors on Terschelling are used to check the planimetric position as they appear as bright spots in the amplitude images. In the DEMs the corners are used to check the heights. With this information a possible distortion in height or planimetry can be seen.

4.4.2 First comparison

Table 4.4 gives the mean and standard deviations of the differences of the various INSAR DEMs with the laser DEM. The difference between XTI DEMs 108S and 107S is also given as these DEMs give the best standard deviations when compared to the laser DEM.

Difference DEM	Mean (m)	Standard deviation (m)
Laser-107R	-7.07	3.94
Laser-107H	-7.06	4.02
Laser-107S	-7.09	3.64
Laser-108R	-2.53	4.09
Laser-108H	-2.53	4.21
Laser-108S	-2.55	3.51
108S-107S	-3.09	4.15

Table 4.4 Statistics of the difference DEMs.

The large mean values between the INSAR DEMs and the laser can be caused by a trend in the INSAR DEMs. The absolute heights of the INSAR DEMs are based on one point in the harbour which is set at zero height. When a trend is present in the INSAR DEMs the difference between the INSAR DEM and laser DEM gets larger when the point is further away from the harbour, causing a large mean difference value. The large standard deviation values can be caused by the presence of vegetation. In order to eliminate this effect areas of interest are defined with homogeneous vegetation types, see Figure 4.15.

The mean difference of both XTI DEMs (3.09 m) is not equal to the difference between both XTI DEMs with the laser DEM (7.09 and 2.55 m) because the nodata values of laser are not a limiting factor, so a larger area is enclosed. The large difference between both XTI DEMs can be caused by phase unwrapping problems. This occurs at very steep hills and by artefacts in the phase data caused by low SNR or aeroplane movements.

Four corner reflectors were installed, spread over the area of interest. Their planimetric positions are checked in the amplitude images. In these images groups of light pixels are seen at the positions of the corners. The heights of the corners are checked with the corresponding heights in the INSAR DEMs. Table 4.5 shows the heights for each corner. When comparing the heights for DEM 107 and DEM 108 with the corners it appears that 107 lies too high on the whole and especially in the north and in the west 107 lies much too high. DEM 108 lies in the north and in the east too low and in the west and south too high compared with the corners. These deviations are mainly caused by a trend that is present in the INSAR DEMs.

Corner no	position	height corner (m)	height 107R (m)	height 107H (m)	height 107S (m)	height 108R (m)	height 108H (m)	height 108S (m)
1	south	2.14	4.47	4.89	5.48	4.05	8.82	5.97
2	north	7.40	15.07	16.30	15.84	5.49	5.99	5.28
3	west	3.43	12.75	12.72	12.48	6.18	6.14	6.13
4	east	2.08	5.67	7.44	7.99	0.64	0.43	1.12

Table 4.5 Results of comparing the heights of the corners with the corresponding heights of the INSAR DEMs.

Figure 4.18 shows the difference of the laser DEM with each sample of DEM 107 and 108. It appears that DEM 107 lies higher than DEM 108. This can also be inferred from the values of the mean differences in Table 4.4.

4.4.3 Second trend correction

In figure 4.18 a trend is clearly visible. Comparing to the flight directions in Figure 4.15, the largest part of the trend appears in the azimuth direction. This trend can be caused by bad processing of the flight data. In order to get representative quality measurements this trend is calculated and subtracted from the difference DEMs.

The estimated trend is shown in Table 4.6. The trend is computed by removing the mean offset and minimising the standard deviation over the whole difference DEM while subtracting a plane turned over a certain angle.

The improvements of the standard deviation values are not significant. This means that the trend is not the dominant factor in the standard deviation. However, when the trends are corrected for in the difference between both XTI DEMs the standard deviation improved significantly.

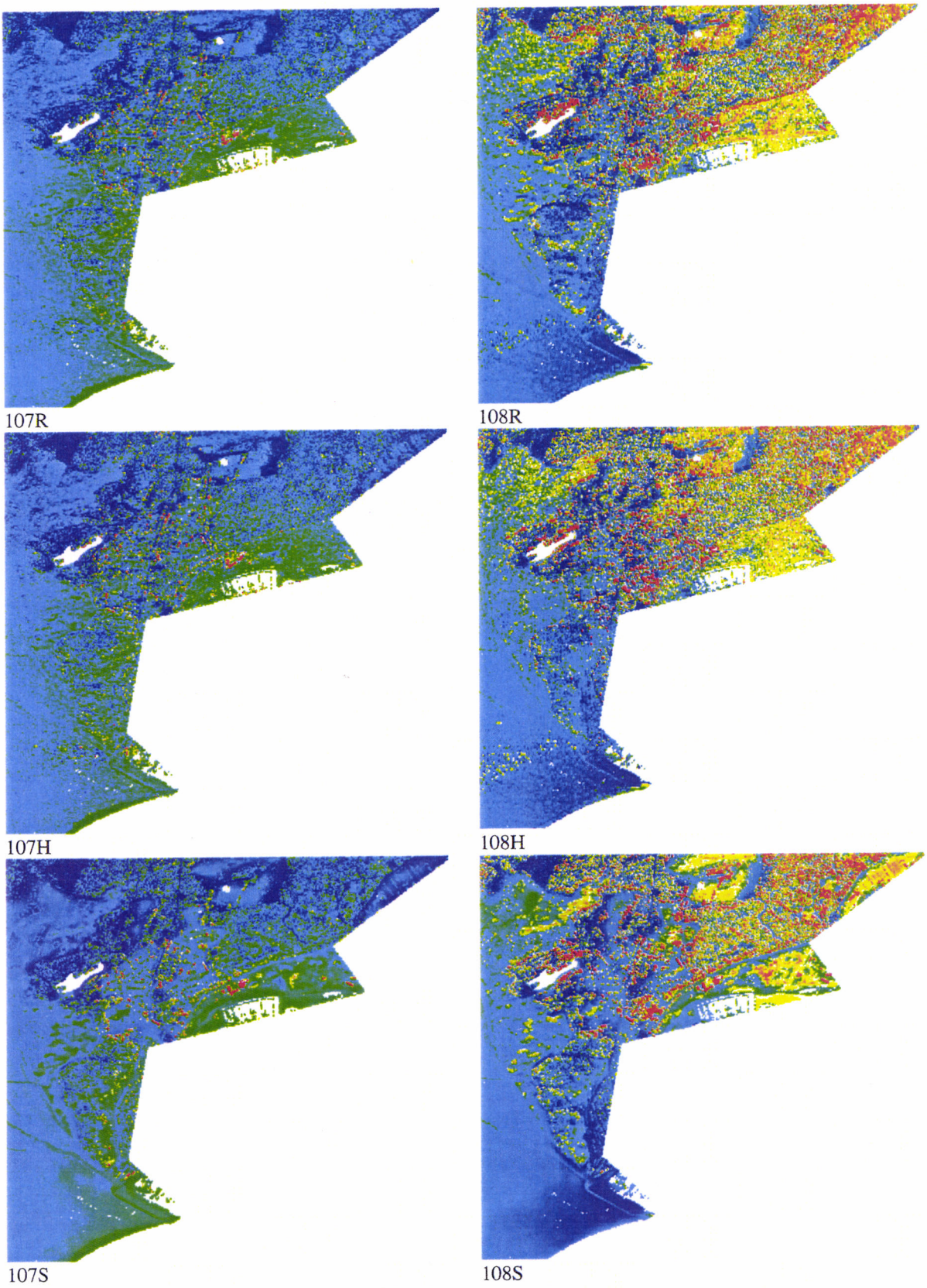

Figure 4.18 Differences of laser DEM with INSAR pairs 107 and 108. Negative differences (INSAR > laser) are given in blue (large difference) to green (small difference). Zero values and nodata is given in white. The positive differences (INSAR < laser) are given in yellow (small difference) to red (large difference).

	estimated tilt x-axis (tan α)	estimated tilt y-axis (tan α)	standard deviation before correction (m)	standard deviation after correction (m)
Laser-107R	0.003	0.002	3.94	3.52
Laser-107H	0.003	0.002	4.02	3.62
Laser-107S	0.003	0.002	3.64	3.17
Laser-108R	-0.0005	-0.0025	4.09	3.67
Laser-108H	-0.0005	-0.0025	4.21	3.80
Laser-108S	-0.0005	-0.0025	3.51	3.05
108S-107S	0.0055	-0.001	4.15	2.20

Table 4.6 Results of estimating the trend in the difference DEMs.

4.4.4 Final comparison

Figure 4.19 shows the difference DEMs after subtracting the estimated trend. Here the red and blue coloured areas indicate differences of more than 5 m and the grey values indicate height differences of less than 5 m. The largest differences occur at highly vegetated areas, as can be seen from comparison with Figure 4.15. Figure 4.19 therefore shows the correlation between vegetation and the differences between laser DEM and INSAR DEMs.

The standard deviations were determined for different sub-area's in order to clarify the influence of vegetation. The results are listed in Table 4.7. The standard deviations of the homogeneous areas are better than the standard deviation of the whole XTI DEM (3.17 and 3.05 m, see table 4.6). Because the offset for the whole difference DEM is corrected for, the means for the different sub-areas are not equal to zero after correction.

Sub-area	Laser - 107 S				Laser - 108S			
	Before correction		After correction		Before correction		After correction	
	Mean	Std. Dev.	Mean	Std. Dev.	Mean	Std. Dev	Mean	Std. Dev.
beach	-6.41	0.52	-0.30	0.93	-4.10	0.75	0.52	0.83
city	-5.65	2.52	1.22	2.47	-3.90	2.67	-0.97	2.60
forest	-7.41	3.33	-0.33	3.29	0.27	3.12	0.59	3.05
heath	-7.94	1.91	0.89	1.38	-2.16	1.52	1.84	1.41

Table 4.7 Mean and standard deviation (Std. Dev.) values before and after the second trend correction.

The improvements of the standard deviations for each sub-area are not significant after removing the trend. The beach area has a standard deviation of about 0.9 m and the heath area has a standard deviation of about 1.4 m, which are quite well. The forest area and the city are less regular and have standard deviation values around the 3 m. Figure 4.20 shows the histograms of the differences laser-107S and laser-108S before and after correction.

The standard deviation values of the differences between both XTI DEMs are as follows for the sub-areas after correction: 1 m for the beach area and heath area, 1.3 m for the forest area and 1.1 m for the city. The values for forest and city are better than the corresponding values of the differences with laser. This can be caused by a different viewing geometry of laser and radar systems and by the time difference between the laser and radar. The laser data is available from 1996 whereas the radar data is available from 1997.

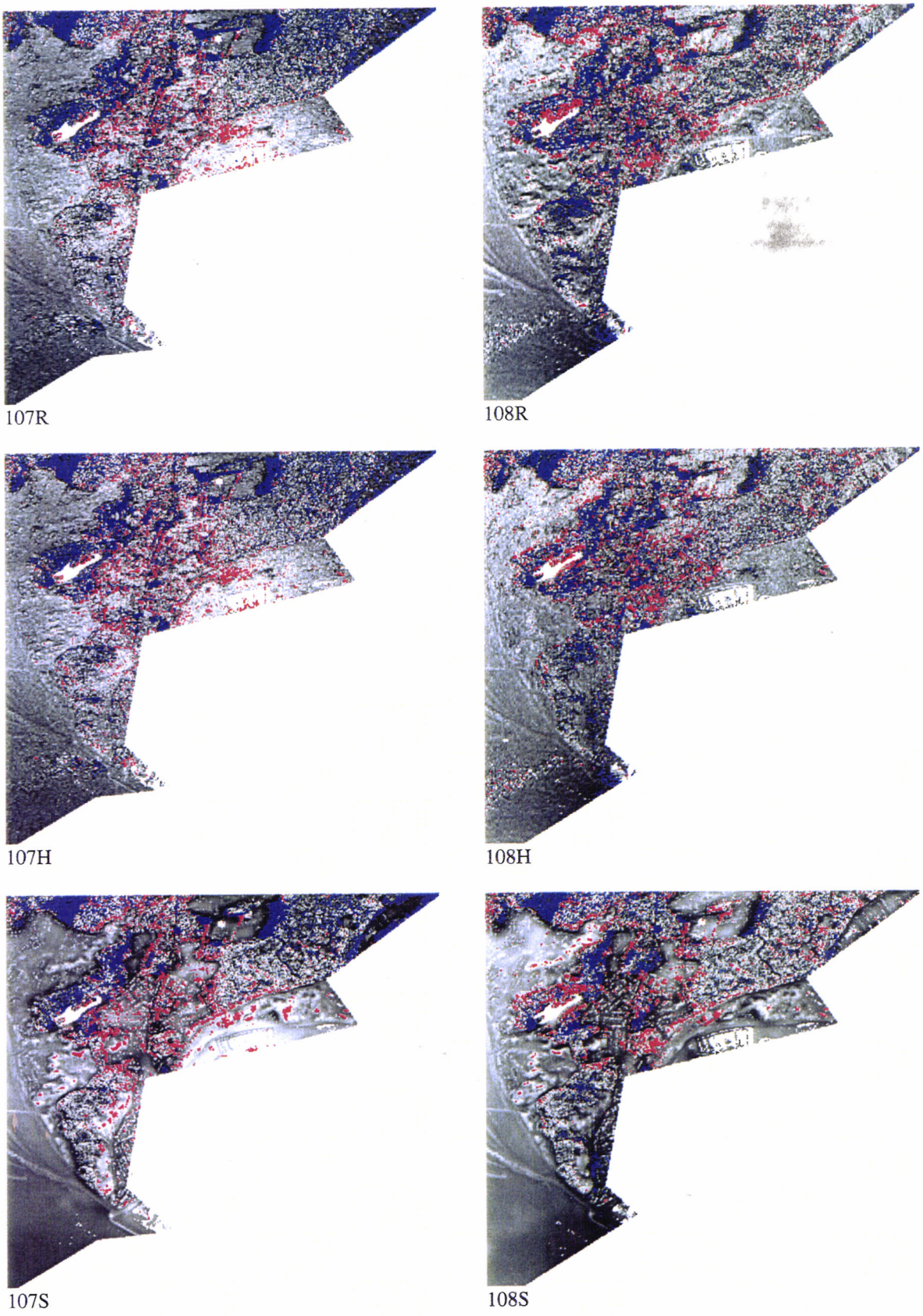

Figure 4.19 Final differences of laser DEM with INSAR pairs 107 and 108. Negative differences (INSAR > laser) of more than 5 m are given in blue. The positive differences (INSAR < laser) of more than 5 m are given in red. The differences in between are given in grey values (from black at -5 m to white at + 5 m).

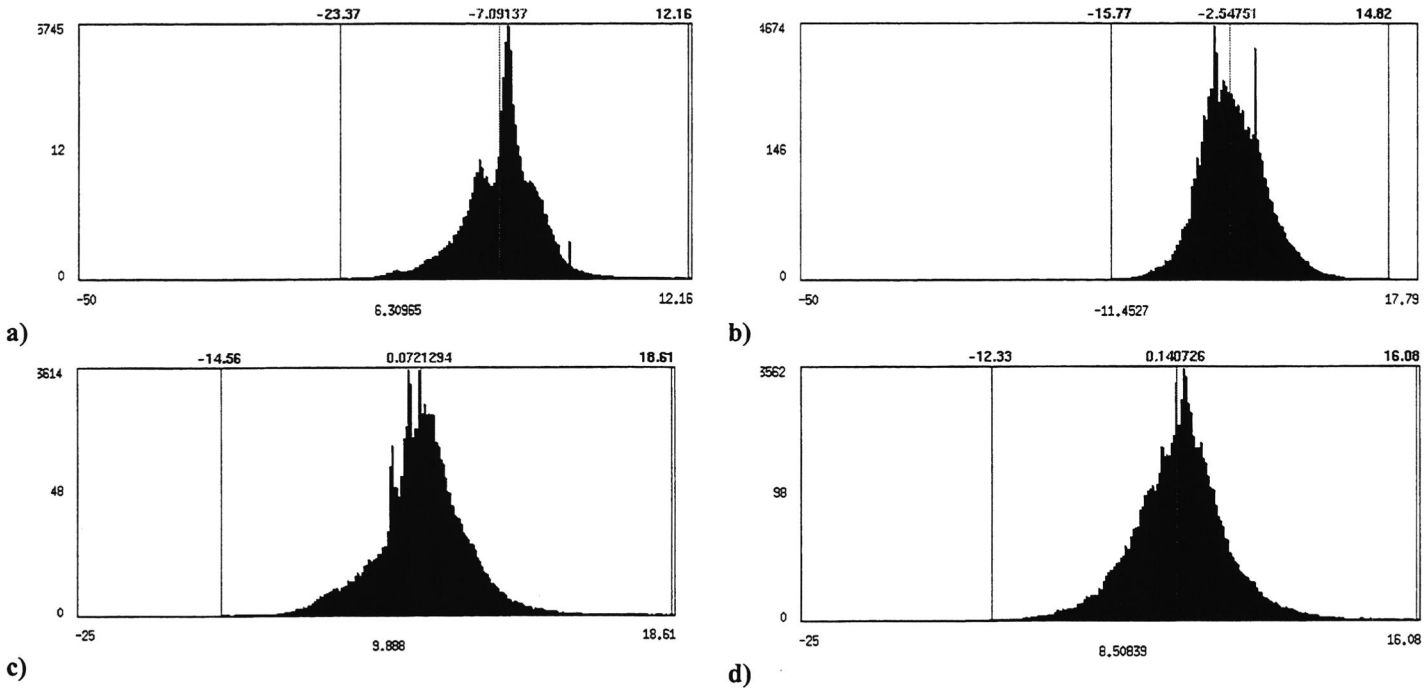

Figure 4.20 Histograms of the differences between laser and INSAR DEMs 107S and 108S: a) laser-107S before correction, b) laser-108S before correction, c) laser-107S after correction , d) laser-108S after correction.

These standard deviations can be compared with the theoretical value of the standard deviation in height due to phase noise (see also section 7.2). At the 6.5 × 6.5 m^2 slant range resolution used here, and assuming 10 dB signal-to-noise ratio (SNR) in the SLC product, the expected standard deviation in height is 0.3 m. This value is much lower than the measured one. If the measured deviations are to be due to thermal phase noise, they would require a SNR between -10 dB and -20 dB. However, such SNR values are unrealistically low. This supports the conclusion that the height errors in the interferometric DEM are not dominated by random phase noise, but by other effects such as imperfect motion and attitude compensation as well as terrain (vegetation) influences.

4.5 Concluding remarks

The following conclusions are drawn concerning the flat earth correction and phase unwrapping:

- The interferograms made from the XTI SLC images are of good quality concerning the power images. Some of the phase images, however, suffer from quite troublesome artefacts resulting in wrong DEMs.
- The phase unwrapping algorithm works reasonable and can be optimised in some cases by adjusting the software.
- Some images show distortions in the range direction. These are probably caused by insufficient correction for the aircraft movements during processing.
- Most of the data of the land is suitable to make a DEM for evaluation, especially the Terschelling data.

From the results of evaluation of the INSAR XTI data of two perpendicular pairs from Terschelling the following conclusions are drawn:

- At 8 m ground resolution, the standard deviation of the differences between two perpendicular XTI DEMs are found to be in the order of 2 m after tilt correction. For homogeneous areas the standard deviation values are all round the 1 m.
- At 8 m ground resolution, the standard deviation of the differences between the XTI-derived and the laser altimeter-derived DEMs are found to be in the order of 3.1 m after tilt correction. For homogeneous areas the standard deviation values are about 0.9 m for the beach area, about 1.4 m for heath areas and around the 3 m for forests and cities.
- For Dutch applications the accuracy is limited, even for areas with little or no vegetation.
- There is a positive correlation between vegetation and large height differences between the laser DEM and the INSAR DEMs.
- This study stresses upon that accurate DGPS data is needed for accurate INSAR applications.
- An ATI baseline component in the XTI sensor makes it impossible to derive DEMs in intertidal regions with (much) flowing water. On the other hand, in such situations the *simultaneous* operation of XTI and ATI seems to be needed to uniquely discriminate between current effects and water slope effects.
- Height errors in the DEMs are found to be larger than expected from receiver phase noise errors, supporting the conclusion that errors in the DEMs are dominated by aircraft motion and attitude errors and vegetation effects.

Chapter 5 ATI ANALYSIS

5.1 Introduction

This chapter describes how the ATI data gathered during the E-SAR experiment were processed to a map of the surface current velocity. The surface flow is compared with a model hindcast. The consistency of the data set is investigated by calculating the modulations in the amplitude image and comparing these to the recorded images.

The processing to a current map involves the following steps:

- Phase calibration and unwrapping
- Velocity calculation
- Corrections
- Coregistration

These steps will be described in section 5.2. The resulting flow map is presented and discussed in section 5.3. In section 5.4 the map is compared to a model hindcast. In section 5.5 the consistency of the data set is investigated. This chapter ends with some conclusions in section 5.6.

From the ATI data collected during the experiment, only the perpendicular scene pair 103/104 over Ameland will be fully analysed. The other data sets are too much contaminated by phase errors due to imperfect motion compensation.

5.2 Flow map generation

5.2.1 Phase calibration and unwrapping

The phase images for scenes 103 and 104 were already shown in chapter 3. To ensure that the phases in the area of the currents contain no phase jump and that the land has phase zero (velocity zero), the phase is transformed. Figure 5.1 shows a histogram of the phases of image 103. The phase runs from $-\pi$ to π radians, and the land has a phase that is a little bit less than zero. To estimate the necessary phase shift, the phase of the land is measured in different places, as listed in Table 5.1. The phase image is shifted with +0.5 radians (see Table 5.1) to set the land on phase zero.

The same procedure is followed for image 104. Here a larger phase shift of +1.76 radians is needed to set the phase of the land equal to zero. Furthermore, a phase jump occurs above the water. Therefore 2π is subtracted from all shifted phases greater than zero in order to remove this jump.

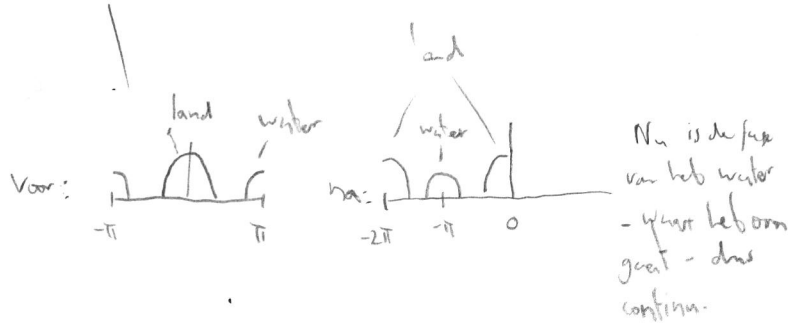

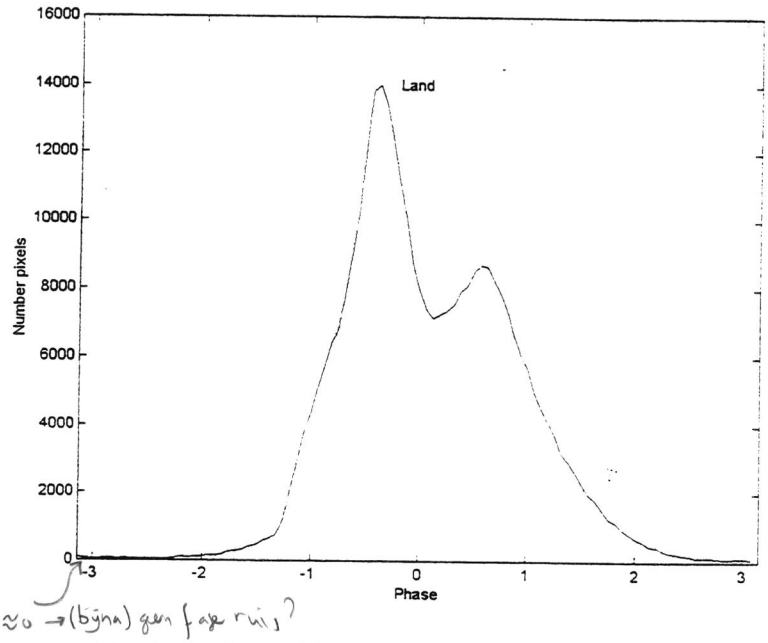

Figure 5.1 Histogram of the phases of scene 103.

X interval (range)	Y interval (azimuth)	Mean phase	Standard deviation
300:398	0:100	-0.3209	0.3168
300:398	100:200	-0.2826	0.1544
300:398	200:300	-0.4283	0.1881
300:398	300:400	-0.4549	0.1762
300:398	400:500	-0.5751	0.1548
340:398	500:600	-0.7230	0.1211
340:398	600:700	-0.8585	0.1116
340:398	700:800	-1.0462	0.1345
340:398	100:800	-0.6388	0.2839

Table 5.1 Phase above land for various parts of scene 103.

X interval (range)	Y interval (azimuth)	Mean phase	Standard deviation
0:50	470:520	-1.577	0.1522
50:100	470:520	-1.766	0.0917
100:150	470:520	-1.784	0.0838
150:200	470:520	-1.796	0.0956
200:250	470:520	-1.824	0.0967
250:300	470:520	-1.803	0.1409
300:350	470:520	-1.762	0.2035
350:374	470:520	-1.786	0.1542
0:374	470:520	-1.761	0.1520

Table 5.2 Phase above land for various parts of scene 104.

5.2.2 Velocity calculation

The next step is to calculate the current velocity. This is done *before* a coregistration is performed because after coregistration near and far range lines in the coregistrated image have unknown boundaries. Moreover, they are interpolated.

The formula to transform from phase to (slant range) velocity was already given in chapter 2. It reads

$$\Delta\varphi = \frac{4\pi}{\lambda} u\Delta t = \frac{4\pi}{\lambda}\frac{u}{V} B_x \,, \tag{5.1}$$

with u the velocity in the direction of the radar, Δt the time difference between the reception of the same signal by the two antennas, V the velocity of the aeroplane, and B_x the baseline in the flight direction of the two antennas, which is assumed to define the x-axis. This velocity is transformed to ground velocity v_G by:

$$v_G(R) = \frac{-\Delta\varphi\,\lambda V}{4\pi\, B_x \sin\theta}, \tag{5.2}$$

with

$$\theta = \arccos\left(\frac{H}{R}\right), \tag{5.3}$$

R being the slant range, and H the height of the aeroplane.

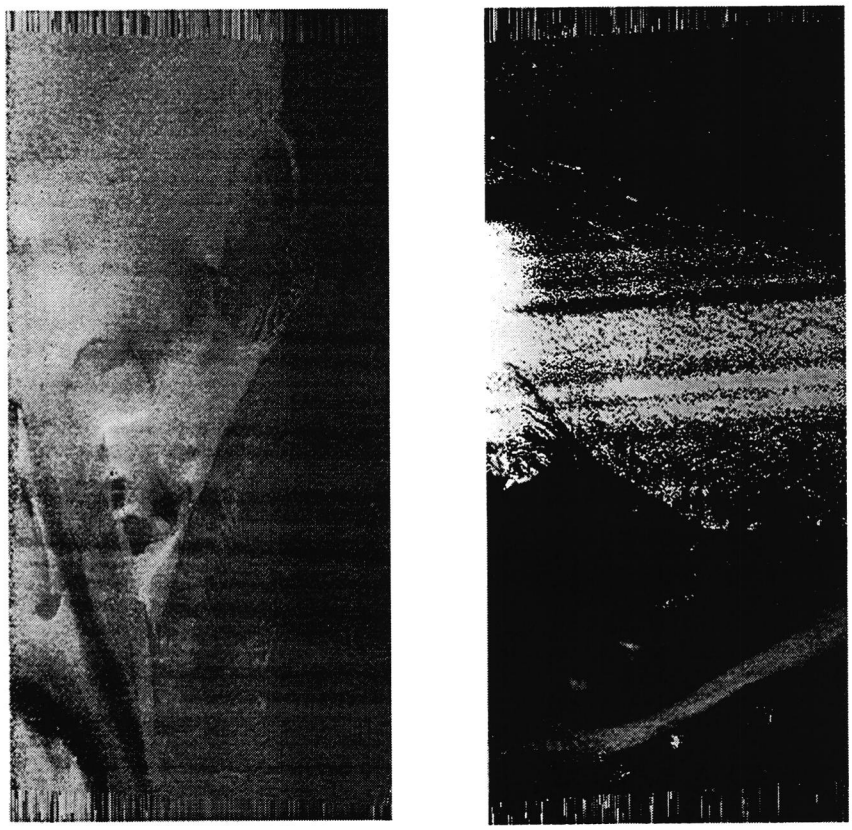

Figure 5.2 Velocity magnitude images for scene 103 (left) and scene 104 (right).

Parameter	Values 103	Values 104
$V_{aircraft}$ [m/s]	80.2129	83.7709
λ [m]	0.031	0.031
B_x [m]	0.87119	0.87119
H [m]	3155.95	3157.01

Table 5.3 Parameters for scenes 103 and 104.

The parameters concerning the two images are given in Table 5.3. The resulting velocity images (in m/s) are shown in Figure 5.2. The images in Figure 5.2 are still in slant range. The images display the velocity in a grey scale. White colour is the highest velocity and black is the lowest. The velocities are absolute, so 1.5 m/s has the same colour as -1.5 m/s. In the right panel of Figure 5.2 the phase jump on the land is clearly visible as the black-and-white pattern. In the left panel of Figure 5.2 no phase jump is visible. The velocity sensitivity is horizontal in Figure 5.2. Some horizontal "bands" disturb the image, giving an error of about 0.1 - 0.2 m/s. They are due to aeroplane movements which are not properly corrected for. The direction of the velocity, either from left to right or from right to left, depends on the tidal phase. Since the images were taken on June 9, 1997 around 16:00 UTC, the tide was ebbing on that moment. The water is therefore running from top to bottom in the left panel of Figure 5.2, and from left to right in the right panel.

5.2.3 Corrections

The velocity as shown in Figure 5.2 contains several components. One of these components is the surface current we want to know.

Another component is the wind drift. The wind causes an extra speed of the surface of the water. It is estimated equal to 5% of the wind speed at 10 m anemometer height. The wind speed during the ATI measurements is about 6.1 m/s from a direction of 270° true north. This leads to a wind drift correction of the current velocity of -0.085 m/s for image 103, and of 0.296 m/s for image 104.

The radar signal scatters to a large extend from water waves with specific wave length and direction, the so-called Bragg waves. These have their own velocity relative to the (moving) water, which must be taken into account. The E-SAR operates in X-band. At this frequency, the Bragg waves have an isotropic angular distribution. The contribution of waves moving towards the radar equals that of waves moving away from the radar. The net effect on the velocity therefore cancels, so no correction for movement of the Bragg waves is needed at X-band.

Another distorting effect is the shift in azimuth, Δx, in the image of the pixels having a velocity U_r in the range direction. It is given by

$$\Delta x = \frac{R}{V} \cdot U_r \,, \tag{5.4}$$

with R the slant range distance and V the aircraft speed. The higher the velocity, the larger the shift in azimuth. This effect is analogue to the overlay effect that occurs in interferograms with great elevation. As in that analogue, an external current field (DEM in XTI case) is needed to correct for this shift. Equation (5.4) can be used to estimate its maximum. For image 103 we have R < 5880 m, V = 80.77 m/s, and U_r < 1.03 m/s. This gives

an absolute maximum displacement of 75 m. For image 104 it equals 105 m, using $R < 5880$ m, $V = 83$ m/s, and $U_r < 1.49$ m/s. As will be shown later, these shifts may be neglected.

5.2.4 Coregistration

Each of the scenes 103 and 104 gives one component of the current velocity. The scenes must be combined in order to obtain the current velocity vector. Before coregistration the velocity images have to be converted from slant to ground range. The images were masked so land really has zero velocity. The pixel spacing is 6.49 m in azimuth and 6.50 m in range.

Coregistration is done with the use of Ground Control Points (GCP). These points are selected in one image and have to be entered in the other image. The collection of GCP is done in the coherence images because of better resemblance. Image 104 was projected on image 103 so the results will only contain the overlapping areas. Figure 5.3 shows the velocity images for scenes 103 and 104 after coregistration. The velocity field of scene 103 (left panel in Figure 5.3) shows the velocity component in the vertical direction.

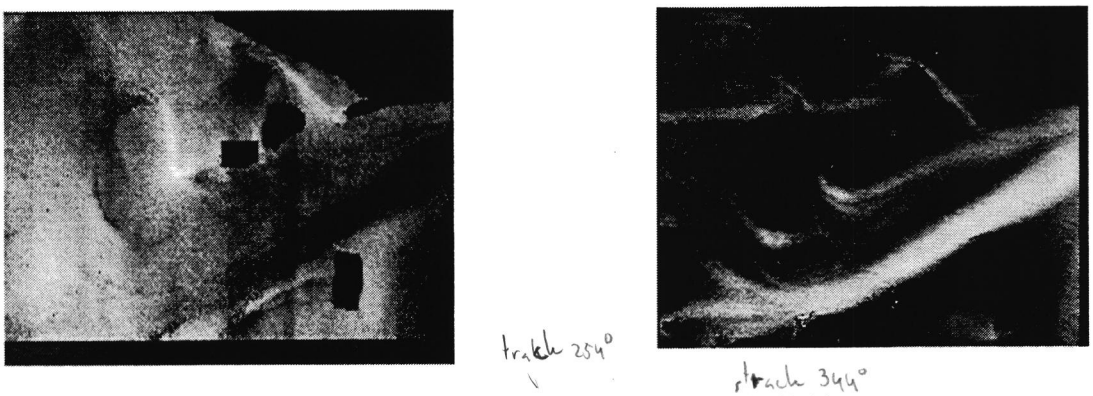

Figure 5.3 Velocity values in ground range for scene 103 (left) and scene 104 (right).

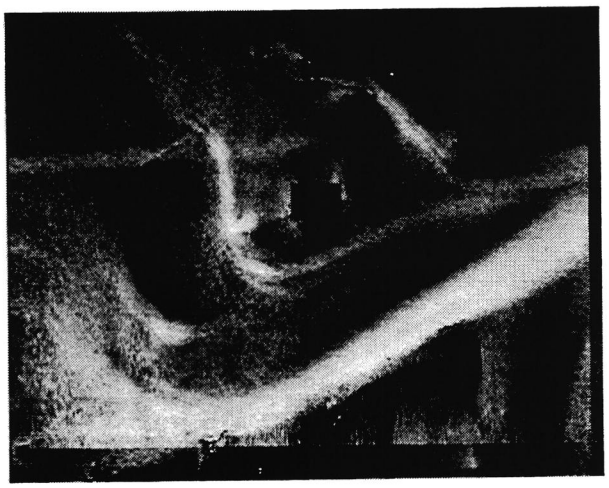

Figure 5.4 Magnitude of the current velocity.

The velocity field for scene 104 (right panel of Figure 5.3) contains the horizontal component. The band in the upper left part of the image is very annoying because it has an considerable influence on the data values. The velocity range is 1.47 m/s for scene 103 and 1.97 m/s for scene 104, so the grey scales in Figure 5.3 are not comparable. The two images were combined as described above to produce a vector field of the current. Its magnitude is shown in Figure 5.4. The boundary of scene 103 is visible in the bottom part. Data points below it only have a horizontal component and must be cut out by hand.

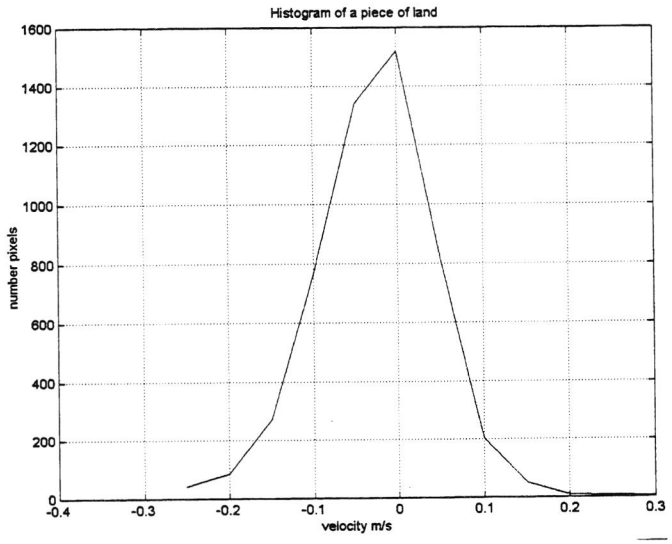

Figure 5.5 Histogram of the velocities above land.

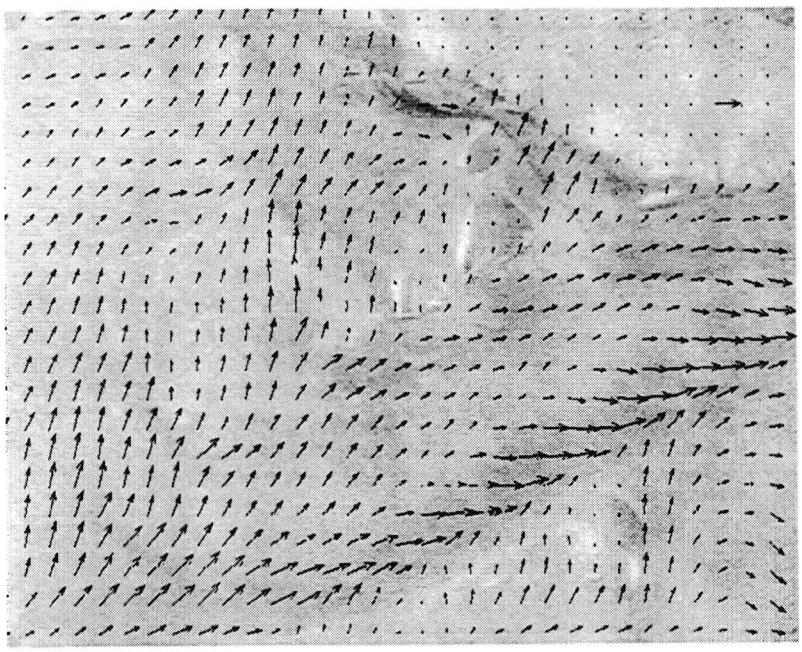

Figure 5.6 Current velocities over the amplitude image of scene 104. Image size is 2 × 3 km^2.

5.3 Flow map results

The processing steps described in the previous section result in a vector field of the surface current. Figure 5.5 shows a histogram of the velocities above land. The standard deviation is inferred to be 6.4 cm/s from this figure. This can be compared to the theoretically expected value of the error in velocity due to receiver phase noise (see also section 7.2). At the 6.5 × 6.5 m^2(slant range)resolution employed here, assuming a SNR of 10 dB, the theoretical error is 1.6 cm/s. Clearly, the measured error is significantly higher. If the measured error were to be explained by receiver phase noise, the SNR would have to be -2 dB. This value is rather low, indicating that the error in velocity is dominated by other effects, such as imperfect platform motion and attitude control. Also decorrelation may add to the error.

Figure 5.6 shows a vector plot of the current velocity overlaid over the amplitude of scene 104. The plotted vectors are averaged over 15 × 15 values, and have a minimum of 0 m/s and a maximum of 1.29 m/s. The arrow in the upper right corner stands for a velocity of 1 m/s. The distance between the arrows is 90 m in both directions. The higher velocities of the current in the bottom right part of the image are clearly visible. These are associated with outflow through a gully caused by the ebbing tide.

5.4 Flow map validation

Before the flow map obtained from the ATI measurements can be analysed further, it must be georeferenced. This is done by hand by selecting ground control points above land on the amplitude images and on the digital topographic map, following the same procedure as in section 4.4.

The ATI current field, further referred to as the measured current field, has a grid size of 8 × 8 m^2, whereas the calculated current field has a grid size of about 440 × 170 m^2, see section 3.5. Note that this grid size is larger than the maximum azimuth shift due to pixel motion, which was estimated 105 m at most in section 5.2. This effect can therefore be neglected. In order to be able to compare the two fields, it is necessary to transform one field to the grid of the other. It makes no sense to interpolate the WAQUA calculation to the fine grid of the observations. Therefore, the measured current was calculated on the WAQUA grid using the following simple procedure:

- Each point on the 8 × 8 m^2 grid of the ATI measurements (further referred to as the fine grid) was assigned to the closest point on the 440 × 170 m^2 WAQUA grid (further referred to as the coarse grid). As the fine grid falls completely within the coarse grid, every point of the fine grid is assigned to a point of the coarse grid.
- For each point of the coarse grid, the assigned ATI measurements are averaged. Some of the coarse grid points fall outside the area covered by the radar and have no ATI measurements assigned to them. Other points may have more than 1000 ATI measured current velocities assigned to them.

Following this procedure, the fine details in the ATI measurements are lost, but the effect of phase noise on the current velocity reduces by a factor $\sqrt{1000}$ to a value of about 0.2 m/s, and can safely be neglected. Figure 5.7 shows the results. The measured current, bottom panel of Figure 5.7, is strong above the western gully and around the shoal south of Ameland. The calculated current, middle panel of Figure 5.7, is strong above both the southern and the eastern gully. The top panel of Figure 5.7 shows the difference between the two current fields (the calculated field minus the averaged measured field). The average difference in magnitude is 0.202 m/s, the average difference in direction is 50°. The maximum difference in magnitude is 0.62 m/s; that in direction 179°.

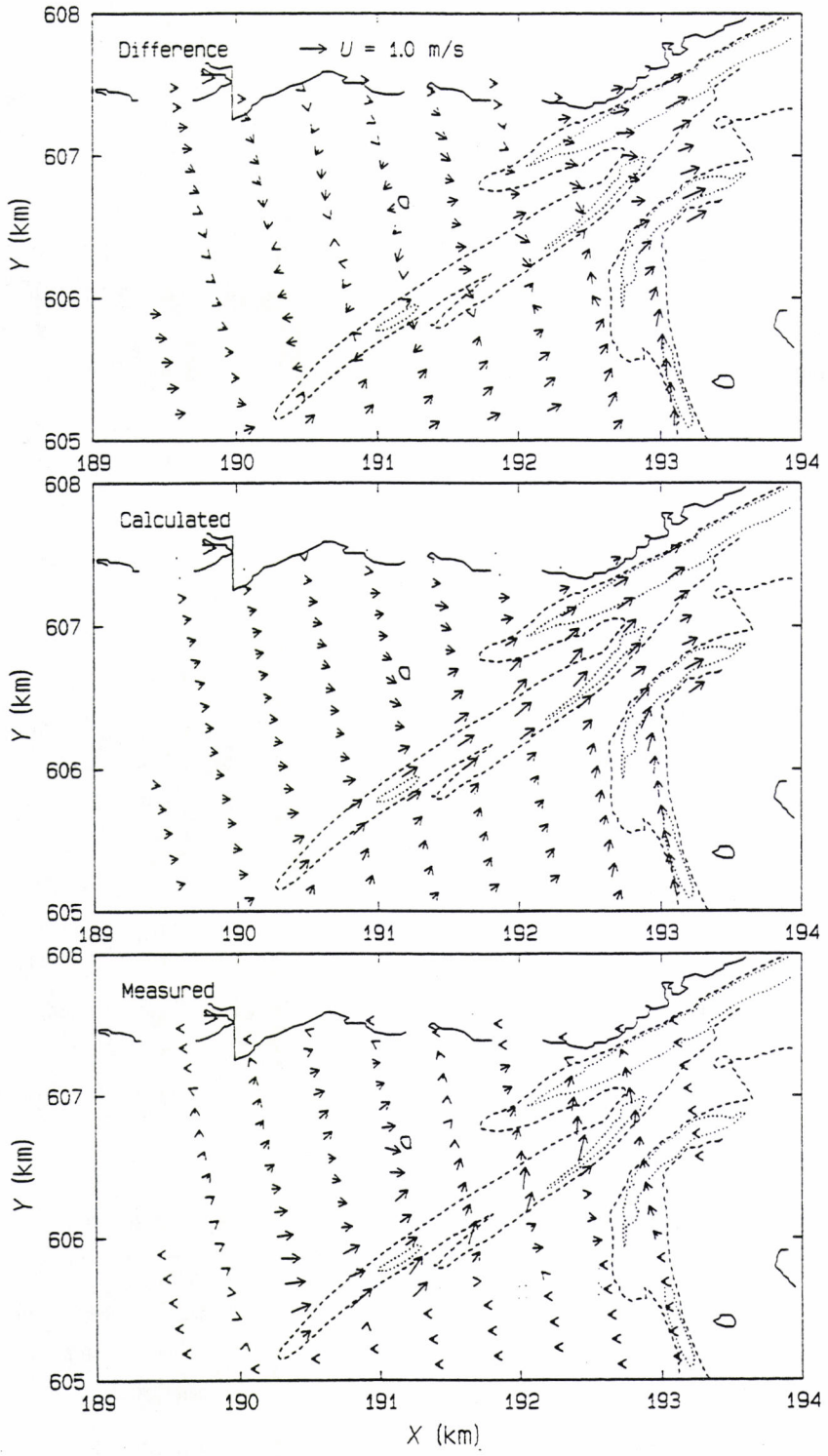

Figure 5.7 Current fields on the coarse grid of the WAQUA model. The lower panel shows the measured surface currents, the middle panel shows the calculated depth-averaged currents, and the top panel shows the difference between the two. Contour lines are at 0 m (solid curves), -2.5 m (dashed curves), and -5 m (dotted curves).

The largest differences occur at the eastern side, where the model predicts strong currents over the gullies which are not seen by the radar, and north of the gully, where the measured currents are directed to the North while the calculated current is more directed to the East. The measured and calculated current fields show some considerable differences. Part of this discrepancy may be caused by the fact that the radar measures the surface current velocity whereas the model calculates the depth-averaged current. These quantities are not the same and should, strictly speaking, not be compared to each other. Moreover, the current is calculated on a coarse grid that represents the bottom structures poorly. From Figure 5.7 it can be inferred that the profile of the gullies are covered by a few grid points only. This may cause errors in the small scale circulation pattern. Finally, the wind drift correction is 0.31 m/s in magnitude, while the maximum measured current velocity is about 1.5 m/s. The wind drift correction is important. A uniform wind field has been assumed, but local variations may cause local differences in wind drift that may account for the differences between measured and calculated current. All these effects may contribute to the differences between measured and calculated currents.

5.5 Consistency

The amplitude images clearly show bottom structures due to wave-current interaction. This phenomenon has been discovered by De Loor in 1969 [*De Loor en Brunsveld van Hulten*, 1978]. The imaging mechanism consists of three steps, as first described by *Alpers and Hennings* [1984]:

1. Interaction between (tidal) flow and bottom topography produces spatial variations in the current velocity at the sea surface.
2. Variations in the surface current velocity modulate the wind-generated spectrum of water waves.
3. Modulations in the wave spectrum cause variations in the radar backscatter which show up as intensity variations in radar images.

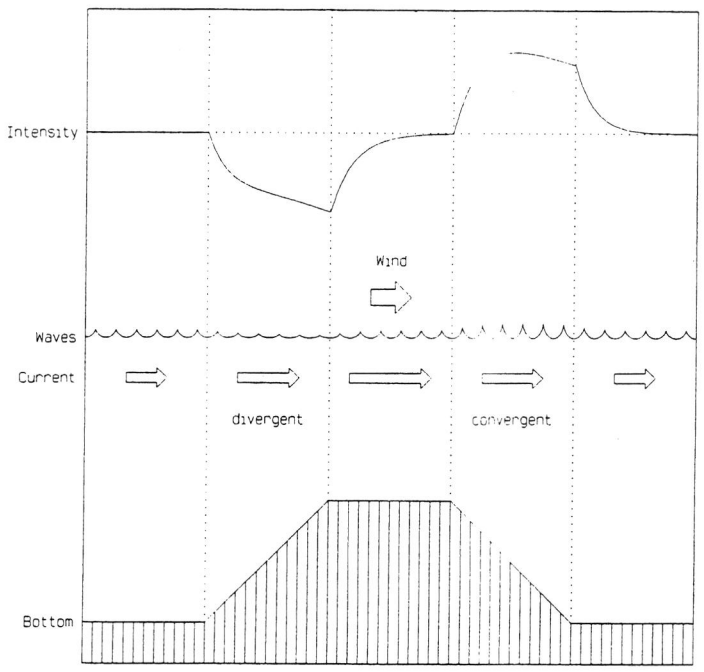

Figure 5.8 Scheme of the bottom topography imaging mechanism.

The imaging mechanism is schematised in Figure 5.8. As the surface current is measured by the radar, only the second and third step of the mechanism need to be taken in order to predict the modulations in the amplitude image.

The radar cross section was evaluated using first-order Bragg scattering. In this model, the radar backscatter is proportional to the wave height spectral density evaluated at plus or minus the Bragg wavenumber vector $\mathbf{k}_B$. Its direction is parallel to the radar look direction, its magnitude is given by

$$k_B = 2k \sin\theta \tag{5.5}$$

with k the radar wavenumber and θ the angle of incidence. It is well known that first-order Bragg scattering at X-band underestimates bottom-induced modulations. The effect of waves longer than the Bragg waves must be taken into account in the scattering model by using a two-scale model or a radar backscatter model based on the Stratton-Chu integral equation [*Vogelzang*, 1998]. However, this requires information on the complete two-dimensional wave height spectrum. Though in principle possible, this calculation would take too much computer time. On the other hand, the modulation pattern, i.e. the extend of areas with increased or decreased radar cross section, depends little on the scattering model used. For a qualitative comparison, first-order Bragg can be used.

The action balance equation with a quadratic relaxation source term was solved in four-dimensional position-wavenumber phase space using the method of characteristics. The parameterisations of the equilibrium wave height spectrum and the relaxation rate were chosen the same as in [*Vogelzang*, 1998] for describing the SAXON-FPN data. The input flow field was obtained by averaging the ATI flow map over 4 × 4 pixels to a resolution of 32 × 32 m^2. In this way, phase noise is averaged out, so it will not be interpreted as bottom induced current variations. Moreover, the flow map is more easily handled by the software for the imaging mechanism.

Figure 5.9 shows the result for image 103. The radar range direction is from left to right, the flight direction from bottom to top. The main features of the measured amplitude image are reproduced in the simulation. The model predicts that the northern wall of the gully shows up dark, while the southern wall shows up bright. The observations show the same pattern, though the dark modulations are broader and extend more across the bend. The bright arc in the left part of the observed image is reproduced well in the simulation. The agreement is good, certainly in view of the approximations made in the model for the imaging mechanism.

Figure 5.10 shows the results for image 104. This image has its range direction from bottom to top. Both the observed and the simulated image 103 show less bottom-induced modulations than image 104. The agreement is less than for image 103. The model predicts that the southern wall of the gully shows up bright, which is not confirmed by the observations. The bright arc left in the observed image is reproduced well in the simulation, as was the case for image 103.

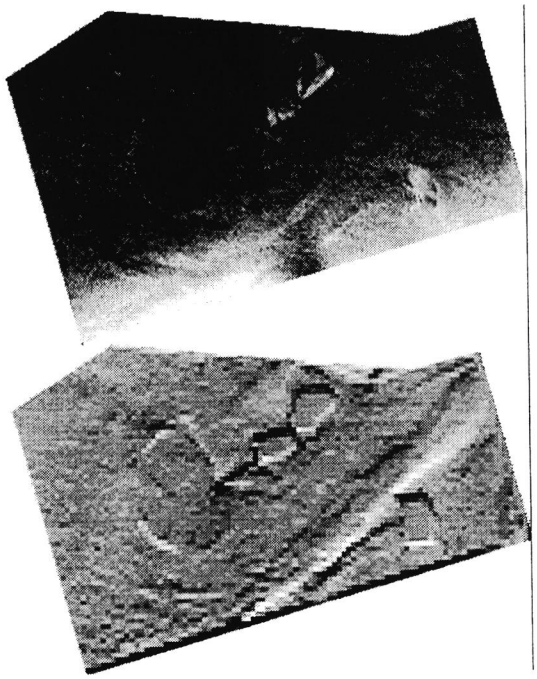

Figure 5.9 Simulated (bottom) and measured (top) amplitude images for scene 103.

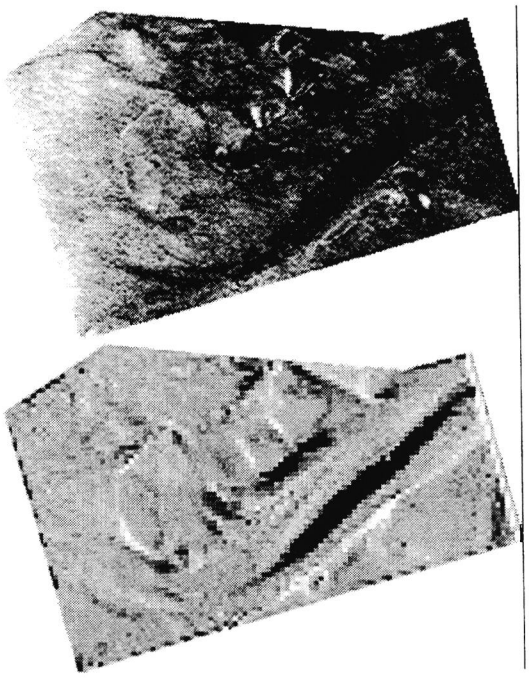

Figure 5.10 Simulated (bottom) and measured (top) amplitude images for scene 104.

5.6 Concluding remarks

From the results obtained in sections 5.2 and 5.3, the following conclusions are drawn:

- The magnitude of the current velocities ranges from 0 - 1.29 m/s with a root-mean-squared (r.m.s.) accuracy of 6 cm/s. This error does not seem to be dominated by receiver phase noise, but by aircraft motion and attitude effects, and possibly by decorrelation.
- Good phase data without much artefacts and errors or noise are needed in order to produce a good velocity vector field.
- Wind drift is corrected for using observations from nearby stations, but no actual site readings of wind were available.
- Bragg scattering and azimuth shift errors can be neglected.

From the analysis in sections 5.4 and 5.5 the following conclusions are drawn:

- The images must contain good identification points for precise mapping with the proper co-ordinates and for selecting GCP's, because limited auxiliary information exists of the data.
- There are considerable differences between the observed current field and the model hindcast, due to differences in grid size, differences between surface current and depth-averaged current, and/or inhomogenities in the wind drift that are not corrected for.
- The simulated modulations due to wave-current interaction using the measured flow field as input agree quite well with the observed ones.

Further research is needed to find the cause for the difference in the current fields. It is recommended to calculate the surface current using a three-dimensional model. It is also recommended to run the flow model with a much smaller grid size.

Chapter 6 CORRELATION

6.1 Introduction

This chapter deals with the relation between surface change and decorrelation. Satellite radar images of Ameland are used to study the decorrelation. To analyse this relation, additional data from field surveys and vector data from the topographic service in the Netherlands (TOP10vector) are included. To process these data sets, several existing software packages are used and a number of programs developed.

In SAR images, the magnitude and the phase of each element of an image are the coherent summations of the backscattering and phase of the individual scatterers inside a resolution cell. In a changing structure and/or chemical composition of the ground cover, the amount of temporal decorrelation will vary and this information can contain information about the type of ground cover or the situation in which it exists. The influence on temporal changes in case of spaceborne sensor-systems can be minimised by a high temporal resolution of the system or by a combination of two "identical" systems in a tandem mode. In this case ERS-1 and ERS-2 images are used from which thematic information can be extracted, based on the coherency of the input data sets. Coherence maps are created from the SAR data set that are in complex format. Each element of the map is the level of coherency in the local region of that element [*Huurneman*, 1998].

The SAR decorrelation refers to change in the position of the individual backscatterers in the field of view and refers, as such, to geometric characteristics. It represents unique information that is complementary to information obtained by optical observation. The variation in the overall phase and the overall magnitude of cells with equal cover type will appear as speckle. However, two images taken from the same position at the same moment will be identical (neglecting system noise). If two images are taken from different positions and/or instants of time, variations in pixels representing the same surface will appear.

In using decorrelation for thematic information extraction, the decorrelation related to the base line should be minimised. If the decorrelation related to the baseline is zero, the remaining decorrelation is caused by temporal changes in composition and the structure of the ground cover within the cells. In practice a zero baseline will not exist, but with a short baseline almost no baseline decorrelation exists. So differences that appear might be attributed to temporal decorrelation. The data can be used as an additional dimension in the feature space for the combined image analysis [*Huurneman et al.*, 1996].

6.2 Data preparation

The TOP10vector data were gridded and the individual maps that covered almost the whole area of the island of Ameland were glued together. The coherence map was created and georeferenced to the geometry of the topographic map. Ground truth was collected in the field at the two days the ERS SAR images were recorded.

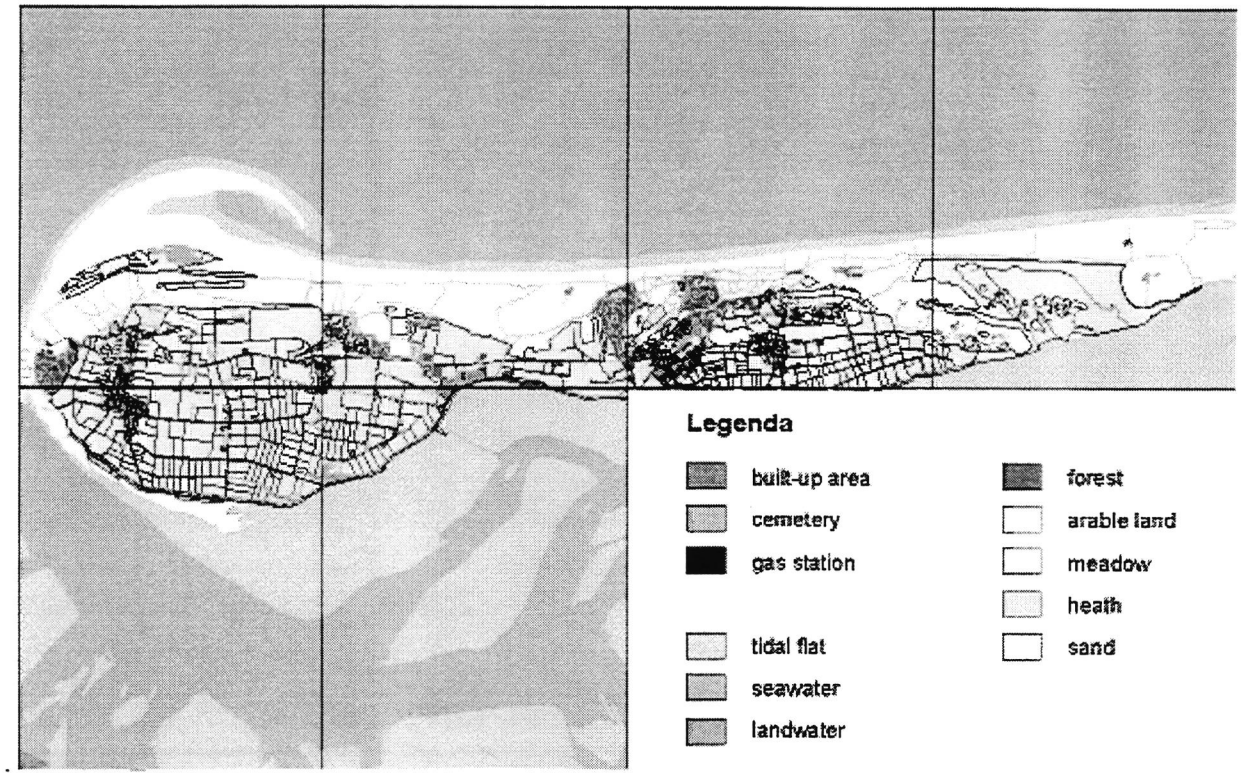

Figure 6.1 Topographic map of the isle of Ameland from TOP10vector data.

6.2.1 TOP10vector data

The TOP10vector data set is a product of The Topographic Service (TDN), based in Emmen (the Netherlands). The Topographic Service builds up a range of digital data files on the basis of aerial photographs and land surveys. The TOP10vector is the most detailed data set produced by the Topographic Service. It is a vector file with a closed surface structure, built from coded and interconnected linear elements. However, the TOP10vector is not a real database, object types and attributes are stored by means of element coding. The files are divided into units, the areas of which match the size of the topographical map series. The TOP10vector files used for this research are in DXF format.

DXF is a format for CAD applications. It can also be read by most GIS applications. The disadvantage of this format, however, is that the Topographic Service codes and source codes are eliminated. This means that the elements only consist of DXF characteristics such as: level, colour, and line style. For this research the format is still useful. The TOP10vector files are VLK-files which also include closed polygons of the surfaces. From the individual polygon maps, the topographic classes of interest (see Figure 6.1) are masked out. Then the maps are gridded and glued together to one complete topographic map.

6.2.2 Field data

Using the DESCW software of ESA, two ERS1/2 SAR data tandem pairs of Ameland were selected. The first pair was planned for May 9 and 10, 1996 and the second for June 13 and 14, 1996. At these days fieldwork was carried out. The aim of the fieldwork was to collect information about the weather conditions at the time of sat-

ellite overpass and to describe the condition of the ground cover (sand and vegetation). The weather conditions at the selected days are listed in Table 6.1.

Date	Satellite	Wind	Atmosphere
9 - May - 1996	ERS -1	NNE - 6	Half clouded - dry
10 - May - 1996	ERS -2	NE - 5	Clouded - rainfall
13 - June - 1996	ERS -1	NW - 4	Light clouded - dry
14 - June - 1996	ERS -2	NW - 4	Clouded - dry

Table 6.1 Weather conditions.

On the island of Ameland the following landscapes and land cover types are recognised:

1. *Beach.* Ameland is at the east, the north and the west bounded by, in some parts, very broad sandbars which are sometimes flooded. These areas did hardly change in shape in the 35 days between the first and the last pass of the satellites. Only minor changes due to wind causing little dunes were sometimes detected. However the moisture contents of the sandbars changed significantly between some of the dates that the satellites passed. On the sandbars there is no vegetation.
2. *Young dunes.* On the edges of the sandbars new dunes are formed, varying in height from 1m to 10 m. In some cases they lie along the waterline, e.g. in the North-west of the island and further everywhere at the sides near the elder part of the island. These new dunes are not or hardly covered by vegetation.
3. *Old dunes.* Adjacent to the new dunes, going towards the South, the old dunes are the dominant landform. These old dunes are covered by a dense and relatively dry vegetation that varies in height and composition, see Figure 6.5. It can be found on a large part of the island sometimes reaching from the new dunes along the North Sea to the Waddensea in the South. These dunes vary in height from about 3 m to 15 m. Between the old dunes there are areas which are relatively flat and which are covered by low vegetation, mainly grass.
4. *Villages.* The villages in Ameland are small and there is a high variation in vegetation and buildings. The buildings are small and surrounded by relatively large gardens.
5. *Forest.* Some areas are covered by mixed forest.
6. *Meadows.* In the agricultural area in the south-western part of the island, a large number of small parcels, about 40 × 200 m^2, with grass vegetation exists. Some of these parcels are covered by young grass with an average height of about 7 cm, others with old grass of about 20 cm. Other parcels are used for hay or for grazing.
7. *Wetland.* Behind the dunes in the north-western part of Ameland and also in the southern part, some small lakes and areas with water minded vegetation exist.
8. *Fords.* South of Ameland is the Waddensea consisting of fords, mudflats, shallow water, and trenches.

During the fieldwork, the locations of the above mentioned classes were identified and indicated on topographic maps of scale 1:50 000. Also videos were produced to get an idea of changes that appeared in the period of 35 days between the different days of data acquisition by the ERS 1/2. The fieldwork gave the following changes between the different images:

- Due to the extreme different weather conditions between May 10 and the three other days (rainfall and dry weather) we cannot expect a high coherence between these images.
- The vegetation in the agricultural areas was significantly different in height between the days in May and the days in June, which will be clear because of the growing season.
- Small changes appeared on the beach and in the young dunes due to the wind conditions.
- The wetlands were also different in May and June due to the growing vegetation.
- On part of the beach at the North side of the island in the neighbourhood of the village of Ballum, Rijkswaterstaat was busy to top up the beach with sand during the days of data acquisition in June.

Hardly any difference was visible between the vegetation in the old dunes (low moisture contents), the forest and the villages. Especially the conditions were almost equal for all classes at the two days in June. During these days even the large sandbar at the north-western side of the island did not change. However it did not consist of completely dry sand. In fact, only the wind could cause differences in shape and structure of the vegetation and sand in the 24 hours between the data acquisition.

6.2.3 Radar data

For this research, the two tandem pairs of radar data listed in Table 6.2 were selected and ordered at NLR.

Date	Satellite	Orbit	Frame	Track
9-May-1996	ERS-1	25189	2529	151
10-May-1996	ERS-2	05516	2529	151
13-June-1996	ERS-1	25690	2529	151
14-June-1996	ERS-2	06017	2529	151

Table 6.2 Radar data.

Unfortunately, the ERS-2 was not programmed at May 10 for the acquisition of SAR data. So finally we got only three data sets. These data sets were processed from RAW data format into SLC format by DLR/D PAF in Oberpfaffenhofen, Germany. The baseline information is obtained from the European Space Agency via Earthnet Online. This information is given in Table 6.3.

	ERS1- 13 June Horizontal	ERS1- 13 June Vertical
ERS-1 9-May	297m	824m
ERS-2 14-June	44m	76m

Table 6.3 Baseline information.

6.3 *Data processing*

To generate a coherence map, the first crucial point is the input of SLC data sets of which the phase has been correctly preserved during processing. That means that for each point, the phase on the zero Doppler line must have been extracted with high accuracy. Expecting that the processing of the RAW data sets has been executed

with care, the three data sets are further processed to realise a number of coherence maps. The essential steps in that process are:

- selection of the area of interest;
- coregistration;
- coherence computation.

These steps are discussed below.

6.3.1 Area selection

The parts of the data sets that contain a large part of Ameland (see Figure 6.2) are extracted from the original data by means of the Earthview INSAR software. Earthview is an image analysis software package from Atlantis Scientific Inc.

Figure 6.2 ERS-1 image of the test area.

6.3.2 Coregistration

For the creation of a coherence map, two SAR-images have to be registered with sufficient accuracy, since the phase difference of the individual pixels in the two images is used for the coherence of an small area. In fact the two SLC's must fit on top of each other with an accuracy of less than 0.1 of a pixel. The automatic image registration, which is part of the INSAR software, was not able to achieve this accuracy due to the limited area of the region and the large part of water in which the software could of course not find any common point. To overcome this problem, the semi-automatic mode for registration was applied. This method is based on visual inspection and manual selection of common points in the images after which a matching technique refines the setting. In this way a number of points with high backscattering in the two images were found, mainly in the villages. These points were used to register the images to an overall root mean squared error of less than 0.02 pixel for the June images.

6.3.3 Coherence computation

The coherence map of the June images was computed. It turned out that the computation is a bit strict and the manipulation of the process by means of parameters is limited. To increase the freedom of processing, the coregistered data sets were stored in the Atlantis internal format and further treated by programs that were developed for this research.

Each element of the map is the level of coherency in the local region of that element. The resolution of the coherence map is related to the size and contents of the operator kernel used in the computation of the coherency. In this section, the influence of some operators on the resolution of a coherence map is investigated.

The magnitude and the phase of each element of a SAR image result from coherent summation of the backscattering and phase of the individual scatterers inside a resolution cell. Correlation between the data from a cell in different images is expressed in terms of the summated phase and intensity of the resulting backscatter. A cell is considered to contain a set of individual backscatterers distributed over the cell. The amount of energy backscattered by these individual scatterers can be equal or can vary and the positional distribution of them is regular or irregular. In a non-homogeneous cell the dominant scatterers will have the highest influence on the phase, therefore variation in the position of dominance will vary the phase significantly. These points with a relatively high response (see Figure 6.2) will also have a too large influence on the computation of the coherence map shown in Figure 6.3. This influence can be reduced by means of a filter combination as described below.

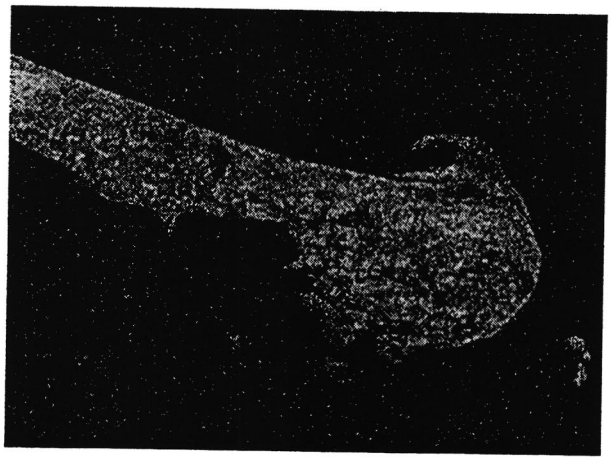

Figure 6.3 Coherence map of the ERS-1/2 pair.

Apart from temporal changes, decorrelation can also be a consequence of an improper distance between the two sensors during data acquisition (too large baseline). In case of the extraction of thematic information, the decorrelation related to the baseline should be minimised such that differences can be considered to originate mainly from temporal decorrelation.

Coherence

The complex coherence γ_C between two SAR images S_1 and S_2 is defined by *Touzi et al.* [1996] as

$$\gamma_C = \frac{E\left(S_1 \cdot S_2^*\right)}{\sqrt{E\left(|S_1|^2\right) E\left(|S_2|^2\right)}}, \tag{6.1}$$

where E denotes the expectation value and the star indicates complex conjugation. The estimator of the coherence is defined as

$$\hat{\gamma} = \frac{\left| \sum_{j=1}^{M} a_{1j} a_{2j} e^{i\Delta\phi_1} \right|}{\sqrt{\sum_{j=1}^{M} a_{1i}^2 \cdot \sum_{j=1}^{M} a_{21i}^2}}. \tag{6.2}$$

For each pixel, the coherence is computed in a window. The value between 0 and 1 is related to the equality of the bi-directional signal of the two sub-images (from master and slave). A constant phase shift between the corresponding elements of the images does not modify the coherence, as it is eliminated in (6.2). However, the influence of a strong backscatterer (e.g. a corner reflection) dominates its surrounding in the computation of the coherency. This results in a high coherence over a larger area than would be the case in reality. For example, an element in a sub-image of the same size as the kernel of the (filter) operator (40 × 7 elements) represent a very strong scatterer (e.g. thousand times the scatterers in its surrounding) in both the ERS-1 image and the ERS-2 image. This strong scatterer will overrule the other elements at a distance smaller than the kernel size. Therefore a large kernel (e.g. 150 × 150 m^2 in ground size) shows a very high coherence over that area without being realistic.

If the coherence map is used for thematic information extraction, then important information can be hidden by this way of coherence computation. The images in Figure 6.4 visualise this unwanted effect. The data used for these pictures is artificial. One image is created using a randomiser (Figure 6.4a) and the second one is derived from the first by a "controlled" phase shift (Figure 6.4b). One element of the first and the corresponding one of the second got a relatively very high value. From these two data sets in complex format the coherence is computed by means of the formula given above. In Figure 6.4c the result is shown. The images contain 25 × 25 elements. An average filter (kernel size is 5 × 5 elements) is applied for the filtering of the components of the formula.

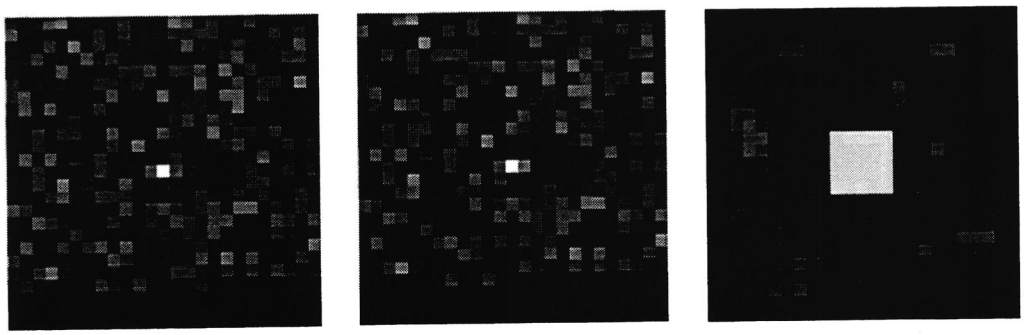

Figure 6.4 Simulated data. Left: master image, centre: slave image, and right: coherence between the two.

As can be seen in Figure 6.4, the central pixel in the master and slave have a big influence on its surrounding at the coherence computation. To avoid this, an adapted filter can be used for example a Gaussian weighted mean or a sinc function. However this will hardly give an improvement since the kernel size of the coherence filter can not be too large. If the kernel is too large, a smoothing of the coherence will be the result and this will reduce the effective resolution of the coherence map. The lower the resolution the less thematic information remains. But a small kernel size will not be effective in case of a corner reflection since a too strong fall off in the contribution of the sub-image elements will lead to a coherence map that consists of the coherency which is computed from almost only individual points. Such a coherence map will show up a high variation in coherency, leading to noisy result.

To give each element the same "strength" in the computation of the coherence in a window, the complex vector must be normalised, which means that the coherence computation is only based on the phase information. In the case that an average filter is used for the computation, the phase of each element gives the same contribution to that computation. In Figure 6.5 the coherence of the normalised images is given.

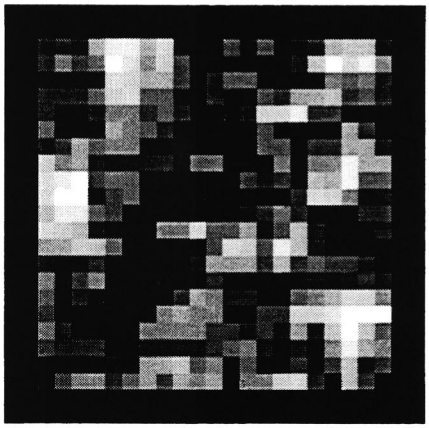

Figure 6.5 Coherence map of normalised images.

The disadvantage of the coherence computation from normalised images is that those points with a high backscatter and a high coherence get a significant lower coherence value assigned because of the strong influence of their surrounding.

It can be concluded that a filter process should be developed that avoids the reduction of the coherence value in case of strong coherent scatterers and on the other hand these strong scatterers should not increase the coherence value if that is not valid. For that purpose, a modified average filter is used. The function of this filter is the computation of the coherency of a sub-image without taking the central element in account. The centre of the filter kernel is equal to zero. In Figure 6.6 the coherence maps that are created by the two types of average filters are shown. The different functionality is clearly demonstrated in the centre of the image.

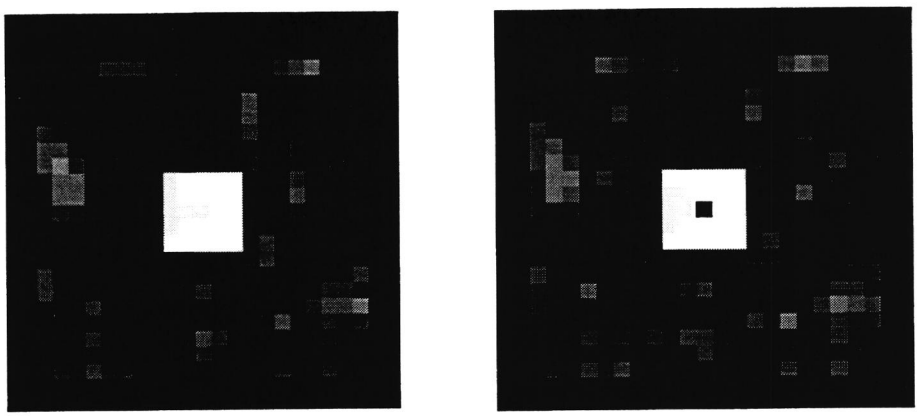

Figure 6.6 Coherence map with complete average filter (left) and with incomplete average filter (right).

The following process is developed to improve the resolution of the coherence map:

1. Compute the coherence map with an average filter where each sub-image element gives the same contribution.
2. Compute the coherence map with an average filter where each sub image element gives the same contribution except the centre element of that sub-image. In this case, the centre of the kernel is zero.
3. Compute the normalised master and slave images.
4. Compute the coherence map of the normalised images.
5. Compare the elements of the coherence maps that are created with the two average filters.

The two coherence maps that result from the two filters are usually different, especially at those points where the backscatter differs significantly from the surrounding. In practice this will mainly appear in points with a high backscatter. The following steps are executed to finalise the process.

6. The difference in coherence between the two maps is computed.
7. If that difference is larger than a given threshold, then the coherence value that is computed with the complete average filter is assigned to the final coherence map. Otherwise, the final coherence map gets the value that is computed using the normalised images.

The absolute difference between elements of the two coherence maps will easier exceed the threshold in areas with an overall low coherence than in areas with a relatively high coherence. To avoid an imbalance in the assignment of the final coherence, it is required to adapt the threshold to the local situation. It is also possible to add another component in the computation of the value to be tested. In this research, the last method is applied. The test value is computed as the product of the coherence value, applying the complete average filter and the difference between the two coherence maps. The method used can be described briefly in the following way:

- C_1 is the coherence value that is computed with the complete average filter.
- C_0 is the coherence value that is computed with the average filter of which the kernel centre is equal to zero.
- C_n is the coherence value that is computed from the two normalised images.
- C_f is the final coherence map.
- σ is the threshold

The following statement is used for the final assignment:

$$\textbf{IF } \sigma < |C_0 - C_1| \textbf{ THEN } C_f = C_n \textbf{ ELSE } C_f = C_1 \tag{6.3}$$

Figure 6.7 shows the coherence map that is produced using the above-mentioned process with the artificial data. It is clear that the influence on the neighbouring elements of the point with the high backscatter in the centre of the images disappeared and that the more realistic coherence of these neighbours remains. The element in the centre however kept its high coherence value.

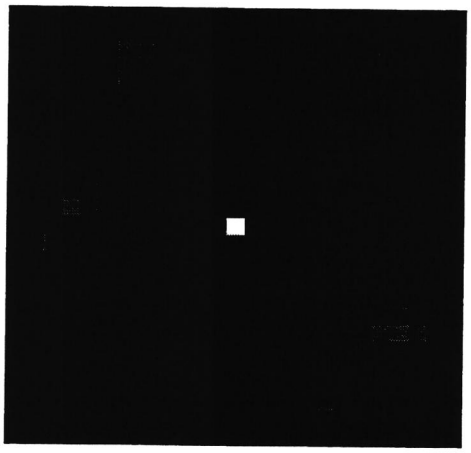

Figure 6.7 Improved coherence map.

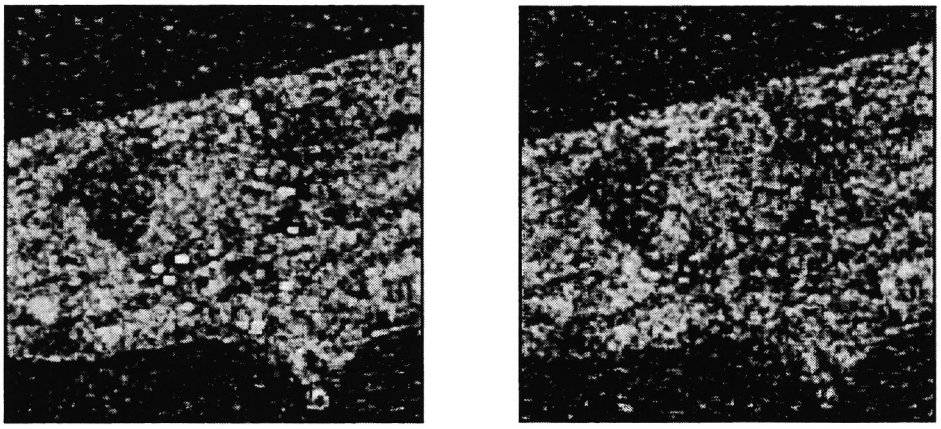

Figure 6.8 Coherence map of a small area at Ameland created with conventional filtering (left) and with a combination of filters as described in the text (right).

The coregistration of the Single Look Complex SAR images is performed with the INSAR processor of Atlantis Scientific. The master (ERS-1) and the slave (ERS-2) images are, after the coregistration, further processed by in house developed software modules. The software modules are written in the languages IDL for I/O and visualisation and in C for the filtering and other time consuming operations. Data conversion is executed in the ITC image processing software, ILWIS. The dimensions of the filters that are used for the coherence map creation are 15 lines and 3 columns. This corresponds with an area of about 60 × 60 m^2 in the terrain. Figure 6.8 shows

the coherence map that is created using conventional filtering (left), and the one that is created applying the procedure described in this chapter (right). Finally, the coherence map from the images of 13 and 14 June is produced using the method that is described in this section.

6.4 Data analysis

To enable the analysis of the coherence map, it is necessary to geo-reference the map. After the geo-referencing, the map can be combined with other data sources in the same co-ordinate system.

6.4.1 Geo-referencing

First of all, the coherence values are scaled from the range 0 - 1 (floating point) to the range 0 - 255 (integer) to facilitate comparison and visualisation. The errors introduced this way can be neglected. Next, a slant range adjustment is performed in the program ERDAS Imagine. With the information of ESA, the parameters (depression angle, beam width and height) were set and the image was resampled to a 20 m resolution. The slant range adjustment corrects for the angular distortion from near range to far range. Before the coherence image could be geo-referenced, the image was first mirrored to avoid large rotations in the final step which could lead to roundoff errors. In the last step the coherence map was resampled based on an affine transformation to register the coherence image to a topographic map in RDM co-ordinates. The result is shown in Figure 6.9.

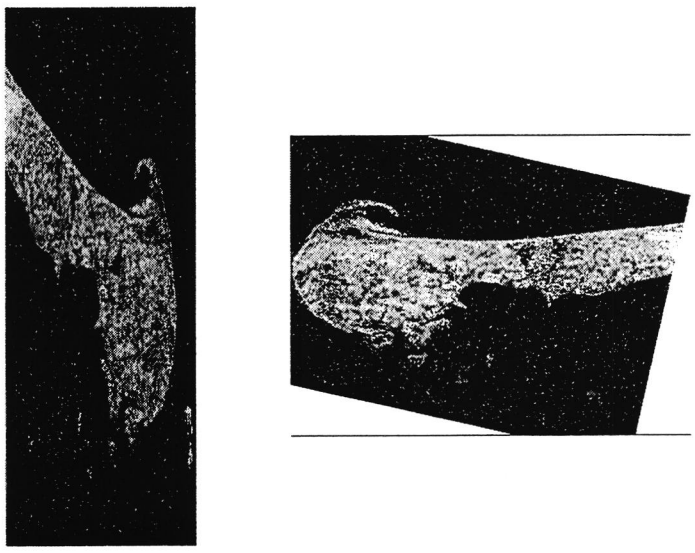

Figure 6.9 Coherence map before (left) and after (right) geo-referencing.

6.4.2 Data segmentation

Geo-referencing puts the coherence map and the topographic data in the same co-ordinate system. The software package ILWIS, developed at ITC, is used to perform operations that are required to overlay and to analyse the data. The main objective is to find whether any relationship exists between the coherence values and the following basic land cover classes:

- Forest
- Arable land
- Meadow
- Heath
- Sand

Before the coherence values can be classified and the link between field data and coherence values can be investigated in more detail, the coherence values should be spatially clustered. It is hoped that these clusters coincide with the spatial distribution of the field data (parcels). The basic idea behind this clustering is the assumption that a strong correlation exists between spatially adjacent pixels. Another method that smoothens a high frequency of changes is segmentation of the coherence map based on the parcel boundaries of the ancillary data from the TOP10vector.

The purpose of image segmentation is to subdivide an image into different parts (segments) that correspond to objects in the terrain [*Gorte*, 1998]. In this case the subject of study is to try to find homogeneous areas from almost homogeneous areas in the coherence image which can be classified according to the field data. First the coherence image was stored in a quadtree data structure using quadtree software. This quadtree data structure and software help to decrease storage requirements and processing time simultaneously. A 'split and merge' algorithm was used to generate objects from the coherence image. Split and merge creates segments that coincide with quadtree leaves. Unfortunately, the user has to apply trial and error to find suitable threshold values and to visually inspect the segmentation results. If the result shows too many small segments, such that many (supposed) terrain objects are still subdivided, the final threshold value should be increased. Conversely, if too many terrain objects are combined into single segments, the final threshold value should be lowered [*Gorte*, 1998]. Appendix D shows the 'split and merge' results.

The TOP10vector data contain detailed information about parcel boundaries. Assuming that within one parcel there is no difference in land cover type, this data set can be used to create a boundary map. Overlaying it on the coherence map, the average and predominant coherence value for every parcel can be computed. From the TOP10vector data set the field boundaries are extracted and rasterised to a 10 m resolution to conserve the contiguity of the field boundaries. To overlay the coherence map with the boundary map the coherence map with a resolution of 20 m should be resampled to a 10 m resolution. Before the overlay operation was performed the boundaries are extracted from a topographic vector file covering almost the whole island of Ameland. First quadtrees are created. Second, using a program for connected component labelling, unique identifier is determined for each map unit. Finally, the two maps are overlaid with an aggregate operation and the statistics for every parcel are computed. These statistics are stored in a table. From that table the parameters average value (avg) and predominant value (pred) are used to give every parcel the corresponding value (avg or pred) from the statistics table. See appendix E for a map with the average coherence value for every parcel and a map with the predominant coherence value for every parcel.

To investigate the link between field and coherence the statistical distribution of the computed coherence in the selected bounded areas are visualised. In Appendix C the graphs of the histograms are shown with the number of pixels that have a certain coherence value for each topographic class. All topographic classes have a Gaussian distribution. The results show that it will become very difficult to classify these coherence values according to field data, because there is a large overlap between the statistical distribution of the different land cover classes. Another reason why classification can become a problem is that all coherence values are from one band (one

dimension). To increase the change of an acceptable classification, the ancillary vector data is included in the process.

To be able to compare the field data with the computed coherence values for every parcel the coherence map is classified. This classification is performed by means of slicing the coherence values into different classes. To overcome the problem of overlap between classes of different land cover types which would be classified as the same class, first a cross operation is performed. The cross operation compares the values of the pixels on the same position in two maps. The first input map is the topographic map with the basic topographic classes, and the second input map is the map with the average coherence values per parcel. Also a cross operation is performed using the map with the predominant coherence value per parcel, as second input map. The combinations of the pixel values in both maps are stored in a table and an output map. The next step was to assign colours to these classes of different combinations. The hue of the colour represents the topographic land cover class to which the subclasses belong. The intensity within that hue corresponds to the coherence value for that subclass. See appendix F for the results.

6.5 Discussion

6.5.1 Coherence

Due to the relative long period (35 days) between the data acquisition of the May and the June data sets, it was not possible to get a coherence map of them. So finally the research had to be done on the ERS 1/2 tandem pair of 13 and 14 June. At these days the meteorological circumstances were equal, sunny, and a moderate wind (4 Beaufort) from almost the same direction. There was no rainfall during data acquisition and the days before.

The baseline of the two images is 44 m in horizontal and 76 m in vertical direction. The dry weather and the small baseline are ideal to get high coherency in those areas where the ground cover does not change rapidly. So low coherency in some areas is caused by changing structure of vegetation due to wind. The level of change that can be extracted from the coherence map can be used as a feature in classifications.

The ground truth of the area of interest is collected from the TOP10vector database and from fieldwork at the days of data acquisition. The selected area covers about 60% of the island of Ameland at the western side. It contains forest, dunes, villages, beach, shallow water, and grass in different growing, grazing and harvest stages. The influence of strong scatterers on the coherence is reduced by an adapted filter technique. This was needed because the parcels with different ground cover are small relatively to the size of the kernel that is used to calculate the coherence. The resolution of a coherence map is increased by using a combination of linear average filters instead of using a single average filter. In the combination, one of the filters is with the central sub-image pixel included and the other one without. The difference in coherence between the maps created using these filters is compared with a threshold. If the difference exceeds the threshold, the coherence is calculated with the "complete" filter. Otherwise the coherence from the normalised images is used. The high coherence of points with high backscattering values remains with this approach without influencing too much the coherence of neighbouring points. The thematic information in the resulting coherence map is not reduced in the surrounding of strong scatterers.

6.5.2 Quality and accuracy of the results

During the processing of the different data sets, errors are introduced. In this section all kind of different operations are listed that are required to get the input data sets in the same geometry. The raster images with the topographic data are glued together. Within every glue operation the output map is automatically resampled according to the georeference of the first input map, because the new output map needs a new (extended) georeference. It can be considered that this will not introduce significant errors. The final topographic raster map is used as master to register the coherence image to this topographic map. First the coherence image has to be transformed from slant range into ground range. Because the coherence image used for this project is a subset of the original coherence image, the parameter "beam width" was set to 1/6 of the original angular distance. For exact settings, this should be computed more accurately. Still, the error introduced by this transformation is considered to be of minor influence. The coherence image in ground range has to be transformed once more to the geometry of the topographic map. Within this final step the (overall) accuracy is dependent on the selection of the tiepoints.

The selection of appropriate tiepoints in the coherence image is a difficult operation, because there are hardly any areas in the image with sharp edges that allow comparison to objects in the topographic map. Also with the selection of every new tiepoint a new error is introduced, because of the uncertainty in position of that point in the two images. Finally, four tiepoints were selected and an affine transformation was applied. After this transformation the coherence map and the topographic map have almost the same geometry.

6.5.3 Analysis

In the analysis part of this project the segmentation method was used to find homogeneous areas (objects) in the coherence image. This is not a useful method, because the segmentation can only be performed on one band. The overlap of the coherence values between separate land cover classes causes a merging of two segments which have different land cover types. This overlap problem also excludes the use of classification as a method to find homogeneous areas, which still can be compared to the field data.

Therefore, the only method that is useful to find those homogeneous areas is by using ancillary data. The boundaries of the parcels from the topographic data set are used for overlaying these boundaries with the coherence map. Assuming that within each parcel the land cover type is the same, the corresponding coherence value is computed.

One drawback of using this data set as ancillary data is that the field boundaries in the parcels at June 13 and 14 are sometimes not the same as the field boundaries extracted from the topographic data. In that case the assumption that within one parcel the land cover is the same, is not correct. Therefore, the positions of the field boundaries from the topographic data set should be updated.

The topographic classes are subdivided into three to four classes with an equal class width. Only the topographic class "meadow" has eight classes of equal class width. The reason for this is that for this topographic class there is detailed field data available. For the purpose of this project, this subset of the final coherence map is visually compared with the corresponding subset of the field data.

6.6 Concluding remarks

Through comparison with ground truth data the relation between decorrelation with surface change is investigated. This experiment was performed with a data set from the island of Ameland situated in the northern part of the Netherlands. The relation between land cover and decorrelation is visualised. However, it was not possible to find a direct link between the computed coherence value per parcel and ground truth data.

On the basis of visual inspection of the final classified coherence map with field data there might be a relationship between these two data sets. From the topographic class "Meadow" the subclasses with a high coherence value should coincide with short grass and the subclasses with a low coherence value should correspond to long grass. For some parcels this is true, however, this relationship is not that straightforward that it is possible to put it in a coherence prediction model

In general it became clear that even under almost ideal circumstances with respect to baseline and climatological circumstances, the coherence drops even within a period of 24 hours in areas with dense vegetation like forests and in areas with water,. Also in areas with grass vegetation the overall coherence is low. Only in areas with dry vegetation like old dune vegetation, the coherence is relatively high, probably also because of the more stable structure of that vegetation, which makes it less sensitive to wind.

It is recommended that, if coherence maps are used for topographic and/or thematic information extraction, the selection of the date(s) and time of data acquisition is carefully made. The time between the acquisition of the data sets should be as short as possible because the influence of only wind in areas covered by many types of vegetation is significantly. Further it should be investigated how the coherency computation could be improved considering the whole range of processing steps, from RAW data to coherence map. Also, the research as is described in this chapter, could be repeated for areas with larger parcels such that the influence of adjacent parcels can be eliminated.

Chapter 7 OPERATIONALISATION

7.1 Costs versus accuracy

7.1.1 XTI

Besides across track interferometry, there are other techniques to measure the data needed for constructing digital height maps:

- tachometry
- GPS
- analytical photogrammetry
- soft copy photogrammetry using aerial photographs or airborne video
- laser altimetry
- CAESAR stereo

These techniques were compared to each other in terms of costs and accuracy in the project "Framework digital elevation models Dutch coast" [*Huising et al.*, 1996]. The present study to XTI can be regarded as an addendum. In their study, *Huising et al.* identified laser altimetry as the best technique in terms of costs and accuracy for mapping large areas. The accuracy is 15 cm r.m.s., while systematic errors are less than 5 cm. The measurement density ranges from 1 point per 20 m^2 for airborne systems to about 1 point per 1 m^2 for helicopter-borne systems. The costs for mapping 1 km^2 ranges from Dfl. 500 to Dfl. 2000 using airborne systems, but may increase to Dfl 6000 for helicopter-borne systems, depending on the measurement density.

The accuracy of the XTI DEM's obtained in this study ranges from 1 m to 3 m, depending on the nature of the surface. This is too inaccurate for operational use in the Netherlands. The flight and processing costs needed to arrive at the two DEM's of Terschelling were about Dfl 180000. With each DEM measuring about 3 km^2, this results in a price of about DFL 20000 per km^2, which is about an order of magnitude more expensive than laser altimetry. Of course, this cost comparison is not completely fair: the XTI data were recorded using an experimental radar system, while laser altimetry is offered on a commercial base.

The figures presented above seem highly unfavourable for interferometry. However, interferometric data gathering and processing is offered on a commercial base by Aero-Sensing Radarsysteme GmbH in Oberpfaffenhofen. On tidal flats, their system is able to produce DEM's with an accuracy of 5 cm at costs comparable to those of laser altimetry [*Wimmer et al.*, 1999; *Moreira*, 1999]. If this claim proves to be correct, across track interferometry may become a serious alternative for laser altimetry.

7.1.2 ATI

It was shown in chapter 5 that detailed maps of the surface current can be obtained from ATI measurements. Such maps can be used for calibration and validation of detailed 3D flow models and for studies to the flow patterns in rivers. Alternative methods for measuring currents are:

- HF radar;
- shore-based radar;
- in-situ current meters like Acoustic Doppler Current Profilers (ADCP).

The costs involved in an HF radar deployment are of the same order of magnitude as those needed for an ATI flight, about Dfl. 150000. The accuracy of HF radar is of the order of 5 cm/s. This is more precise than ATI, but interferometry yields a much higher spatial resolution which can be traded for accuracy. An ATI flight will yield a few maps, whereas HF radar delivers flow maps every 20 minutes during several months. HF radar has a typical resolution of 200 m. This is much coarser than that for ATI, but comparable to the grid size of today's high resolution models.

In-situ current meters give accurate data, but on one position only. However, they are relatively cheap and measure the current velocity at some depth. Their precision of the order of several cm/s, depending on the type of instrument. Shore-based radar may also be a cheap alternative, but its potential in terms of accuracy and resolution is insufficiently clear at this stage.

For model calibration and validation, ATI has to compete with the other techniques. ATI is the obvious technique only when extremely high spatial resolution is needed. ATI may also be used to study the detailed flow patterns in rivers. This requires the very high spatial resolutions that only ATI can deliver. However, ATI only gives instantaneous overviews of the surface current at relatively high costs, which may be a drawback.

7.1.3 Differential interferometry

Differential interferometry allows mapping of land subsidence and deformation with an accuracy of the order of millimeters. The technique is a combination of repeat-pass interferometry and along-track interferometry. It measures the velocity of the (land) surface at a time scale of the order of days, weeks, or months. It is necessary that the sensor follows almost the same path: too much deviation causes baseline decorrelation. The precise orbit constraints depend on the platform altitude and the radar characteristics.

Differential interferometry has not been studied within this project. However, mapping of land subsidence is important for the water management in the western part of the Netherlands. Measurement of dike deformation is important for monitoring the safety of the defences against flooding, on a regular base as well as during high water situations. These applications need further attention. Temporal decorrelation may be a limiting factor, as efficient monitoring requires sufficient correlation over a year or longer. Longer radar wavelengths may be the solution, but the price to be paid is decreased accuracy.

7.2 Implications for PHARUS

7.2.1 Introduction

The present research has clearly demonstrated the value of an interferometric capability for airborne SAR. In order to do this, it was necessary to use a foreign system, because the Netherlands' system PHARUS did not possess an interferometric option at that time. The applications for which the interferometry proved useful were: shore line detection, DEM extraction and surface current mapping. Since the start of this project, PHARUS has developed a few extra interferometric options. While no second antenna – the most basic and probably optimal solution for interferometry – has been installed, it has nevertheless become possible to:

a) Operate PHARUS in dual-pass XTI mode, and
b) Operate PHARUS in split-antenna ATI mode.

The dual-pass XTI mode has two applications: DEM extraction and monitoring the secular motion of the earth surface, in particular land subsidence. The split-antenna ATI mode also has two applications: surface current mapping and Moving Target Indication (MTI). In Table 7.1, relevant interferometric parameters of E-SAR and PHARUS are compared. The following discussion will make reference to this table.

7.2.2 Land subsidence monitoring

With the dual-pass mode, XTI data can be obtained by flying nearly the same track twice; the data from the two cross-track separated antennas are taken consecutively instead of simultaneously. This mode is presently being tested for the application of land subsidence monitoring. The objective of this application is to locally estimate the amount of vertical displacement of the surface. The accuracy to which this kind of measurement is possible with PHARUS can be of the order of a centimeter. The accuracy is a function of baseline (cross-track antenna separation), horizontal resolution, temporal decorrelation of the scene and the precision of the flight track maintainance and measurement. For a 1 meter baseline, 5x5 m horizontal resolution, no temporal decorrelation and no errors in the flight track, 1 cm accuracy for subsidence should be possible to reach with PHARUS. To what extent this number is deteriorated by flight track errors and temporal decorrelation is at present being investigated in the project "Repeat Pass Interferometry".

7.2.3 DEM extraction

In addition to subsidence, dual-pass XTI can also be used for DEM extraction. This application has not been explored with PHARUS yet, partly because it needs processing software to be developed. The expected accuracy for the DEM can be estimated by using equation 4.4. From this relation it follows that a r.m.s.error in the phase difference values $\sigma_{\Delta\phi}$ leads to a r.m.s. height error σ_h of:

$$\sigma_h = \frac{\lambda H \tan\theta}{4\pi B_\perp}\sigma_{\Delta\phi} \,. \tag{7.1}$$

At the same time, the RMS phase difference error can be written as [*Otten and De Vries*, 1995]:

$$\sigma_{\Delta\phi} = \frac{1}{\sqrt{N}\sqrt{SNR}}, \tag{7.2}$$

with *SNR* the signal-to-noise ratio in the SLC image and N the number of SLC pixels that are coherently averaged to obtain one height value. This expression is not valid for *SNR* values below 1. (Note that *SNR* is defined in terms of power, not amplitude.)

Substituting the relevant values and assuming an *SNR* of 10 dB (Table 7.1), we find a single-look height accuracy of 1.8 m for E-SAR, i.e., the height accuracy at a horizontal resolution of 2.1 m x 0.6 m. The PHARUS single-look height accuracy is 0.9 m, i.e., at 5.2 m x 1.25 m horizontal resolution. In order to better compare these numbers, they can both be brought to the same multi-look horizontal resolution of 5.2 m x 5.2 m. At that resolution, the height accuracy for both E-SAR and PHARUS is the same: 40 cm.

In practice, this accuracy is deteriorated by temporal and baseline decorrelation effects and by imperfectly corrected platform motions. Due to the dual-pass nature of PHARUS, the temporal decorrelation will be much larger than for E-SAR. Also platform motion correction will be more difficult, since the constraint of fixed antenna separation is not present. On the other hand, a PHARUS baseline of 5 m was used in the calculation,

while larger baselines, leading to increased accuracy, are possible. For the PHARUS case conform Table 7.1, the maximum baseline (at which baseline decorrelation is complete) is 35 m. Also, the assumption of 10 dB for the SNR is very rough; SNR values for PHARUS and E-SAR may differ, depending on system sensitivity. PHARUS SNR may well be significantly higher than that of E-SAR, in part because of the lower PHARUS resolution. Furthermore, the PHARUS pulse repetition factor can be much higher than that of E-SAR: up to 4 times as high, leading to an improvement by a factor of 2.

With dual-pass interferometry, one has the possibility to freely choose the interferometric baseline, thereby optimally adapting the needed accuracy and tolerated ambiguity to the situation. Also, there are no extra costs involved with hardware extensions of the system (although software extensions for the processing are still needed). In spite of these advantages over single-pass XTI, the problems associated with dual-pass XTI probably make single-pass a better solution for DEM mapping, as that method is less susceptible to flight track errors and temporal decorrelation, and less expensive in operation (since in dual-pass each scene must be flown twice), making it more robust and reliable for operational applications.

7.2.4 Surface current mapping

In the split-antenna mode, the PHARUS antenna is split into two parts along the flight direction. This is possible because of the phased array nature of the PHARUS antenna: the 'array' of radiating elements can be split in two (overlapping) sub-arrays. In this way, effectively two antennas are obtained, with 30 cm along-track spacing (baseline). Both antennas can be used for transmitting and receiving. This in effect turns PHARUS into an ATI interferometer. This mode has been implemented only very recently, and only one data set has been taken so far which is at present being analysed. This data set was taken over land, for MTI application. Obviously, when this mode is used over sea, in principle the same possibilities arise as with a standard two-antenna ATI system. The sensitivity for surface currents of PHARUS in this mode can be estimated by using relation 2.1:

$$\sigma_{v_G} = \frac{\lambda V}{4\pi B_x \sin\theta}\sigma_{\Delta\phi} \,. \tag{7.3}$$

Instead of the full radial velocity u as in (2.1), the ground (horizontal) radial velocity v_G is used here. For the phase difference noise $\sigma_{\Lambda\phi}$, the same formula as above (7.2) applies.

Substituting the appropriate numbers (see Table 7.1), the accuracy of E-SAR at the same horizontal resolution of 5.2 m x 5.2 m is found to be more than 10 times as high as that of PHARUS: 2 cm/s versus 30 cm/s. Such an accuracy may not seem attractive for PHARUS, but the spatial resolution of 5.2 m is in practice much too high. When the resolution is lowered to 50 m x 50 m, a very acceptable spatial resolution for a water current map, the PHARUS accuracy becomes a very good 3 cm/s. Again, an *SNR* of 10 dB was assumed for both systems. Actual *SNR* values are not known; they strongly depend on system configuration and, in the case of sea surface imaging, also on the environmental circumstances (wind speed).

Similar to XTI, these accuracies are in practice lowered by temporal decorrelation effects and platform motion errors. Concerning temporal decorrelation effects, it is worthwhile to compare the system parameters of synthetic aperture time and ATI time lag with the expected decorrelation times for the water surface. The synthetic aperture time is the time needed for the radar to gather all the data needed to make a full resolution single-look image. It is of the order of 1-2 seconds (for the case considered in Table 7.1). The ATI time lag is the time difference between the collection of the two SLC images that make up the interferometric pair.

The expected water surface decorrelation times are between 4 and 9 milliseconds. For the E-SAR, the ATI time lag at 11 ms is longer than that. For PHARUS, on the other hand, the ATI time lag is only 3 ms, shorter than the surface decorrelation. Therefore, PHARUS may be expected to suffer much less from temporal decorrelation than E-SAR and therefore perform better. For both systems, the synthetic aperture times are an order of magnitude longer than the surface decorrelation, indicating severe velocity bunching problems for both sensors.

Parameter	E-SAR	PHARUS
Wavelength	0.031	0.057 m
Ground range resolution	2.1	5.2 m
Azimuth resolution (1 look)	0.6	1.25 m
# Looks for 5.2 m × 5.2 m	21.5	4.2
XTI Perpendicular baseline	1.37 m	0 - 35 m
ATI Baseline	0.87 m	0.3 m
Platform speed	80 m/s	90 m/s
Height accuracy, 1 look	1.82 m	0.90 m *)
, 5.2 m × 5.2 m	0.39 m	0.44 m *)
Ground velocity accuracy, 1 look	0.10 m/s	0.60 m/s
, 5.2 m × 5.2 m	0.022 m/s	0.29 m/s
, 50 m × 50 m	0.002 m/s	0.03 m/s
Synthetic aperture time	1.8 s	1.1 s
ATI time lag	11 ms	3.3 ms
Bragg decorrelation time	5.9 ms	9.2 ms
Long wave decorrelation time	4.3 ms	4.8 ms

Table 7.1. Comparing interferomeric parameters of the DLR E-SAR with PHARUS. Where applicable, the following parameters have been used: Platform altitude: 3200 m. Incidence angle: 45 deg. SNR: 10 dB. *): for 5 m XTI perpendicular baseline.

7.2.5 Shoreline detection

The application of shore line detection on the basis of ATI data was shown to be successful in this project, making use of the combination of image intensity, coherence and phase. As noted above, in the PHARUS split-antenna ATI mode, the ATI time lag is shorter than the expected water surface decorrelation time, in contrast with E-SAR. Therefore, while this would lead to a better PHARUS performance for current measurements, it is at the same time expected to lead to less performance in discriminating land from water on the basis of the correlation measure.

On the other hand, PHARUS dual-pass XTI mode could be used for shore line detection. Full decorrelation is expected for water, as opposed to only partial decorrelation for the land. Also, the polarimetric capabilities of PHARUS may be applied for land-water discrimination. This would be preferable over dual-pass XTI as only one pass is needed. However, neither have yet been tested with PHARUS. At present, another BCRS project, "Interferometric shoreline mapping" is being carried out that investigates this issue, primarily with satellite SAR.

7.2.6 Future enhancements

The extension of the PHARUS system with a second XTI antenna would require a significant investment, but it would make PHARUS more attractive for operational DEM extraction. Using the same numbers as earlier (Table 7.1), a height accuracy of 1.1 m at 5.2 m horizontal resolution is expected. However, a better estimate of the actually expected accuracy of PHARUS with a second XTI antenna can be made by substituting more specific numbers than the reference values used above to compare PHARUS with E-SAR. Taking 3000 m platform altitude, 6 m horizontal resolution and an *SNR* of 15 dB we find a height accuracy of 50 cm. The 15 dB *SNR* is a realistic number for medium to high backscatter backgrounds. In case there is an interest in the very accurate determination of the average height of large, flat areas (such as meadows or tidal flats), the coherent averaging may be extended. For example, coherent averaging over an area of 100 m x 100 m will yield an accuracy of 3 cm. As before, the accuracies may worsen by decorrelation and platform motion effects (but to a lesser extent than in the dual-pass case),

A second ATI antenna would improve the accuracy for surface current measurements and for MTI. However, an improved accuracy for the former case may not even be needed. In order to decide on the desirability of an extra ATI antenna for PHARUS, the expected performance as analysed here should first be validated by an experiment.

7.2.7 Conclusions

On the basis of the above analysis, in which a few assumptions had to be made with the most important one being about the *SNR* values, it can be concluded that:

- PHARUS dual-pass XTI can give DEM accuracies comparable to E-SAR (40 cm at 5 m horizontal resolution), or even better when using a larger baseline;
- PHARUS should be able to achieve good results for surface current mapping in its split-antenna ATI mode (3 cm/s accuracy at 50 m resolution). It would be quite worthwhile to validate PHARUS's expected performance in this respect through an experiment;
- The PHARUS performance for shore line detection is not yet known, but is expected to come from its dual-pass XTI mode and from its polarimetric mode;
- Extension of PHARUS with a second antenna in XTI mode would much improve the use of PHARUS for operational DEM mapping, with expected height accuracies of 50 cm at 6 m horizontal resolution or 3 cm at 100 m resolution.

Chapter 8 CONCLUSIONS

This report describes a study to three types of interferometry: across-track (XTI), along-track (ATI), and repeat-pass. The study was held in the Waddensea north of the Netherlands. An experiment was held with the German airborne E-SAR system that can operate in both XTI-mode and ATI-mode. Not all data recorded during the experiment could be used, since the aircraft track could not be recovered to the required precision because of a DGPS failure. A selection of the XTI data was further processed to a digital elevation map (DEM) of the western part of the isle of Terschelling. This map was compared to a high precision DEM obtained with laser altimetry. Similarly, a selection of the ATI data was further processed to a map of the surface current. This was compared to a model hindcast. The measured surface current was also used as input for a wave-current interaction model to check consistency of the radar data. ERS tandem mode data were used for repeat pass interferometry. This allows the construction of coherence maps. For a large part of the isle of Ameland it is investigated if a coherence map can be used for land classification.

Form this study the following conclusions are drawn:

1. XTI allows generation of a DEM with an accuracy ranging from about 1 m for flat areas to about 3 m compared to forested areas. This agrees well with accuracies mentioned in the literature. For operational use within the Netherlands, however, this accuracy is much too poor when compared to that of laser altimetry (about 15 cm). Recent developments, however, indicate that accuracies of the order of 5 cm are feasible within reasonable costs.
2. ATI allows generation of very detailed maps of the surface current velocity. The accuracy is about 6 cm/s for a pixel size of 8×8 m^2. The observations compare well to a model hindcast, despite the fact that the model gives the depth-averaged current velocity, the poor resolution of the model, and uncertainties in the wind drift correction. ATI may be used for calibration and validation of detailed 3D flow models, and for measuring currents near structures in coastal waters and rivers. However, the azimuth shift must be corrected for if detailed current information is needed.
3. The coherence obtained from repeat-pass interferometry had little value for land topographic applications. However, it can be used for land use classification, since the coherency of the different parcels depends very strong on the land cover. Different types of vegetation in different growing stages result in different coherency. Good correlation was found only in very dry parts. In the more moist parts coherence is diminished and also the effect of wind on the (long) vegetation decreases the coherency drastically.

When using interferometry, the following should be kept in mind:

1. In case of an airborne interferometer, the flight track should be recorded to the required precision.
2. In case of obtaining coherence maps from repeat-pass interferometry, the meteo conditions during both SAR acquisitions should be carefully examined to minimise their effect.

Along-track interferometry seems a promising technique for applications like calibration and validation of flow models and, especially, detailed observations of the current field near structures in coastal waters and rivers. To learn more on the nature, precision, and usefulness of ATI observations, they should be compared to the results of a detailed 3D flow model.

Differential interferometry has not been investigated within this study. Since it can be used for mapping land subsidence and deformations, this technique may have important applications.

APPENDICES

A Flowchart

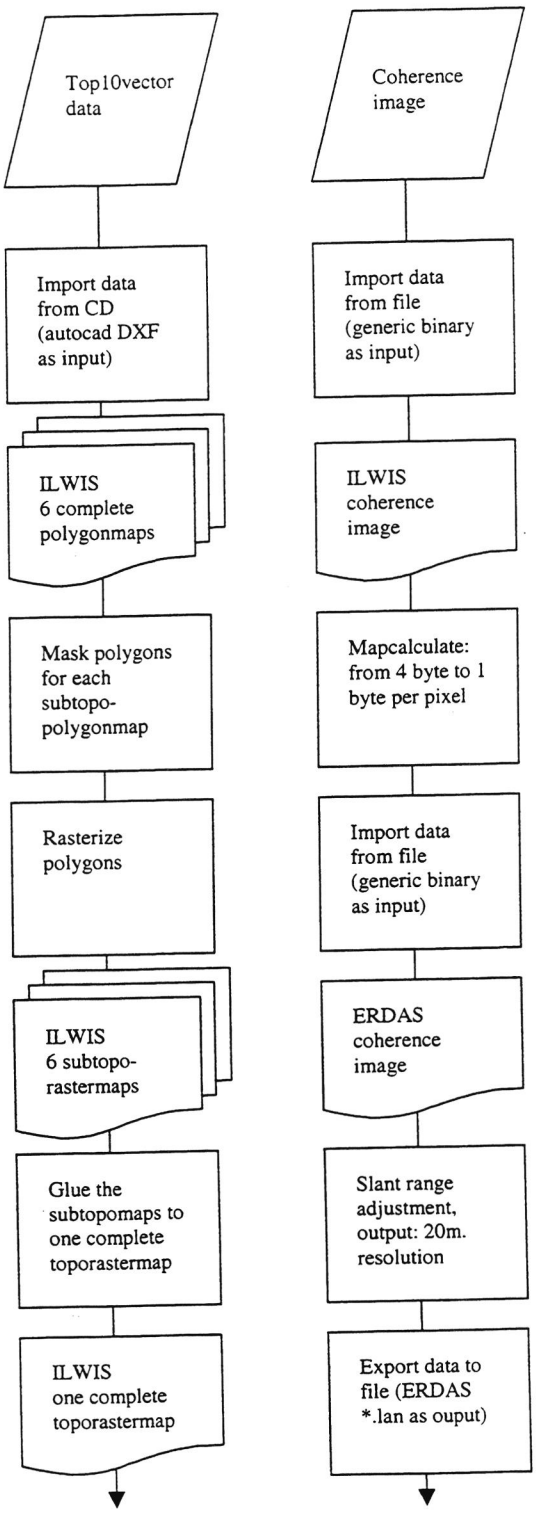

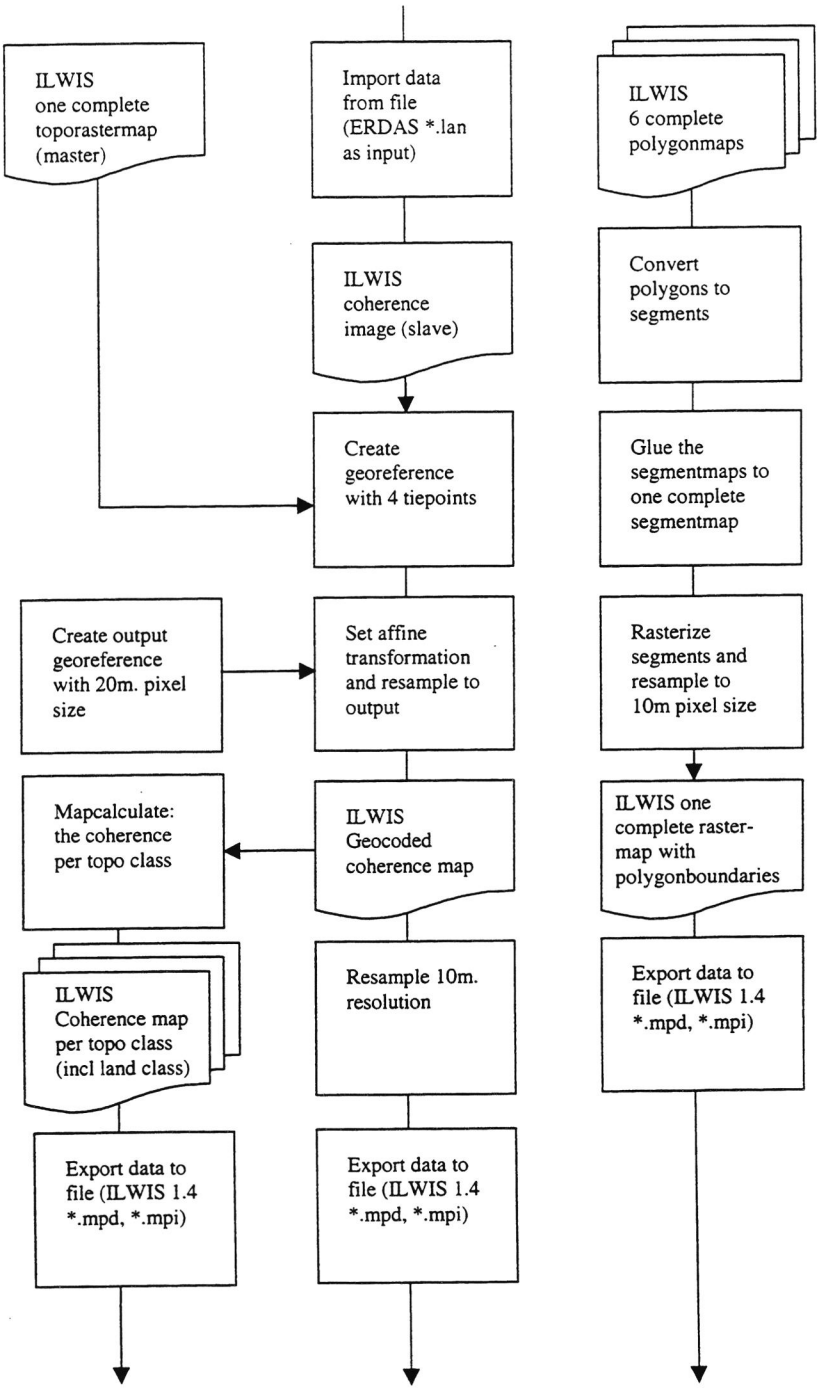
ILWIS
one complete
toporastermap
(master)
Import data
from file
(ERDAS *.lan
as input)
ILWIS
6 complete
polygonmaps
ILWIS
coherence
image (slave)
Convert
polygons to
segments
Create
georeference
with 4 tiepoints
Glue the
segmentmaps to
one complete
segmentmap
Create output
georeference
with 20m. pixel
size
Set affine
transformation
and resample to
output
Rasterize
segments and
resample to
10m pixel size
Mapcalculate:
the coherence
per topo class
ILWIS
Geocoded
coherence map
ILWIS one
complete raster-
map with
polygonboundaries
ILWIS
Coherence map
per topo class
(incl land class)
Resample 10m.
resolution
Export data to
file (ILWIS 1.4
*.mpd, *.mpi)
Export data to
file (ILWIS 1.4
*.mpd, *.mpi)
Export data to
file (ILWIS 1.4
*.mpd, *.mpi)

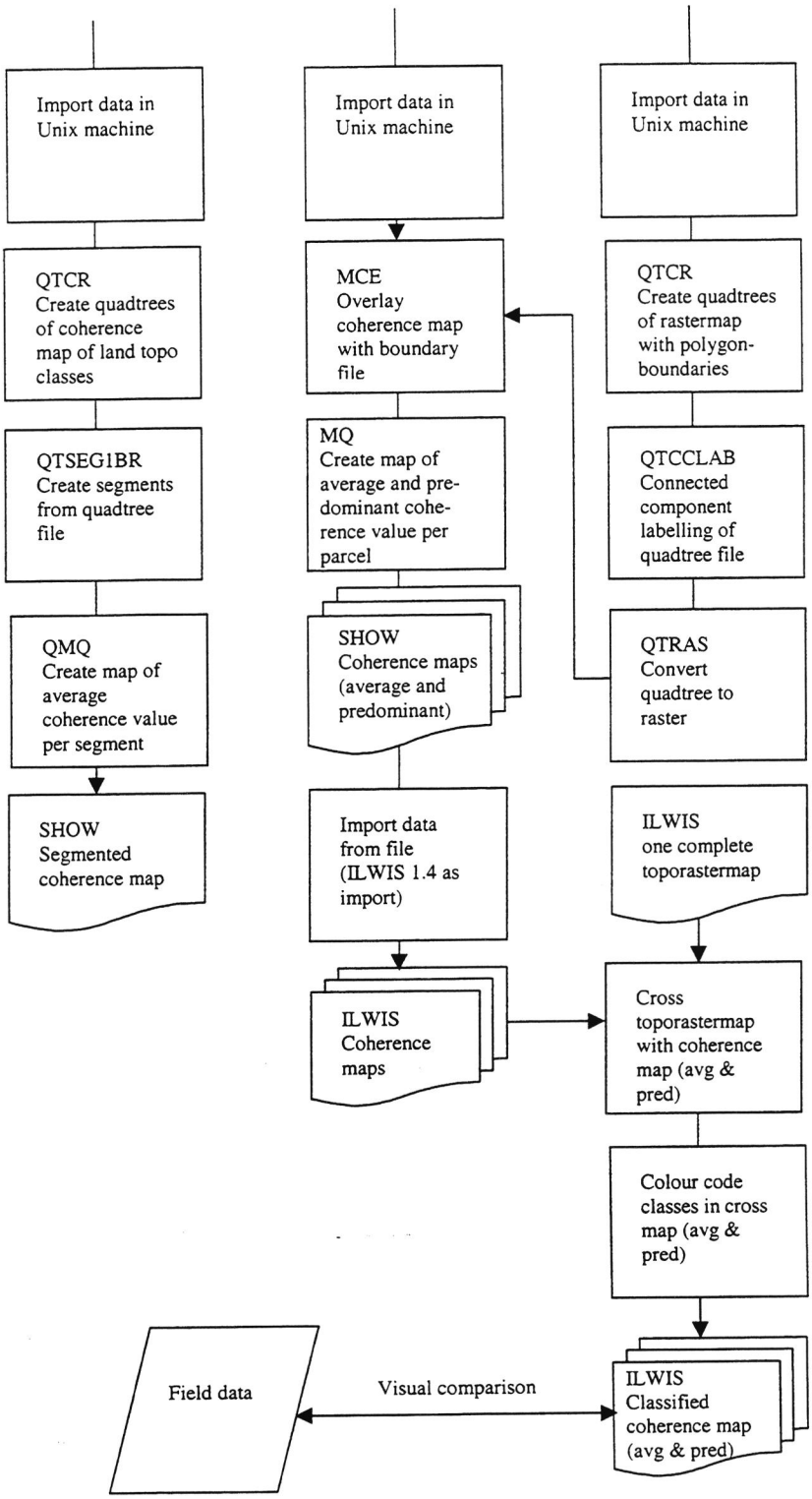
Import data in Unix machine
QTCR Create quadtrees of coherence map of land topo classes
QTSEG1BR Create segments from quadtree file
QMQ Create map of average coherence value per segment
SHOW Segmented coherence map
Import data in Unix machine
MCE Overlay coherence map with boundary file
MQ Create map of average and predominant coherence value per parcel
SHOW Coherence maps (average and predominant)
Import data from file (ILWIS 1.4 as import)
ILWIS Coherence maps
Import data in Unix machine
QTCR Create quadtrees of rastermap with polygon-boundaries
QTCCLAB Connected component labelling of quadtree file
QTRAS Convert quadtree to raster
ILWIS one complete toporastermap
Cross toporastermap with coherence map (avg & pred)
Colour code classes in cross map (avg & pred)
Field data
Visual comparison
ILWIS Classified coherence map (avg & pred)

B Coherence values per topo class

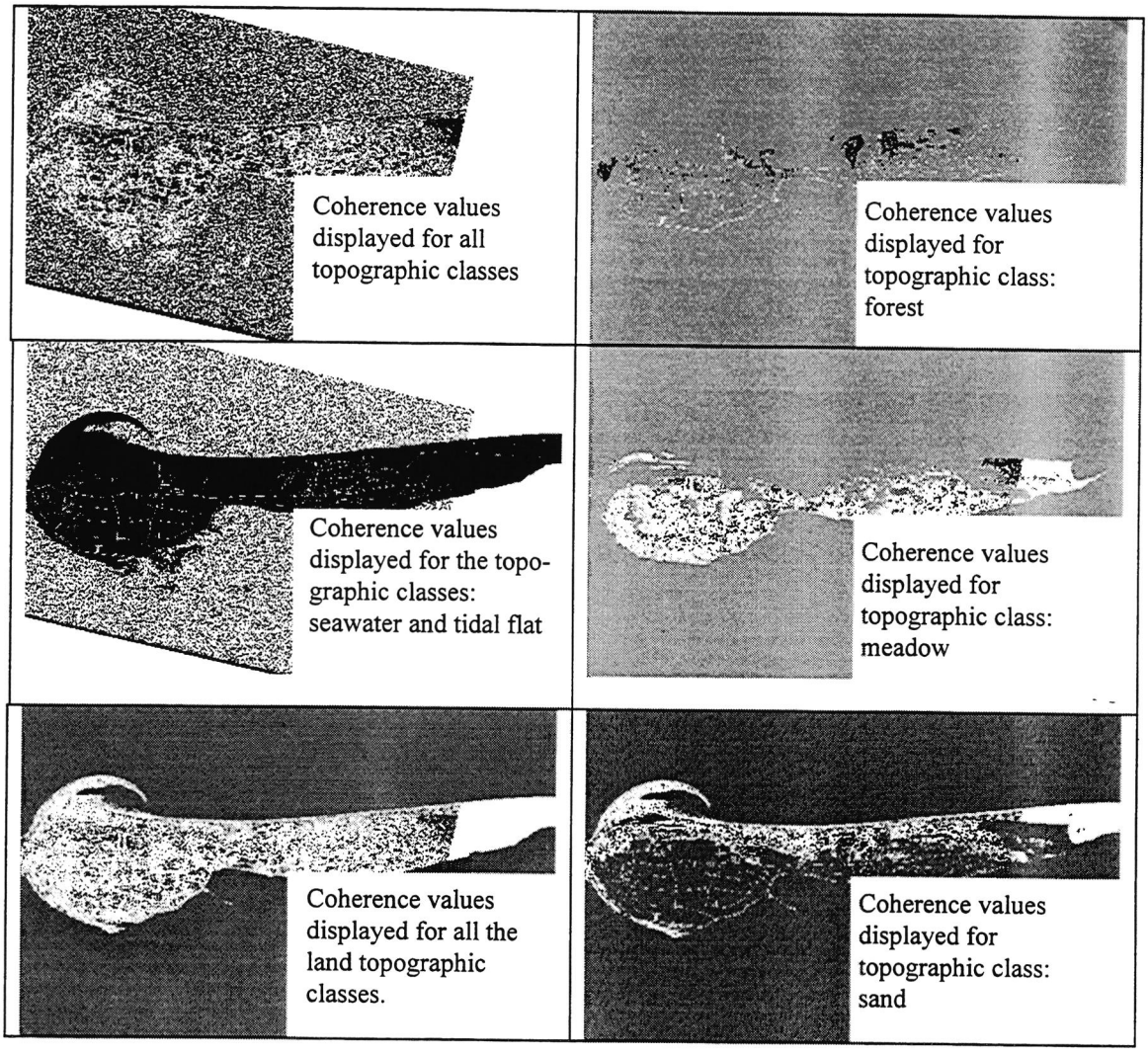

Coherence values displayed for all topographic classes

Coherence values displayed for topographic class: forest

Coherence values displayed for the topographic classes: seawater and tidal flat

Coherence values displayed for topographic class: meadow

Coherence values displayed for all the land topographic classes.

Coherence values displayed for topographic class: sand

C Histogram of coherence values

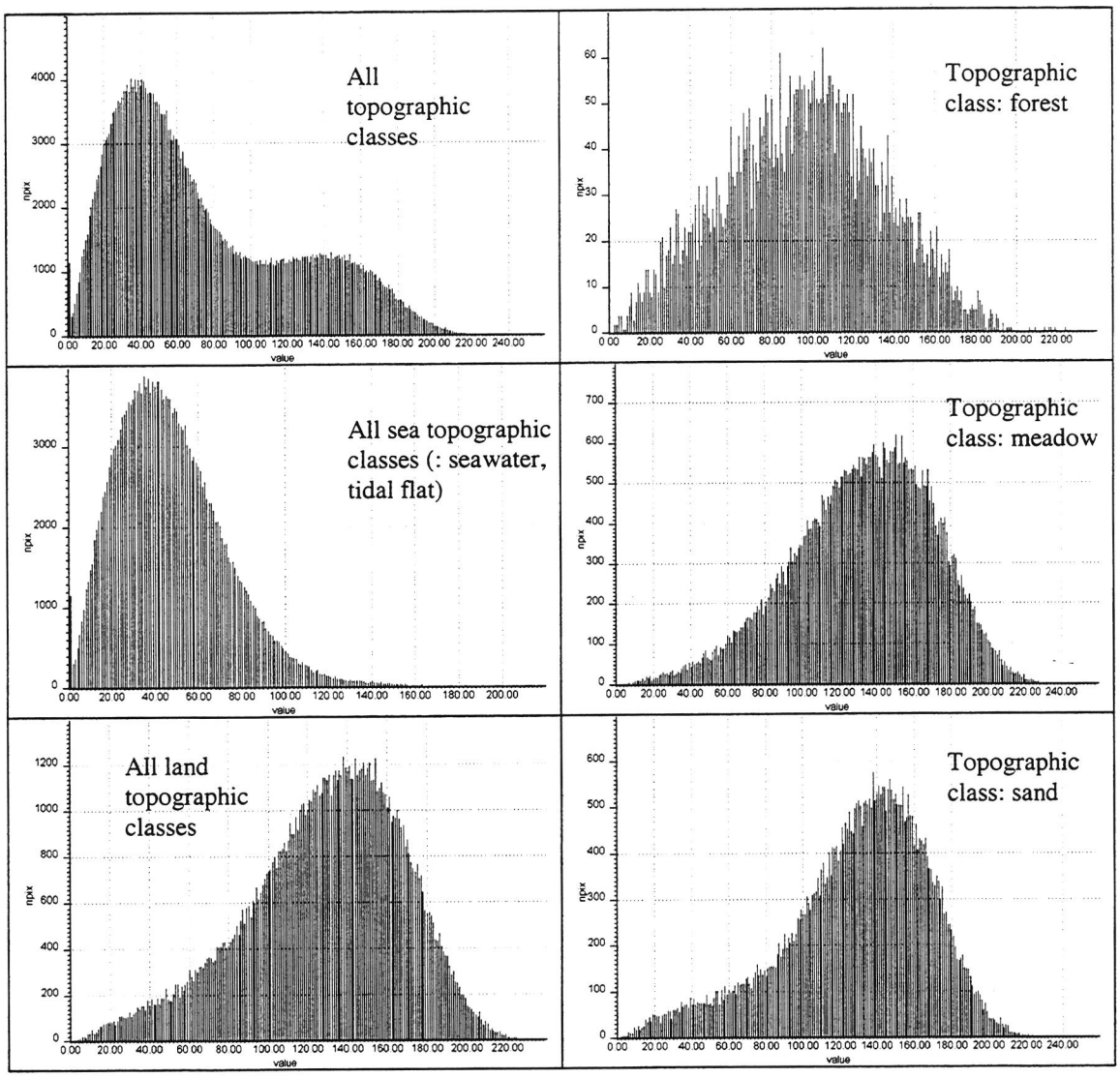

D Results of split and merge segmentation

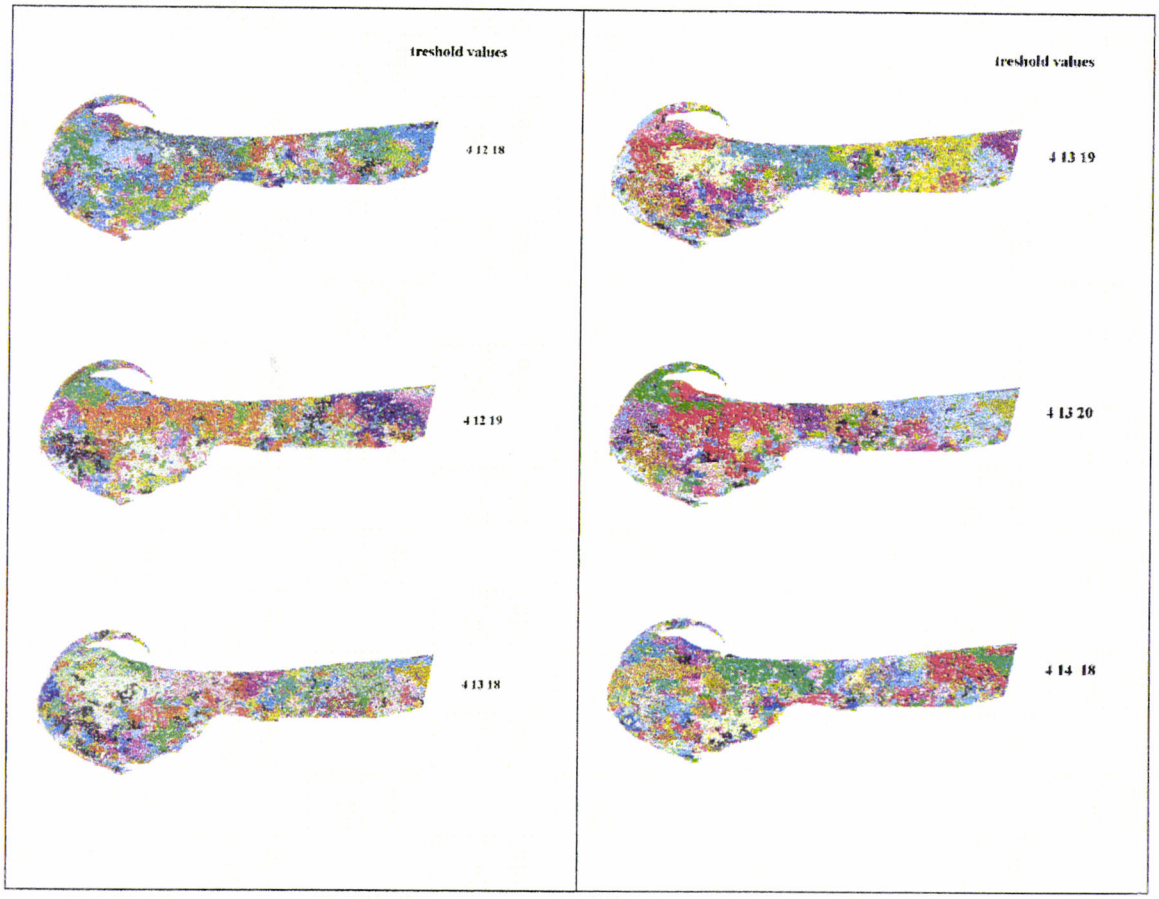

E Coherence values per parcel

Average coherence value for every polygon

Predominant coherence value for every polygon

F Classification of coherence values

Classified predominant coherence value (no zero's) per topographic class

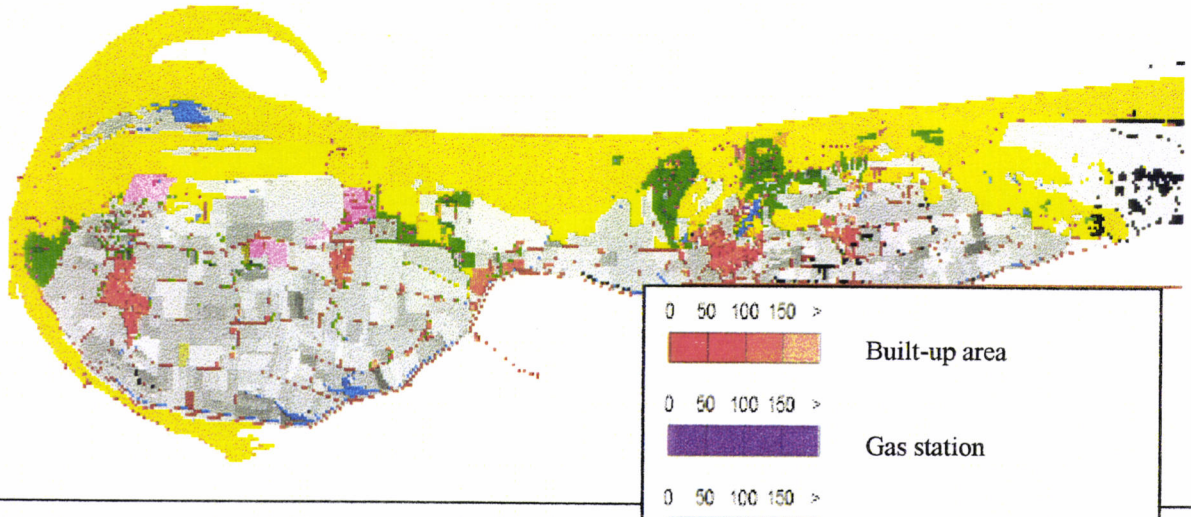

LEGEND:
(intensity corresponds to coherence values)

0 50 100 150 > Built-up area

0 50 100 150 > Gas station

0 50 100 150 > Landwater

0 50 100 150 > Forest

0 100 > Arable land

0 100 150 > Heath

0 100 150 > Sand and dunes

0 50 100 150 200 > Meadow

Undefined

No data

Classified average coherence value per Topographic class

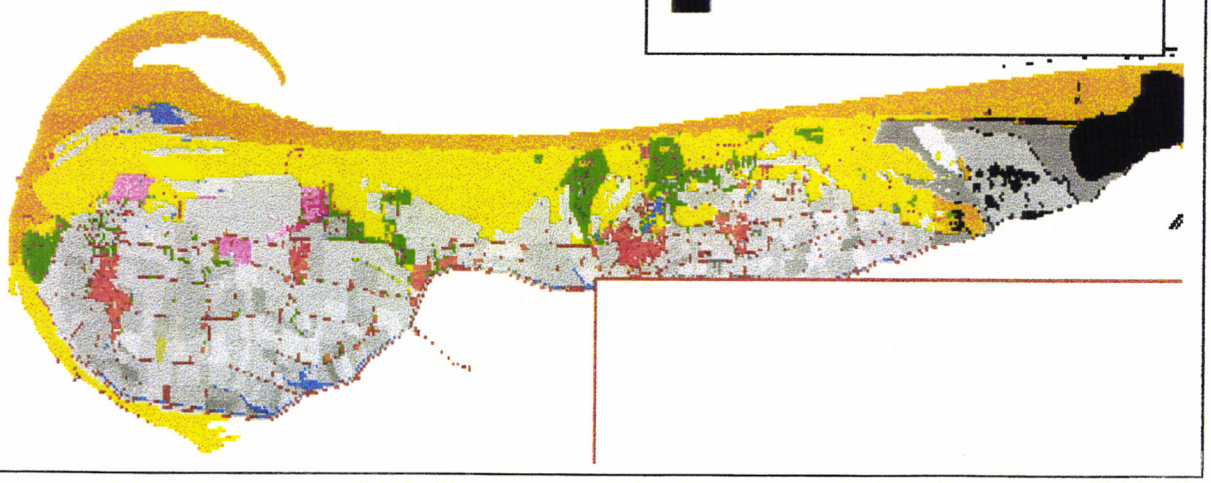

References

W. Alpers and I. Hennings, 1984,
A theory for the imaging mechanism of underwater bottom topography by real and synthetic aperture radar.
Journal of Geophysical Research, **89**(C6), 10,529-10,546.

G.P. De Loor and H.J. Brunsveld van Hulten, 1978,
Microwave measurements over the North Sea.
Boundary Layer Meteorology, **13**, 113-131.

R.M. Goldstein and H.A. Zebker, 1987,
Interferometric radar measurement of ocean surface currents.

B.G.H. Gorte, 1998,
Probabilistic segmentation of remotely sensed images.
PhD Thesis Wageningen Agricultural University and ITC. *ITC Publication No. 63.*

H. Greidanus, E.J. Huising, Y. Platschorre, R.J.P. Van Bree, D. Van Halsema, and E.M.J. Vaessen, 1999a,
Coastal DEMs with cross-track interferometry.
Proceedings IGARS '99, 28 June-2 July 1999, Hamburg, Germany.

H. Greidanus, R.J.P. Van Bree, E.J. Huising, J. Vogelzang, and E.M.J. Vaessen, 1999b,
Coastal currents with along-track interferometry.
Proceedings IGARS '99, 28 June-2 July 1999, Hamburg, Germany.

R. Horn, 1996,
The DLR airborne SAR project E-SAR.
Proceedings IGARSS '96 Symposium, 1624-1627.

E.J. Huising, R.W.L. Jordans, F.M. Spruijt, E.M.J. Vaessen, R.J. Wicherson, J.F. Zomerdijk, and M. van Persie, 1996,
Framework digital elevation model Dutch coast
Report BCRS-96-15, Netherlands Remote Sensing Board, Delft, Netherlands.

G.C. Huurneman, R. Gens, and L. Broekema, 1996,
Thematic information extraction in a neural network classification of multi-sensor data including microwave phase information.
Proceedings ISPRS 1996, Vienna, Vol II, p. 170.

G.C. Huurneman, 1998,
Operators used in the compilation of Coherence Maps for Thematic information extraction.
Proceedings ISPRS Commission VII Symposium, Budapest, pp. 538-543.

J.J. Leendertse, 1967,
Aspects of a computational model for long-period water propagation.
Memo RM-5294-PR, Rand Corporation, Santa Monica, California, U.S.A.

M. Marom, L. Shemer, and E.B. Thornton, 1991,
Energy density directional spectra of a nearshore wave field measured by interferometric SAR.
Journal of Geophysical Research, **96C**, 22125-22134.

J. Moreira, 1999,
Private communication.

M.P.G.Otten, and F.P.Ph. De Vries, 1995,
Moving target indication: Phase 2 of EUCLID RTP 9.1, WP 38140.
TNO report FEL-95-C245, 's Gravenhage, Netherlands.

C. Prati, F. Rocca , and A.M. Guarnieri, 1992,
SAR interferometry experiments with ERS-1.

R. Scheiber, 1998,
Single-pass interferometry with the E-SAR system of DLR.
Proceedingd Eusar '98, 47-50.

R. Touzi, A.Lopes, and P.W. Vachon, 1996,
Estimation of the coherence function for interferometric SAR applications.
In: *EUSAR'96*, Koenigswinter, Germany, 241-244.

P.T.A. Van den Hout, 1997,
The development and evaluation of a multiresolution, multigrid phase unwrapping algorithm for SAR interferometry.
TNO-report FEL-97-S009, TNO Physics and Electronics Laboratory, 's Gravenhage, Netherlands.

M.W.A. Van der Kooij, D. Van Halsema, and W. Groenewoud, 1993,
SAR land subsidence monitoring.
TNO report FEL-93-B084, TNO Physics and Electronics Laboratory, 's Gravenhage, Netherlands.

J. Vogelzang, 1998,
Radar imaging of sea bottom topography.
Thesis. University of Utrecht, Utrecht, Netherlands.

U. Wegmuller, and C.L. Werner, 1994,
Analysis of interferometric land surface signatures.
Proceedings of PIERS'94, Noordwijk, The Netherlands, Paper Code 039.

C. Wimmer, R. Siegmund, and J. Moreira, 1999,
Derivation and validation of high precision topography models in the Waddensea with airborne SAR-interferometry, 1999.
Proceedings IGARS '99, 28 June-2 July 1999, Hamburg, Germany.

H.A. Zebker, C.L. Werner, P.A. Rosen, and S. Hensley, 1994,
Accuracy of topographic maps derived from ERS-1 interferometric radar.
IEEE Transactions on Geoscience and Remote Sensing, **32**.